The Dissertation Committee for Dung Duc Phan
certifies that this is the approved version of the following dissertation:

A Search for Neutron-Antineutron Oscillation in the NOvA Experiment

Committee:

Karol Lang, Supervisor

Peter Onyisi

Jack Ritchie

Pawan Kumar

A Search for Neutron-Antineutron Oscillation in the NOvA Experiment

by

Dung Duc Phan

DISSERTATION

Presented to the Faculty of the Graduate School of

The University of Texas at Austin

in Partial Fulfillment

of the Requirements

for the Degree of

DOCTOR OF PHILOSOPHY

THE UNIVERSITY OF TEXAS AT AUSTIN

December 2020

Dedicated to William Phan-Vu.

Acknowledgments

Achieving this Ph.D. has been an exhausting run, and I would not have been reaching the finish line without the great support and guidance from my family, friends, and colleagues.

I would first like to extend my deepest gratitude to my advisor Karol Lang. Your unwavering guidance in academic and professional development is invaluable for the long scientific research journey ahead of me.

My sincere appreciation goes out to the home field research team. Adam Schreckenberger, Will Flanagan, and Junting Huang are three postdocs friends who took me under their wings to teach me their ways of doing and loving physics. Lessons learned are immense, yet more important is the friendship that grows out of this mentorship. A little more special thanks to Junting. He has always been a source of encouragement for my research endeavor in general and my pursuit of this neutron oscillation research in particular. To Simon de Rijck, Beatriz Tapia, Ramon Salazar, Thomas Carroll, and Brandon Soubasis, I am grateful to have you as friends. Your companionship has always been a source of warmth during my years in graduate school.

Besides the University of Texas, Fermilab can be considered my second home in the US. The hospitality that people there have shown me makes every one of my trips to the lab something to look forward to.

In the NOvA collaboration, I first want to thank people in the Exotics group, especially Matthew Strait, for many inspiring discussions regarding the development of this analysis. Big thanks to people in the DAQ working group who organize the excellent annual expert training where I learned a great deal about the DAQ system. Many thanks to Teresa Lackey, who, in countless times, saves me from DAQ issues. The deployment of the neutron oscillation trigger would have been ten times more challenging without the help from people in the DDT working group, especially Shih-Kai Lin. Working in the NOvA Test Beam has been an excellent experience as I had an opportunity to tinker with detector hardware and observe beam physics in action. I learned a lot from everyone in the Test Beam team, especially Mike Wallbank and Yagmur Torun. And all of this would not have happened without the kind support from Alex Sousa.

Special recognition goes to the Universities Research Association, Inc. Your generosity has alleviated my financial burden and allowed me to accomplish two important research projects at Fermilab, which eventually lead to the completion of this thesis.

I am indebted to Hien Vu, for unconditioned love and support, especially when my work life is going nowhere.

Lastly, no words are enough to thank my parents for the sacrifice they have made for me to receive a good education.

A Search for Neutron-Antineutron Oscillation in the NOvA Experiment

Dung Duc Phan, Ph.D.
The University of Texas at Austin, 2020

Supervisor: Karol Lang

This dissertation presents the search for neutron-antineutron oscillation using the data collected in the Far Detector of the NOvA experiment. Searching for neutron anti-neutron oscillation is becoming an active research direction that promises immense values for the field of particle physics and cosmology. Experimental observation of the phenomenon would offer the possibility of new physics associated with anomalous B and $B - L$ violating processes. This work is opening with a general introduction of the neutron-antineutron oscillation, its theoretical motivations, and recent empirical results related to the topic. The data-driven trigger that allows the NOvA experiment to collect the signal-like events constitutes a significant work of this study and will be described in detail. Following the discussion of the trigger, the thesis focuses on the development of a selection method to further classify collected events into the signal candidates and the background. This search chooses an analysis approach in which the real data

is partially unblinded to assist the development and evaluation of the event selection. Because this is an ongoing work and essential aspects of the analysis have not been all finalized, this thesis closes out with a sensitivity study. By analyzing the data from 4 months of Far Detector exposure, a 90% C.L. sensitivity limit of 4×10^{30} years is placed on the oscillation lifetime of bound neutrons inside the ^{12}C targets. This limit is equivalent to a sensitivity of 0.57×10^{8} s placed on the oscillation lifetime of free neutrons. The NOvA's sensitivity is a factor of 5 below the most stringent limit of 2.7×10^{8} s set by the Super-Kamiokande experiment.

Table of Contents

List of Tables

List of Figures

Chapter 1

Introduction

Throughout most of the existence of human civilization, the permanence of matter around us has usually been taken for granted. Only until the advent of modern physics, we have learned to appreciate that the basic building blocks of matter do not just disintegrate spontaneously as most elementary particles. From the perspective of particle physics, this stability owes its existence to the conservation of the baryon number $\mathcal{B}$. One can assign a definite value of $\mathcal{B}$ to each of the elementary particles: $1/3$ for quarks, $-1/3$ for anti-quarks, and 0 for leptons. The conservation of $\mathcal{B}$ asserts that the sum of baryon numbers from all particles involved in a process must not change between the initial and the final states. All physics processes observed so far respect this conservation law.

However, the seemingly apparent stability of matter is not enough empirical evidence to guarantee the absolute $\mathcal{B}$ conservation. Indeed, there are several reasons to question the validity of this law. First of all, the conservation of $\mathcal{B}$ is "empirical". Unlike the conservation laws of momentum, energy, and electric charge conservation, it does not tie to any known symmetry, neither global nor local. There is no direct experimental evidence for an associated gauge field enforcing the conservation of $\mathcal{B}$.

Furthermore, the asymmetry between matter and anti-matter observed today necessitates the presence of $\mathcal{B}$ violation processes during very early moments of the Universe after the Big Bang. With those motivations, searching for $\mathcal{B}$ violation processes has always been the focus of the high energy physics. It will undoubtedly remain a primary goal of new experiments in the coming years. The outcomes of those experiments will navigate us through the uncharted water of a new physics.

Historically, the hunt for $\mathcal{B}$-violation processes started with the search of nucleon decays, in particular proton decays. The latest results [18–23] from the Super-Kamiokande water Cherenkov experiment have shown that the lifetime of protons lies beyond 10^{34} years. This limit puts a stringent constraint on baryogenesis models in which the $\mathcal{B}$-violation is manifested only via proton decays (or more generally via $\Delta\mathcal{B} = 1$ processes). Such a mechanism alone is not enough to generate the observed baryon-antibaryon asymmetry [5].

The $\mathcal{B}$-violation search thus shifted its focus toward processes that violates the baryon number conservation by two units, $\Delta\mathcal{B} = 2$ [24–27]. This thesis investigates one of such processes: the neutron-antineutron oscillation. Two types of searches have been pursued so far, with one focusing on transitions occurring with free neutrons, and the other is looking for bound neutron transitions. The former approach has been realized in several experiments (ILL in 1985 [28], Pavia University's Triga Mark II reactor in 1990 [29]) with the most recent result on the oscillation time of free neutron reported by the ILL Grenoble experiment in 1994, $\tau = 0.86 \times 10^8\,\mathrm{s}$ [30].

The search presented here follows the latter approach, whose basic working principle is to continually watch for the appearance of antineutrons that underwent spontaneous transition inside the atomic nuclei that comprise the detector. The sensitivity of the search scales with some specifications of an experiment, such as the energy resolution, the capability of track and shower reconstruction, as well as the total exposure. The type of material that comprises the detector is also an important factor as nuclear composition and structure strongly affect the oscillation probability of bound neutrons [31]. The Super-Kamiokande experiment has drawn the most stringent limit on the oscillation lifetime of intranuclear neutron-antineutron transition, $T = 1.9 \times 10^{32}$ years [2]. Applying a model describing the intranuclear suppression effect on the oscillation of bound neutrons [31], the Super-Kamiokande limit translates to a free neutron oscillation time of $\tau = 2.7 \times 10^8$ s.

This work explores the prospect of using the NOvA Far Detector to search for the oscillation of neutrons. The development of a trigger system dedicated to capturing the signal candidates will be discussed in detail. Lastly, the data from 4 months of exposure of the NOvA Far Detector, collected during the period from 9/2018 to 1/2019, will be analyzed to set the sensitivity for the search.

Chapter 2

The Physics of Neutron Oscillation

2.1 History of the Search for Baryon Instability

The idea of the stability of protons dates back to Hermann Weyl in 1929 [32]. Taking into account that positrons, muons, and mesons were undiscovered back then, a proton decay, as a modern physicist might picture, could not have been imagined. Weyl, on the other hand, wondered why protons and the electrons in an atom do not annihilate with each other. His solution to the problem was the existence of two kinds of electric charges, which are carried by protons and electrons separately. If such charges conserve independently, the annihilation is prohibited, leading to the stability of matter.

Although being largely ignored for almost a decade, the problem of proton stability was reexamined when Ernst C. G. Stueckelberg in 1938 [33] and Eugene P. Wigner in 1949 [34] independently proposed a new conserved quantity named "baryon number". In the 40s and 50s, "baryon" is the collective name for the members of the nucleon family. Originated from the Greek word for "heavy" ($\beta\alpha\rho\nu\zeta$, barýs), the name is introduced to the field by Abraham Pais [35, 36] for the reason that most known elementary particles back then had much lower masses than the baryons. All baryons, and under the CPT invariance, all anti-baryons, are assigned a baryon number of +1 and −1, respectively. Lighter particles, including photons, electrons, positrons, muons, and mesons, assume a baryon number of 0. The law of baryon number conservation is a simple assertion that the total baryon number must conserve in any process. The decay of a proton into lighter particles would alter the baryon number, thus violating the conservation, so it must be forbidden. As a result, this established a general belief in the existence of absolute conservation of baryon number.

The apparent stability of matter is, however, the only empirical proof for the law of baryon number conservation during that time. Since the beginning of the 50s, various ideas of experimental tests for the conservation law started to emerge. Maurice Goldhaber proposed the first one in the summer of 1954 during a visit to Los Alamos Scientific Laboratory (LANL's name at the time). Inspired by the Bondi-Gold-Hoyle theory of continuous matter creation[1], Goldhaber pushed the idea to a new level: if matter can be spontaneously created, it can also be spontaneously destroyed. In this spirit, a bound nucleon can disappear and leave the nucleus with an excited state and induce spontaneous fission [39]. This reaction had already been observed with a few isotopes, including ^{232}Th. From the measured half-life of ^{232}Th of about 1.4×10^{10} years and the spontaneous fission probability of 1.1×10^{-11}, Goldhaber was able to put a lower limit on the nucleon disappearance

[1] Tommy Gold contemplated that as the universe expands, new matter can be created in the widening interstellar gaps. Tommy Gold and Hermann Bondi published the theory [37] in 1949, followed by a mathematical description [38] by Fred Hoyle later the same year.

lifetime $\tau > 1.4 \times 10^{18}$ years [39].

About the same time, F. Reines and C. Cowan were setting up a large liquid scintillator counter [3] at Los Alamos to search for atmospheric neutrinos. Goldhaber collaborated with the two neutrino physicists and utilized their detector to look "parasitically" for proton decays. The setup consists of a 300-liter liquid scintillator detector surrounded by paraffin walls of 2 ft in thickness. It is partially shielded from cosmic rays in an underground room with 100 ft of rock overburden. The final products of a proton decay are expected to have a kinetic energy of about 100 MeV. The pulse height distribution observed is shown in Fig. 2.1. The integrated

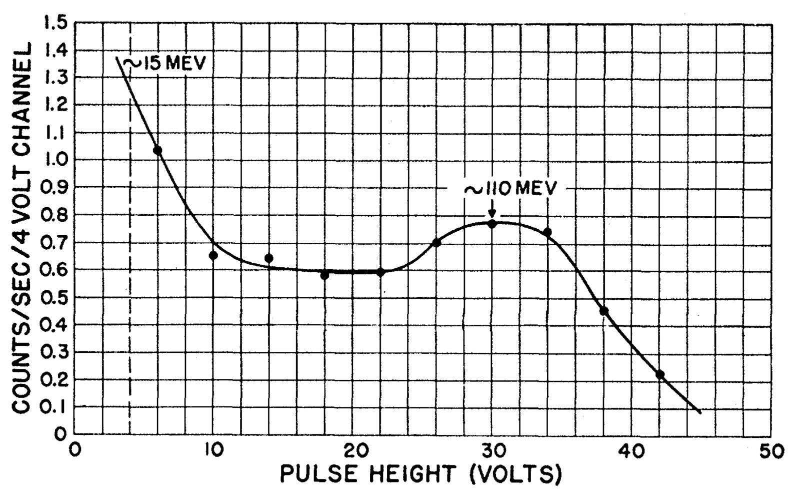

Figure 2.1: Pulse height spectrum for an exposure of 1000 s per point. The integrated area for pulses larger than the cut-off bias of about 15 MeV, is 6.6 counts/s [3].

counting rate in the "signal" region is 6.6 Hz. This rate translates to a lower limit of the mean proton lifetime of 1.5×10^{20} years [3]. However, since the event rate and the spectral shape are both consistent with cosmic muons[2], Goldhaber concluded that the decay of protons could attribute to, at most, only a fifth of the observed counts. Also, the number of bound nucleons in the detector is an order of magnitude larger than that of protons. As a result, this first direct search has placed a lower limit of $\tau > 10^{21}$ years on the lifetime of free protons and of $\tau > 10^{22}$ years on the lifetime of bound nucleons [3].

From a theoretical point of view, the suspicion that nucleons might be unstable, or more generally, that the law of baryon number conservation is not absolute, originated from two concerns. First of all, the law of $\mathcal{B}$ conservation is merely an ad-hoc solution for the apparent stability of the baryonic matter. The Noether's theorem and gauge field theories have established a connection between conservative charges and the symmetries that the physical system must obey. Searching for such connection in the case of baryon number conservation was conducted as early as 1955 by Lee T. D. and Yang C. N. [40]. In this article, Lee and Yang considered the baryon number conservation[3] as a result of a local symmetry. They also placed an upper limit on the strength of the long-range interaction associated with this symmetry by analyzing the null result of Eotvos' 1922 experiment [41]: at most, the new force is 10^{-5} times weaker than

[2]Interestingly, at the time of the paper, muons were misclassified as mesons, so the authors mentioned them as "muon mesons."

[3]Lee and Yang used the phrase "conservation of heavy particles."

gravity [40]. Following Lee and Yang's approach, various models have vetted the different ways (vector bosons, scalar bosons, spin-dependent interactions, etc.) the baryon symmetry can result in a macroscopic force. In these models, the new long-range force can leave its signature via either deviation from the $1/r^2$ law or violations of the universality of free fall [42]. However, results from the Eot-Wash experiments - the modern versions of the Eotvos' experiment - have placed strong constraints on both possibilities [43–48].

The second concern when questioning the $\mathcal{B}$ conservation comes from the work on the baryon asymmetry of the Universe (BAU) by Sakharov in 1967 in which he emphasized the need for $\mathcal{B}$-violation processes. Matter and anti-matter were in a thermal equilibrium via pair-creation and annihilation reactions in the very early moments of the Universe. However, when it started to cool down, the energies became too small to sustain the pair creation. Particles and antiparticles annihilate to photons as end products. However, for some reason, a minute amount of matter survived the cooling and formed the Universe as we see today. The ratio between the numbers of baryons and photons observed in the Universe today, $\eta = n_{\mathcal{B}}/n_{\gamma}$, quantifies the level of matter-antimatter asymmetry. From Big Bang Nucleosynthesis and measurements of the power spectrum of fluctuations in the cosmic microwave background, η is determined to be $(6.19 \pm 0.14) \times 10^{-10}$ [49]. Sakharov suggested that matter-antimatter asymmetry may have been created dynamically by baryogenesis from an initially symmetric state [50].

According to Sakharov [50], three conditions are needed for successful baryogenesis : (i) baryon number violation, (ii) C and CP violation, and (iii) a deviation from thermal equilibrium. First, the violation of baryon number conservation is a must for any system to evolve from a $\mathcal{B} = 0$ state to a $\mathcal{B} \neq 0$ state. The second condition is required to break the balance between processes that generate matter-antimatter asymmetry and their C or CP conjugations that would cancel out the effect. Lastly, thermal equilibrium is a state in which all observables' expectation values are constant; therefore, a deviation from thermal equilibrium is a must to allow the evolution from $\mathcal{B} = 0$ to $\mathcal{B} \neq 0$. The first Sakharov condition presents a strong motivation to search for $\mathcal{B}$ violation processes.

2.2 Modern Perspective on the Conservation of $\mathcal{B}$

2.2.1 Baryon Number Violation in the SM and GUTs

The 70s witnessed the theoretical completion of the Standard Model (SM) of particle physics and the emergence of first grand unification theories (GUTs). One of the primary goals is to construct models that incorporate viable $\mathcal{B}$-violation mechanisms that can generate successful baryogenesis. It is interesting to notice that[4] $\mathcal{B}$-violation processes are possible even in the Standard Model: the $U(1)_{\mathcal{B}}$ is a global symmetry at the classical level, but breaks at the quantum level by Adler-Bell-Jackiw anomalies [51–53]. As a

[4]In fact, all three Sakharov's conditions are fulfilled by the SM: the baryon number is violated by sphaleron processes described above, P and CP are violated by the electroweak interaction and the quark Yukawa couplings, and the non-equilibrium condition present in the inflation.

result, non-perturbative electroweak processes can transform baryons into leptons and vice-versa in a way that leaves only the $\mathcal{B} - \mathcal{L}$ difference unchanged. The low temperature of the present Universe strongly suppresses the rate of such transitions. Nevertheless, it should have been more significant during the era of the electroweak phase transition, which occurred when $T \sim 170$ GeV [53, 54]. However, detailed calculations indicated that this $\mathcal{B}$-violation mechanism alone predicts a baryon-to-photon ratio of η at many orders of magnitude smaller than the observed value of $\sim 10^{-10}$ [55], making baryogenesis within the SM very challenging.

Substantial matter-antimatter asymmetry to fit the observed data necessitates BSM physics models that incorporate new $\mathcal{B}$-violation mechanisms. Thus, most of the newly emerging GUT models embrace the baryon number violation as a key ingredient. The difference among these models is the selection rules that the $\mathcal{B}$-violating processes respect. When a nucleon spontaneously disintegrates, the angular momentum conservation requires that the spin 1/2 of the nucleon must transfer to either a lepton or another nucleon. This leads to the following selection rules:

$$|\Delta(\mathcal{B} - \mathcal{L})| = 0 \text{ or } 2; \tag{2.1}$$

in which, $\mathcal{L}$ is the lepton number, with a role similar to that of the baryon number $\mathcal{B}$. Leptons (anti-leptons) are assigned $\mathcal{L} = 1$ ($\mathcal{L} = -1$) while non-lepton particles all have $\mathcal{L} = 0$. All processes in the Standard Model respect $\Delta(\mathcal{B} - \mathcal{L}) = 0$, even at the non-perturbative level. The rule

$\Delta(\mathcal{B}-\mathcal{L}) = 2$ enables three transitions: (i) $\Delta\mathcal{B} = -\Delta\mathcal{L}$, (ii) $|\Delta\mathcal{B}| = 2$ and (iii) $|\Delta\mathcal{L}| = 2$. A prominent prediction of early GUT models - the decay of protons - is an example of $|\Delta\mathcal{B}| = |\Delta\mathcal{L}| = 1$ transitions. Unfortunately, constraints on the life-time of protons from past searches, see Figure 2.2 , rendered the baryogenesis from $\Delta\mathcal{B} = 1$ processes alone unviable [5]. Therefore, transitions that respect $\Delta\mathcal{B} = 2$ need to be examined in more detail to see if they are relevant to the baryon asymmetry problem. Searching for the neutron-antineutron oscillation is a feasible approach.

Another reason that makes the neutron-antineutron oscillation an interesting case study is the energy scale to which it probes. To make a comparison, let us discuss the proton decay first. In the most simple case without supersymmetry, a typical decay is carried out with an operator of the form $gqqql/\Lambda^2$, in which g is the dimensionless coupling constant and Λ is the effective UV-cutoff or equivalently the energy scale probed. The rate of this decay is $\Gamma \propto (m_p^\alpha/\Lambda^2)^2$ and needs to have the dimension of energy or m_p, so we find $\alpha = 5/2$. With the current lower limit of proton's life-time around 10^{34} years, the corresponding energy probed is at the GUT scale[5]

$$\Lambda \propto \sqrt[4]{\frac{m_p^5}{\Gamma}} \approx \sqrt[4]{\frac{1 \text{ GeV}^5}{(10^{34} \cdot 31.5 \times 10^6 \cdot 1.52 \times 10^{24})^{-1} \text{ GeV}}} = 2.6 \times 10^{16} \text{ GeV}.$$

On the other hand, a neutron-antineutron transition features an operator of

[5]Using the conversion 1 GeV $\approx 1.52 \times 10^{24}$ s^{-1} and 1 year $\approx 31.5 \times 10^6$ s. A complete table showing how different conventional units are related in the natural system of units can be found at http://www.saha.ac.in/theory/palashbaran.pal/conv.html. The masses of protons and neutrons are approximated to 1 GeV for simplicity.

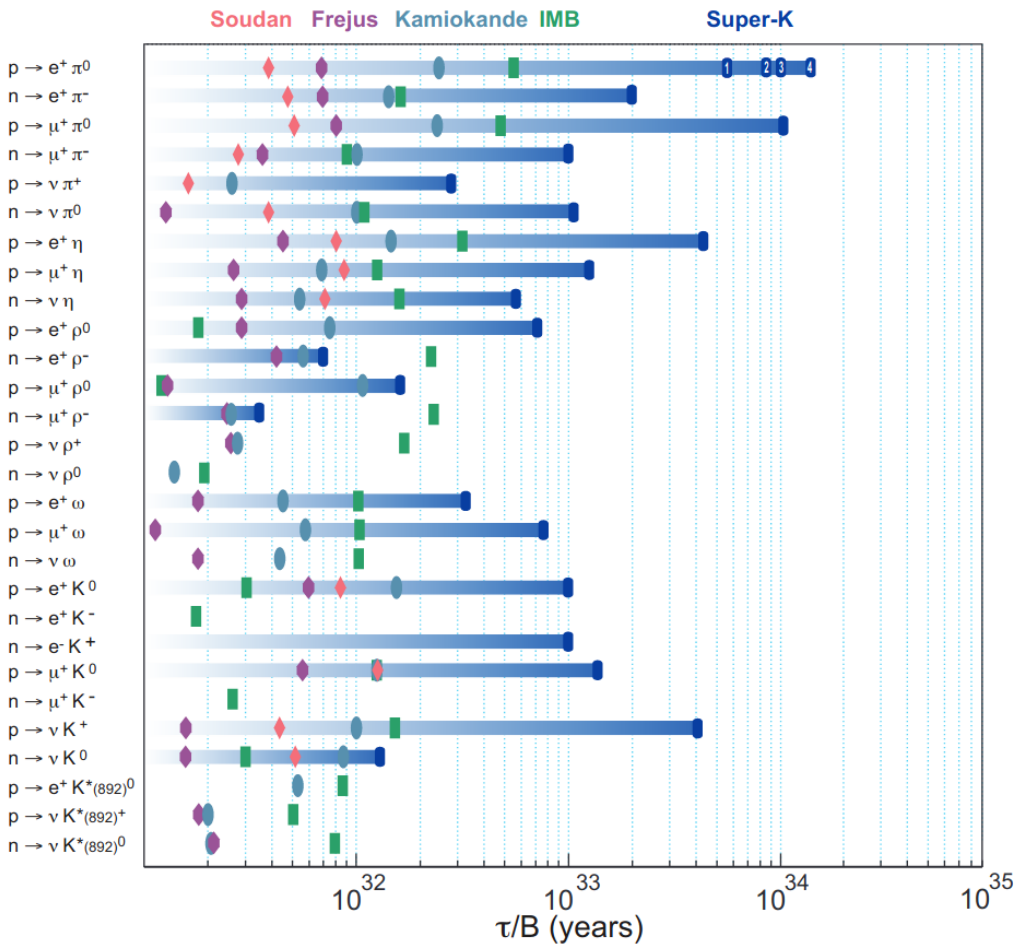

Figure 2.2: Summary of experimental proton decay searches [4] by Super-K (dark blue gradient band with marker) and previous experiments, Soudan (pink diamonds), Frejus (purple hexagons), Kamiokande (light blue ovals), and IMB (light green rectangles).

the form $gqqq\bar{q}\bar{q}\bar{q}/\Lambda^5$. Using similar dimensional analysis, the transition rate is $\Gamma \propto m_n^{11}/\Lambda^{10}$. The current limits on the oscillation time of free neutrons around 10^8 s implies a UV-cutoff

$$\Lambda \propto \sqrt[10]{\frac{m_n^{11}}{\Gamma}} \approx \sqrt[10]{\frac{1\ \text{GeV}^{11}}{(10^8 \cdot 1.52 \times 10^{24})^{-1}\ \text{GeV}}} = 1.6 \times 10^3\ \text{GeV},$$

which is of TeV scale. From this crude dimensional analysis, it is clear that the search for neutron-antineutron oscillation provides us a probe to new physics in the electroweak TeV scale, a much more accessible range compared to the GUT scale at $10^{15} - 10^{16}$ GeV.

If we allow the possibility that $\mathcal{B}$ might not be an exact symmetry of Nature, several puzzles need to be solved to explore the new physics underlying the $\mathcal{B}$-violation:

1. Is there a symmetry that enforces that $\mathcal{B}$ conservation? Furthermore, if it exists, is it a global or local one?

2. Does $\mathcal{B}$ stand as a symmetry on its own or in combination with $\mathcal{L}$ i.e., $\mathcal{B} - \mathcal{L}$ symmetry exists?

3. What is the energy scale that characterizes the violation of $\mathcal{B}$?

4. What is the mechanism of baryogenesis?

Despite almost four decades of concerted search, we observed no sign of proton decays. In this scenario, the search for neutron-antineutron oscillation stands out as a feasible approach to the physics of $\mathcal{B}$ violation in the years to come.

2.3 Phenomenology of Neutron Oscillation

In this section, we will discuss the features of neutron-antineutron oscillation in two cases: the free neutrons and bound neutrons in nuclei. To avoid unnecessary confusion, we mention here the notations that will appear in the following sections. Without further notices, τ denotes the free neutron oscillation time, while T indicates the intranuclear transition time. Notations $n\bar{n}$ and $p\bar{n}$ indicate the annihilations of an antineutron with a nearby neutron and proton. On the other hand, $n - \bar{n}$ is merely an abbreviation of the phrase "neutron-antineutron oscillation".

For our purpose, it is sufficient to consider the 2×2 Hamiltonian that dictates the oscillation of a neutron-antineutron mixed state:

$$H_{n\bar{n}} = \delta m \int \mathrm{d}^3x \; \bar{\psi}_n \sigma_1 \psi_n, \tag{2.2}$$

where $\psi = \begin{pmatrix} n \\ \bar{n} \end{pmatrix}$ and σ_1 is the Pauli matrix $\begin{pmatrix} 0 & 1 \\ 1 & 0 \end{pmatrix}$. The factor δm is the transition mass which represents the underlying physics that breaks the baryon number conservation. The lifetime of oscillation occurring in free space is the inverse of this transition mass $\tau_{n\bar{n}} = 1/\delta m$. The Schrodinger's equation governs the time evolution of the mixed state:

$$\mathrm{i}\frac{\partial}{\partial t}\begin{pmatrix} n \\ \bar{n} \end{pmatrix} = \begin{pmatrix} E_n & \delta m \\ \delta m & E_{\bar{n}} \end{pmatrix}\begin{pmatrix} n \\ \bar{n} \end{pmatrix} = A\begin{pmatrix} n \\ \bar{n} \end{pmatrix}. \tag{2.3}$$

The difference in the energy between neutron E_n and antineutron $E_{\bar{n}}$ will be manifested in different ways depending on the potential that the particles experience, e.g., intranuclear field or external magnetic field. The formal solution for the equation (2.3) can be written as:

$$\begin{pmatrix} n \\ \bar{n} \end{pmatrix}_t = \mathrm{e}^{-\mathrm{i}At} \begin{pmatrix} n \\ \bar{n} \end{pmatrix}_{t=0} . \tag{2.4}$$

Consider a particle state starting as a neutron, i.e. $\begin{pmatrix} n \\ \bar{n} \end{pmatrix} = \begin{pmatrix} 1 \\ 0 \end{pmatrix}$, the probability of this state being detected as an antineutron, i.e. $\begin{pmatrix} n \\ \bar{n} \end{pmatrix} = \begin{pmatrix} 0 \\ 1 \end{pmatrix}$, is

$$P_{\bar{n}}(t) = \left| \begin{pmatrix} 0 & 1 \end{pmatrix} e^{-iAt} \begin{pmatrix} 1 \\ 0 \end{pmatrix} \right|^2 = \frac{4\delta m^2}{\Delta E^2 + 4\delta m^2} \sin^2 \left(\frac{\sqrt{\Delta E^2 + 4\delta m^2}}{2} t \right), \tag{2.5}$$

where $\Delta E = E_n - E_{\bar{n}}$. Neutron decay would not alter this formula as long as the time t is small enough compared to the neutron lifetime. The details on the calculation of $\mathrm{e}^{\mathrm{i}At}$ and the derivation of $P_{\bar{n}}(t)$ can be found in Appendix B.

As we mentioned before, two important cases relevant to experimental purposes will be considered here, namely oscillation of (i) free neutrons and (ii) bound neutrons. With the oscillation of free neutrons $t\sqrt{\Delta E^2 + \delta m^2} \ll 1$, the transition probability becomes[6]

$$P_{\bar{n}}(t) \sim \frac{4\delta m^2}{\Delta E^2 + 4\delta m^2} \left(\frac{\sqrt{\Delta E^2 + 4\delta m^2}}{2} t \right)^2 = (\delta m \cdot t)^2 \equiv \left(\frac{t}{\tau_{n\bar{n}}} \right)^2, \tag{2.6}$$

where, once again, we see the appearance of the free oscillation lifetime $\tau_{n\bar{n}} = 1/\delta m$. All the dynamics of $n\bar{n}$ transition is determined by the transition mass

[6] Some authors also call this condition $t\sqrt{\Delta E^2 + \delta m^2} \ll 1$ the "quasi-free" condition.

δm. For the experiments searching for $n\bar{n}$ transition that uses free neutrons, the sensitivity is proportional to the number of neutrons reaching the detector N_n and their average time of flight $\sqrt{\langle t^2 \rangle}$. The use of an intensive source of cold or ultracold neutrons can help to maximize the sensitivity of this type of experiment.

For the case of bound neutrons, due to the potential difference $\Delta E \sim$ 100 MeV experienced by the neutron and antineutron states, the transition probability is strongly suppressed [56]. A qualitative argument can be made to quantify the strength of the nuclear suppression factor. Even though a bound neutron is in constant interactions with other nucleons in a nucleus, we can consider it to be effectively free for very short amounts of time.

$$\delta t \sim \frac{1}{E_{\text{binding}}} \sim \frac{1}{10\text{ MeV}} \sim 10^{-22}\text{ s.} \tag{2.7}$$

This means, in every second, the neutron will experience this free condition for $N \sim 1/\delta t \sim 10^{22}$ times. The transition probability per second is then modified as:

$$P_{\bar{n}}(t) \equiv \frac{1}{T_{n\bar{n}}} = \left(\frac{\delta t}{\tau_{n\bar{n}}}\right)^2 \frac{1}{\delta t}, \tag{2.8}$$

in which, $T_{n\bar{n}}$ is the oscillation time of bound neutrons. We can see that

$$T_{n\bar{n}} = \tau_{n\bar{n}}^2 \times R, \tag{2.9}$$

with $R = 1/\delta t \sim 10^{22}\text{ s}^{-1}$ is called the nuclear suppression factor.

2.4 Current Status

As mentioned earlier, there are two methods for observing $n - \bar{n}$ transitions: one searches for the oscillations of free neutrons and the other searches for those of bound neutrons in nuclei. This thesis follows the latter approach. However, this section will cover the status of the search for neutron antineutron oscillations in both scenarios, giving more or less a complete picture of the field as a whole.

2.4.1 Free Neutron Searches for Neutron Antineutron Oscillations

In this approach, one first produces a slow neutron[7] beam propagating freely to a distant thin material target. During the flight, neutron oscillations might occur and lead to the appearance of antineutrons. These antineutrons will be detected via their annihilations at the target. The annihilations generate patterns with a rather well-defined energy deposition of approximately 2 GeV, usually formed by 4 to 5 pions in the final state. This distinctive signature can be efficiently identified with a tracker and a calorimeter surrounding the target. The combination of this unique signature and timing of the beam actively suppresses potential backgrounds.

As pointed out in Section 2.3, the "quasi-free" condition $t\sqrt{\Delta E^2 + \delta m^2} \ll 1$ must hold for transitions of this type to happens. This condition introduces some experimental requirements: (i) a low pressure

[7]Neutrons with kinetic energy below 10 eV.

($< 10^{-5}$ Pa) to extend the free path length of neutrons and (ii) a low ambient magnetic field (1 to 10 nT) along the neutrons' flight path which can induce a large energy difference and damp the oscillations. Even though advanced technologies of the vacuum system and magnetic shielding are desired, the free neutron oscillation experiments offer superior background suppression and increasing sensitivity.

The best limit on the free neutron oscillation time is currently set by the ILL Grenoble experiment in 1994; see Figure 2.3. This experiment utilized a cold neutron beam extracted from their high-flux research reactor. The beam intensity of 1.25×10^{11} n$\cdot$s^{-1} was propagated through a region with a pressure $P \sim 2 \times 10^{-4}$ Pa and an external magnetic field maintained at $|\vec{B}| < 10$ nT. Traces of antineutrons was sought with a 130 μm-thick carbon film target. Candidates events need to generate at least two tracks with one due to a charged particle in the tracker. Also, they are required to deposit total energy above 850 MeV in the enclosing calorimeter. The ILL Grenoble experiment detected no antineutron candidates during a total running time of 2.4×10^7 s. A 90% C.L lower limit of $\tau > 0.86 \times 10^8$ s for free neutron transitions was then established [30].

In the last two decades, several experiments are pursuing a sensitivity one to two orders of magnitude better than that of the ILL. This goal is very much plausible as we have witnessed notable advances in neutron moderation and transport technology, as well as the advent of bright neutron sources from proton spallation. One such effort is the neutron oscillation search at the

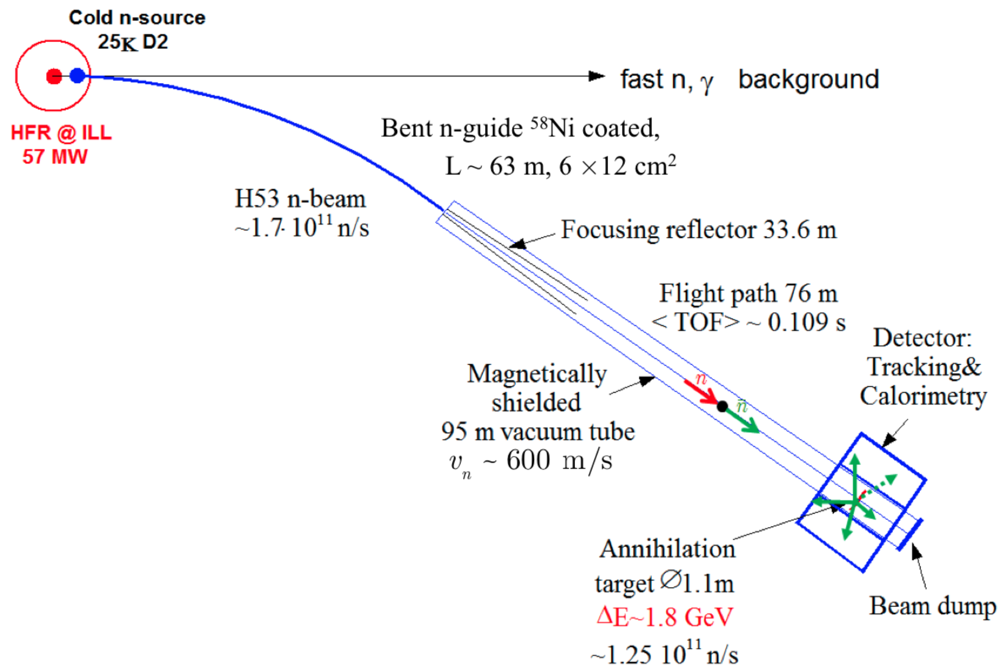

Figure 2.3: Setup of the ILL/Grenoble experiment [5].

European Spallation Source (ESS) [57] - a new reactor facility currently under construction in Lund, Sweden. The $n\bar{n}$ experiment in ESS expects to raise the sensitivity to the neutron oscillation lifetime to 2 orders of magnitude compared to the previous limit set by ILL Grenoble.

2.4.2 Searches for Oscillations of Bound Neutrons

In contrast to the approach discussed in the previous section, the working principle of this detection method is to monitor a large body of material continuously and look for isolated patterns with multiple prongs coming from a common vertex and an energy deposition between 1 to 2

GeV. These signatures result from an antineutron, which emerges from a bound neutron's spontaneous transition, annihilating with surrounding nucleons in the nuclear. Two main techniques of detection exploited so far are tracking calorimeter (Soudan [58], Frejus [59]), and water Cherenkov imaging (Kamiokande [60], Super-K [2], SNO [61]).

The limits on bound neutron oscillations time came from the experiments that were initially designed for proton decay search. Using an appropriate nuclear potential model, one can always convert an oscillation time limit on bound neutrons to its counterpart for free neutrons via Equation (2.9). Table 2.1 summarizes the lower limits of neutron's oscillation lifetime placed by various experiments.

Experiment	Source of neutrons	T (yr)	τ (s)
ILL [30]	neutron beam		0.9×10^8
Soudan [58]	^{56}Fe	0.72×10^{32}	1.3×10^8
Frejus [59]	^{56}Fe	0.65×10^{32}	1.2×10^8
Kamiokande [60]	^{16}O	0.43×10^{32}	1.2×10^8
Super-K [2]	^{16}O	1.90×10^{32}	2.7×10^8
SNO [61]	^{2}D	1.48×10^{31}	1.4×10^8

Table 2.1: Experimental lower limits on neutron's oscillation life-time in nucleon decay type of experiments. ILL Grenoble's limit is included for comparison.

The most substantial limit, see Table 2.1, on the oscillation lifetime of neutrons, is currently held by the Super-Kamiokande experiment - a water Cherenkov detector located near the city of Hida, Gifu Prefecture, Japan. Significant exposure and a low background play an important role in achieving the limit in Super-Kamiokande. The most recent result came from SNO - a neutrino observatory located 2.1 km underground in Vale's Creighton Mine in Sudbury, Ontario, Canada. SNO has drawn a quite competitive limit compared to that of Super-K despite two orders of magnitude short of exposure (2.45×10^{34} n·yr for Super-K [2] and 2.047×10^{32} n·yr for SNO [61]). The reason lies in its choice of heavy water as the active material. A deuteron ^{2}D nuclear - the source of bound neutrons in SNO's study - has only one neutron and one proton, so an oscillation will yield only a $p\bar{n}$ annihilation and there are no intra-nucleus re-absorption that distorts the final state signatures of the event. This advantage leads to higher detection efficiency. More importantly, the nuclear suppression factor of ^{2}D is four times smaller than that of ^{16}O [61].

The high energy physics community's stand regarding the neutron-antineutron oscillation search is pushing the sensitivity by 2-3 orders of magnitude in terms of the oscillation lifetime τ, see Figure 2.4. This goal could be achieved with the next-generation experiments: DUNE in the USA, Hyper-K in Japan, and ESS-$n\bar{n}$ in Europe. In the meantime, current experiments like Super-K and NOvA can still provide very competitive limits and serve as a guideline for the analyses in future experiments.

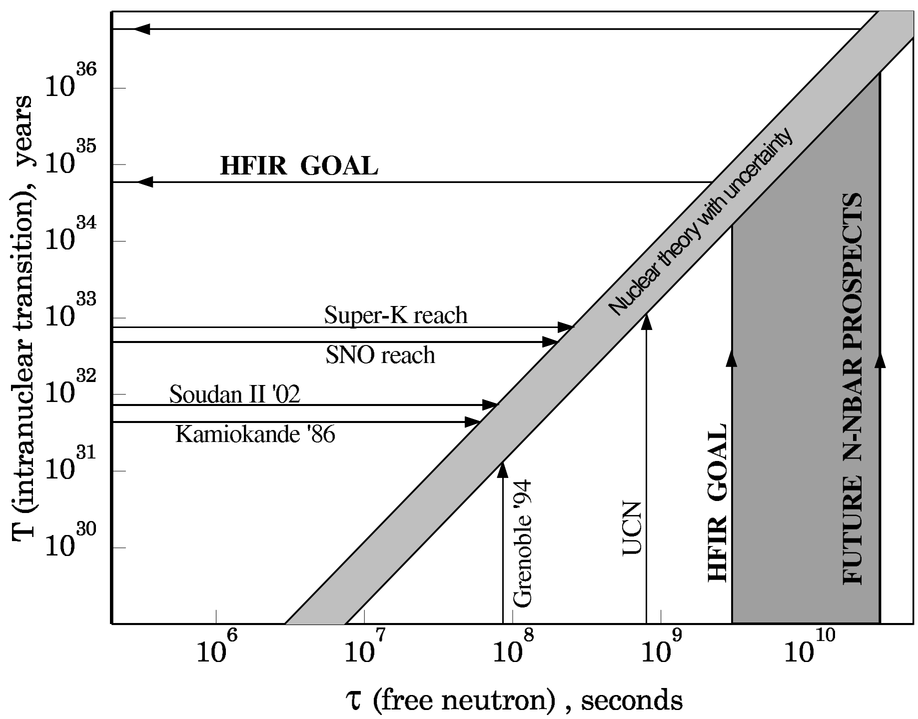

Figure 2.4: Comparison of free neutron and bound neutron methods for $n - \bar{n}$ oscillation search. Horizontal axis represents limits for characteristic transition time in experiments with free neutrons from the reactors while vertical axis represents limits for lifetime for intra-nuclear transition [6].

Chapter 3

Neutron Oscillation Search at NOvA

NOvA stands for "**N**uMI **O**ff-axis $\boldsymbol{\nu}_e$ **A**ppearance," a long-baseline neutrino oscillations experiment based at Fermilab, Batavia, Illinois. This experiment's primary goal is to study the neutrino oscillations - a quantum mechanical behavior that exposes various important characteristics of the particles, most notably their non-zero masses. In particular, NOvA was optimized for the measurements of electron neutrino and anti-neutrino appearance, which is a key to exploring the possibility of CP violation in the lepton sector and determining the neutrino mass ordering. NOvA consists of two technically identical detectors sampling a beam of muon neutrinos and anti-neutrinos produced by the Fermilab's NuMI facility (**Neu**trino at the **M**ain **I**njector). A unique trait in NOvA's design is the implementation of the off-axis neutrino beam, which enhances the sensitivity to the $P(\nu_\mu \to \nu_e)$ and $P(\bar{\nu}_\mu \to \bar{\nu}_e)$ measurements. In addition to serving as a neutrino detector, the design of NOvA enables a wide range of exotic physics studies, including the phenomenon of neutron-antineutron oscillation in particular. In this chapter, we will discuss these design choices and describe how they can assist the search for neutron anti-neutron oscillations.

3.1 Neutrino Oscillations and the NOvA Experiment

Neutrinos and anti-neutrinos have three flavours: the electron neutrinos ν_e ($\bar{\nu}_e$), the muon neutrinos ν_μ ($\bar{\nu}_\mu$) and the tauon neutrinos ν_τ ($\bar{\nu}_\tau$). A flavored neutrino is always appearing with its corresponding charged lepton in a CC interaction. The remarkable discovery of the neutrino oscillations in the late 1990s has started a vigorous exploration in the physics of the neutrino sector. Neutrino oscillations suggest that once a neutrino of a specific flavor, say ν_μ, travels a sufficiently large distance, the probability of it being detected as a neutrino of a different flavor, say ν_τ, is non-zero. The phenomenology of the oscillations between the three abovementioned flavors of neutrinos can be entirely encoded in the PMNS mixing matrix whose conventional parameterization was usually written as

$$\begin{pmatrix} c_{12}c_{13} & s_{12}c_{13} & s_{13}e^{-i\delta_{\rm CP}} \\ -s_{12}c_{23} - c_{12}s_{13}s_{23}e^{i\delta_{\rm CP}} & c_{12}c_{23} - s_{12}s_{13}s_{23}e^{i\delta_{\rm CP}} & c_{13}s_{23} \\ s_{12}s_{23} - c_{12}s_{13}c_{23}e^{i\delta_{\rm CP}} & -c_{12}s_{23} - s_{12}s_{13}c_{23}e^{i\delta_{\rm CP}} & c_{13}c_{23}. \end{pmatrix} \quad (3.1)$$

The symbols c_{ij} and s_{ij} stand for the $\cos\theta_{ij}$ and $\sin\theta_{ij}$ where θ_{ij} is one of the three mixing angles θ_{12}, θ_{23} and θ_{13}. The angle $\delta_{\rm CP}$ is the CP-violation phase. The question whether $\delta_{\rm CP} \neq 0$ is currently among those of uttermost importance in neutrino physics.

If only a specific flavour can be detected in an experiment and it takes part in the oscillations, one would expect a deficit or also called a disappearance of that flavour at the detection point. The disappearance of solar ν_e, also known as the solar neutrino anomaly, has been observed at several solar neutrino observatories like Homestake [62], Kamiokande [63] , Super-Kamiokande [64] and SNO [65, 66], as well as radio-chemical experiments such as SAGE [67], GALLEX [68, 69] and GNO [70]. The disappearance of reactor $\bar{\nu}_e$ was suggested by the Double Chooz experiment [71] and since then confirmed by the KamLAND [72, 73], the Daya Bay [74–76] and the RENO [77] experiments. The disappearance of ν_μ and $\bar{\nu}_\mu$ produced by the decays of π/K mesons in the secondary cosmic rays, also known as the atmospheric neutrino anomaly, has been suggested in early nucleon decay experiments like IMB [78], Kamiokande [79] and Frejus [80], and has been confirmed by the Super-Kamiokande experiment [81, 82]. The disappearance of man-made ν_μ and $\bar{\nu}_\mu$ has been observed in many long base-line neutrino oscillations experiments including K2K [83], MINOS [84–86], T2K [87, 88] and OPERA [89]. A list of neutrino disappearance experiments and their measurement channels is given in Table 3.1. A noble recognition for the discovery of oscillations of atmospheric neutrinos and solar neutrinos is the 2015 Nobel Prize awarded to Takaaki Kajita from the Super-Kamiokande collaboration and Arthur McDonald from the SNO Collaboration.

Many neutrino detectors can identify more than one neutrino flavour, usually ν_e and ν_μ. In these experiments, one can observe the appearance of a neutrino flavour that is not produced at the source. Two experiments T2K [90] and MINOS [91] were the first to show empirical data consistent with $\nu_\mu \to \nu_e$ oscillations. Strong evidence of ν_e appearance has been presented by T2K [92]. Notably, the detectors in two experiments Super-Kamiokande [93] and

Neutrino Disappearance Experiment	
Solar ν_e	Homestake [62]
	Kamiokande [63]
	SAGE [67]
	GALLEX [68, 69]
	GNO [70]
	Super-Kamiokande [64]
	SNO [65, 66]
Reactor $\bar{\nu}_e$	KamLAND [72, 73]
	Daya Bay [74–76]
	RENO [77]
Atmospheric $\nu_\mu/\bar{\nu}_\mu$	IMB [78]
	Kamiokande [79]
	Frejus [80]
	Super-Kamiokande [81, 82]
Accelerator $\nu_\mu/\bar{\nu}_\mu$	K2K [83]
	MINOS [84–86]
	T2K [87, 88]
	OPERA [89]

Table 3.1: List of notable neutrino disappearance experiments.

OPERA [94] allow the identification of ν_τ CC interactions and have provided indications of $\nu_\mu \to \nu_\tau$ oscillations.

NOvA is a US-based long-baseline neutrino oscillations experiment. Like its predecessor MINOS, it utilizes the muon neutrino and anti-neutrino beam from the Fermilab's NuMI facility. It comprises of two technically identical liquid scintillator detectors. One of them - the Near Detector (ND) - is placed at the Fermilab, where the NuMI's neutrinos come from, measuring the initial beam composition, and constraining the flux. The other one - the Far Detector (FD) - locating 810 km away at Ash River, Minnesota measures the beam's oscillated spectrum. NOvA is able to conduct measurements of both $\nu_\mu/\bar{\nu}_\mu$ disappearance and $\nu_e/\bar{\nu}_e$ appearance probabilities, allowing the constraints of the atmospheric sector oscillation parameters Δm^2_{32} and $\sin^2\theta_{23}$ with high precision, see Figure 3.1. Determining experimentally if the θ_{23} is exact $\pi/4$ (the maximal mixing scheme) would provide theorists with important leverage to recognize new discrete symmetries in the electroweak sector, which in turn leads to new insights of its dynamical structure and the neutrino mass generation mechanisms [95].

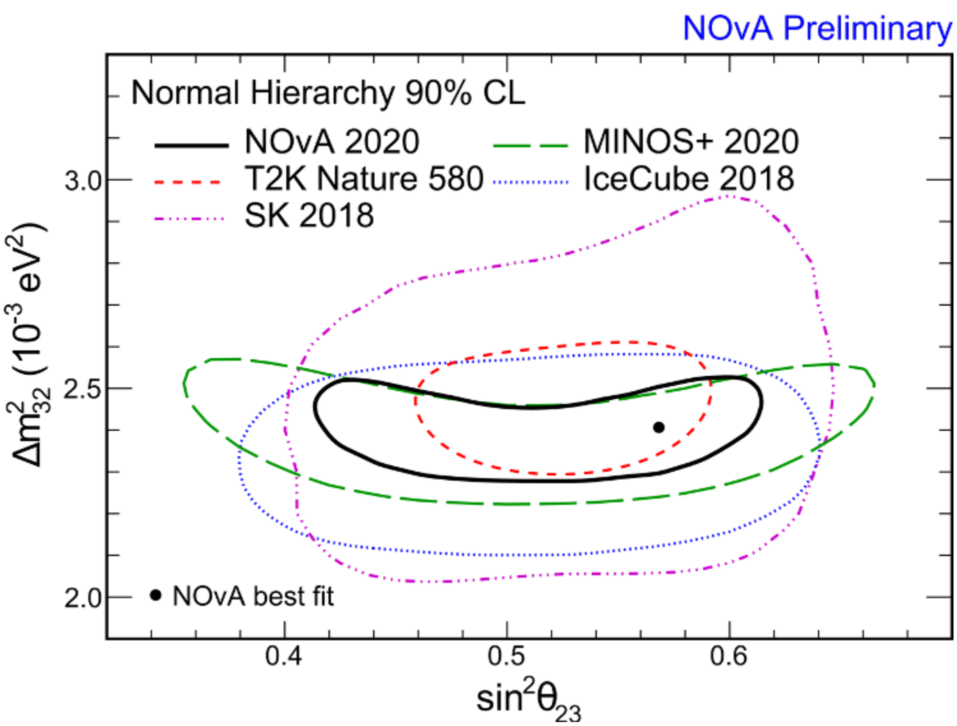

Figure 3.1: The 90% confidence level region for Δm^2_{32} and $\sin^2\theta_{23}$, with best-fit shown the by black marker, overlaid with results from other experiments. Taken from [7].

More importantly, NOvA set goals to explore the CP violation in the lepton sector via the measurement of the phase angle δ_{CP} as well as to resolve the neutrino mass ordering. To achieve this, NOvA measure precisely and compare the $\nu_\mu \to \nu_e$ and the $\bar{\nu}_\mu \to \bar{\nu}_e$ oscillation probabilities, see Figure 3.2. A couple of difficulties in measuring these oscillation probabilities have been identified in the previous effort - the MINOS experiment. First, the detector requires enough granularity to sample and distinguish the electromagnetic showers and the hadronic showers from the $\nu_e/\bar{\nu}_e$ CC interactions. Second, the background which, in this case, comes from the NC interactions of high energy neutrinos resembling lower energy CC interactions, needs to be suppressed. These issues have been addressed in the NOvA experiment by (i) choosing low-Z materials for the detector construction and (ii) implementing the off-axis beam design. The first result on the constrain of CP-violation [96] excludes δ_{CP} from -0.04 to 0.97π for the lower θ_{23} octant and from 0.04 to 0.91π for the upper θ_{23} octant by more than 3σ, assuming the inverted hierarchy (IH), see Figure 3.3. The data also prefer the normal hierarchy (NH) with a significance of 1.9σ and the upper θ_{23} octant with a significance of 1.6σ [96].

Besides the main focus on neutrino oscillations, NOvA is able to perform a wide range of studies including neutrino cross-section measurements [97, 98], sterile neutrino search [99], multi-messenger astrophysics [100, 101] and search for exotic physics phenomena. The focus of this thesis is on the search for neutron anti-neutron oscillation using the

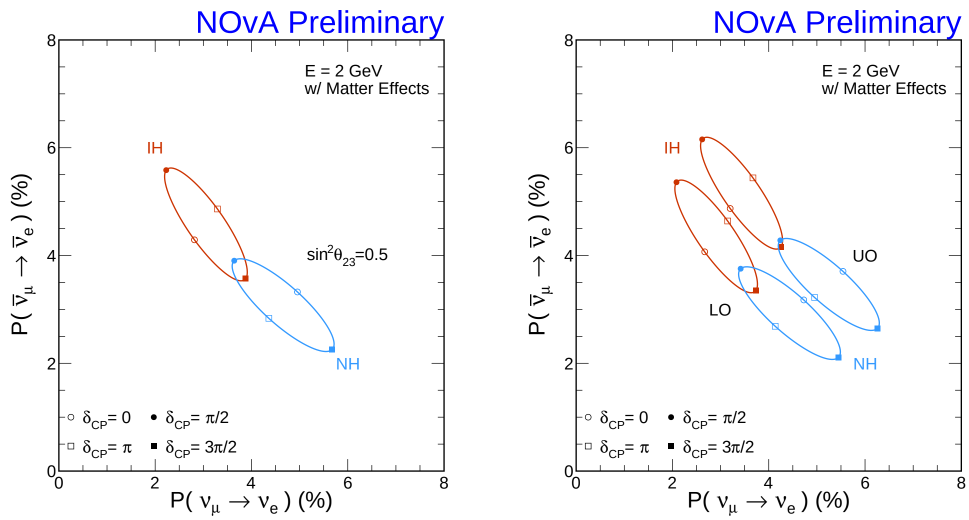

Figure 3.2: Bi-probability plots of ν_e and $\bar{\nu}_e$ appearances in the NOvA experiment [8]. The blue and red ellipses show the appearance probabilities for the normal (NH) and inverted (IH) mass ordering, respectively. The effect of CP violation is depicted by the ellipse, whose each point represents a different value of δ_{CP}. The plot on the left assumes the maximal mixing scenario where θ_{23} at $\pi/4$, while the plot on the right shows the contrast when the angle lies in different octants.

NOvA Far Detector. In the following sections, the design of NOvA detectors will be described and analyzed to explain why it can assist the search of $n\bar{n}$. As the study presented in this thesis is conducted using only the FD data, the following sections will engage solely in the physical design, the data acquisition (DAQ), and the trigger systems for the FD. Discussions about the NuMI beam, which is relevant exclusively for the physics of neutrino oscillations, are also omitted.

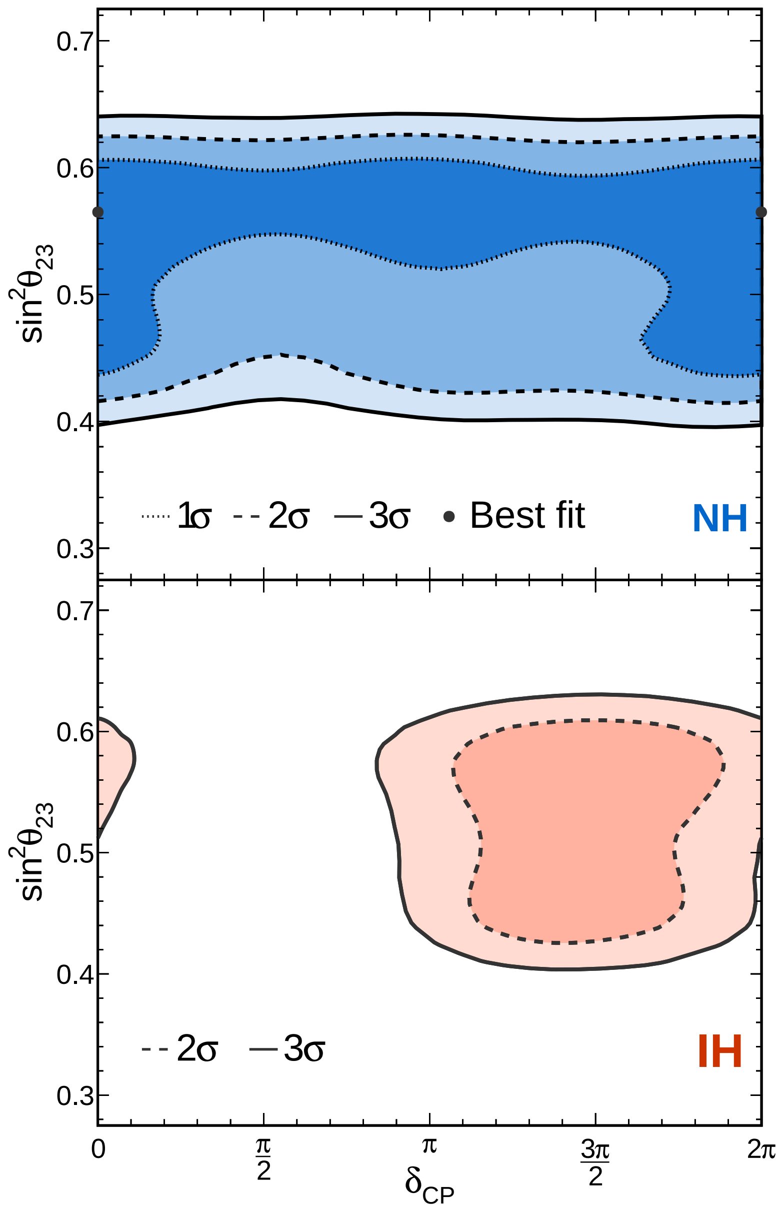

Figure 3.3: The $1\sigma, 2\sigma$ and 3σ C.L. contours in $\sin^2\theta_{23}$ vs $\delta_{\rm CP}$ in the NH (top) and IH (bottom) together with the best-fit point shown by the black marker.

3.2 The NOvA Detectors

As mentioned in the previous section, serving as a long-baseline neutrino oscillation experiment, NOvA comprises two detectors: the ND and the FD. The detectors' primary function is to identify the flavor and measure the energy for each neutrino coming to them from the beam. The unoscillated energy spectra for each flavor measured at the ND are then extrapolated to get the FD prediction. In order to alleviate the effect of systematic uncertainties, the two detectors are designed to be almost identical in terms of physical construction and DAQ architecture.

3.2.1 Mechanical Design

NOvA detectors are constructed from extruded PVC cells whose lengths span the full transverse dimension of the detector. Several modules, which are array compilations of 16 cells, are glued together side-by-side to make a square plane. Planes with cell's orientation perpendicular to each other are then sandwiched to compose a larger detector block (32 planes for FD and 24 planes for ND), see Figure 3.4. The alternative orthogonal planes setup allows the reconstruction software to perform 3D tracking of particles when they traverse multiple planes. The planes of vertical and horizontal modules provide the so-called top-view (X-view) and side-view (or Y-view) of an event display. The NOvA Far Detector in Ash River, Minnesota, consists of 896 planes containing 344,064 cells, each of which is 15.5 m long. The full detector dimensions extend approximately $15.5\,\mathrm{m} \times 15.5\ \ \mathrm{m} \times 60.0\,\mathrm{m}$. After filled with the liquid scintillator, the total mass of the FD is about 14 ktons.

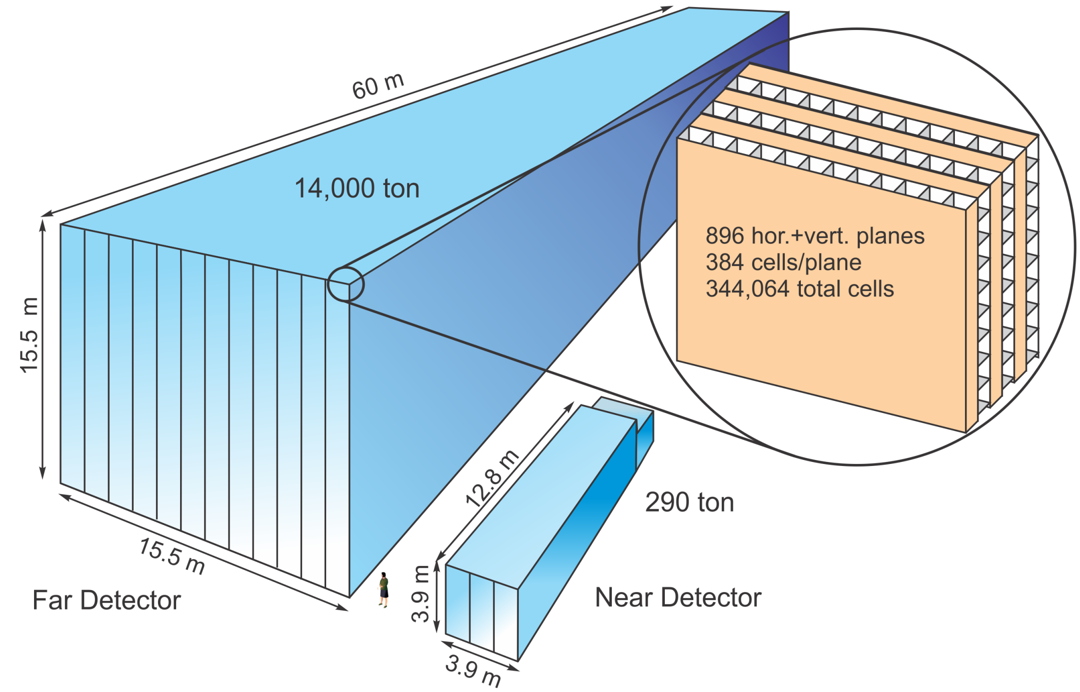

Figure 3.4: The inset figure (dotted circle) shows that each detector has an identical alternating plane structure composed of vertical and horizontal cells [9].

Aiming specifically to enhance the performance of ν_e appearance measurement, NOvA detectors need enough granularity to distinguish the EM showers due to interactions of electrons and gammas. Two numbers characterize the topology of an EM shower: the Moliere radius R_{M} and the radiation length X_0, which dictate the transverse and longitudinal dimensions of the shower, respectively. The choice of low Z material means a larger R_{M} and a larger X_0. For NOvA, R_{M} is 11 cm or about the width of 3 cells. The transverse dimension of an electron shower will then extend up to

3 cells on average. This makes the distinguishing a shower from a non-showering particle track much easier. Similarly, the value of X_0 is approximately 40 cm, or equivalent to the length of 6 planes. This becomes important in the identification of π^0s. When a π^0 is created in a neutrino interaction, it almost immediately decays into two gammas which, on average, would travel a distance of about $1.3X_0$ before pair-productions. A gap between the vertex and a shower due to a large X_0 is the characterizing signature of a π^0 in the NOvA detectors, distinguishing it from an electron, see the bottom panel in Figure 3.5.

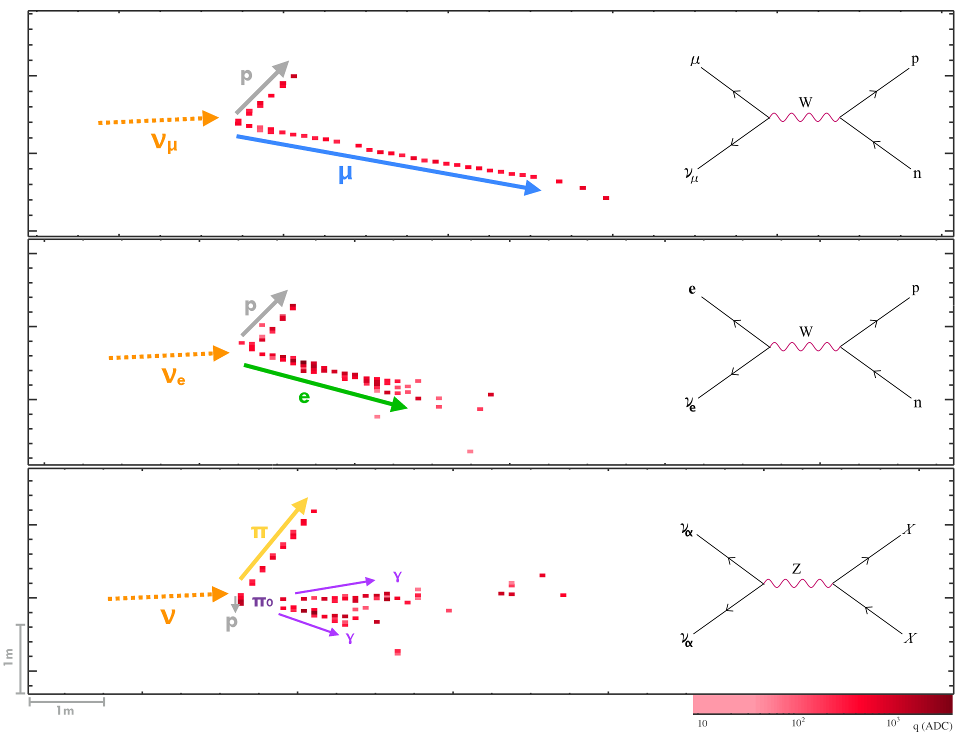

Figure 3.5: Example event topologies from data files [10]. Top: selected ν_μ ND event. Middle: selected ν_e ND event. Bottom: selected π^0 ND event.

3.2.2 The NOvA Cell

The building block and also the smallest readout unit of the detectors is the NOvA cell, see Figure 3.6 [102]. The basic element of this design is a long plastic tube filled with liquid scintillator and equipped with an optical fiber to capture the scintillation light produced when a charged particle passes by.

A cell has inner dimensions of $3.8\,\text{cm} \times 5.9\,\text{cm}$. The thickness of the walls varies from 2 to 5 mm due to differences in the mechanical stability requirements between vertical-cell and horizontal-cell planes [103]. The length of the cell is 15.5 m for the FD, and 4.0 m for the ND. The material that made up the cells is PVC doped with TiO_2 to increase the cell's inner surface's reflectivity. Optical simulation of the detector [104] indicated that the scintillation light bounces off the walls of a cell nine times on average before being absorbed by the WLS fiber. An increase in reflectivity of the cell will immensely improve the light collection efficiency. The PVC skeleton accounts for about 35% of the total mass of the detectors. Some important mechanical design parameters of the FD is given in Table 3.2.

3.2.2.1 The Liquid Scintillator

The remaining 65% of the mass comes from the liquid scintillator used to fill the cells' inner. This scintillator is made up of three components. First of all, pseudocumene (1,2,4-trimethyl-benzene), as the main scintillant, produces UV light when ionizing particles are passing through it. Second,

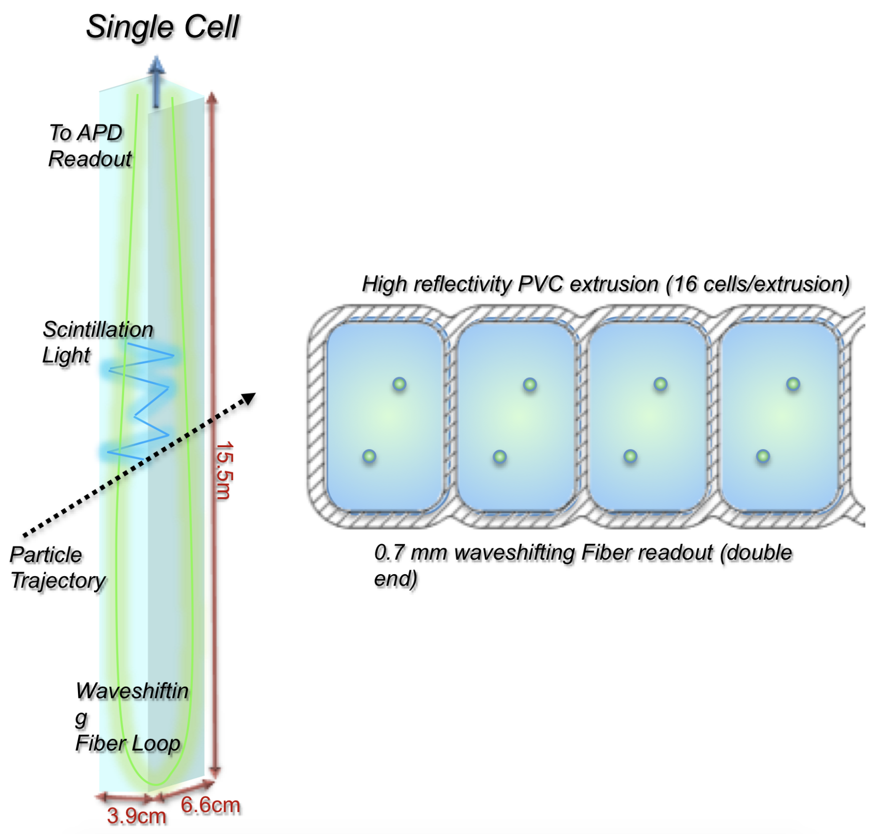

Figure 3.6: For the Far Detector, the readout cell is 15.5 m long. It is a PVC tube formed by extrusion and filled with liquid scintillator. Each extruded module encloses 16 cells. A loop of wavelength-shifting (WLS) fiber is embedded in the scintillator to collect and transport the scintillation light to an avalanche photodiode located at one end of the cell.

two waveshifters - PPO (2,5-diphenyloxazole) and bis-MSB (1,4-dimethylstyryl-benzene) - downshift the UV photons to longer wavelengths to facilitate absorption by the wavelength shifting fibers. The light production chain is detailed in Figure 3.7 with data from [105]. The last component is a solvent of mineral oil doped with a trace amount of

Quantity	Value
Number of planes	896
Cells per plane	384
Cell depth [1]	5.64 cm
Cell width	3.60 cm
Dimension (X)	[-758 cm, 765 cm]
Dimension (Y)	[-749 cm, 765 cm]
Dimension (Z)	[0 cm, 5962 cm]

Table 3.2: Summary of the NOvA's FD mechanical design.

antioxidant (vitamin E) and antistatic[2] agents (Stadis-425) that hold all the components in a stable solution. The composition of the NOvA liquid scintillator is summarized in Table 3.3.

Component	Mass Fraction	Volume (gal)	Total Mass (kg)
mineral oil	95.8%	3,082,145	9,917,109
pseudocumene	4.1%	128,439	425,908
PPO	0.091%		9,373
bis-MSB	0.0013%		131
Stadis-425	0.0003%		46.6
tocopherol (Vit.E)	0.0010%		104
Total	100.0%	3,210,584	10,352,551

Table 3.3: Composition of the NOvA liquid scintillator [1].

[2]The liquid scintillator is extremely non-conductive. A non-conductive fluid will develop a net charge through the triboelectric effect during flow, which can lead to sparking at the liquid-container interface. In order to avoid the sparkings, the anti-static agent was added to the scintillator mixture to bring the scintillator conductivity up to safe levels.

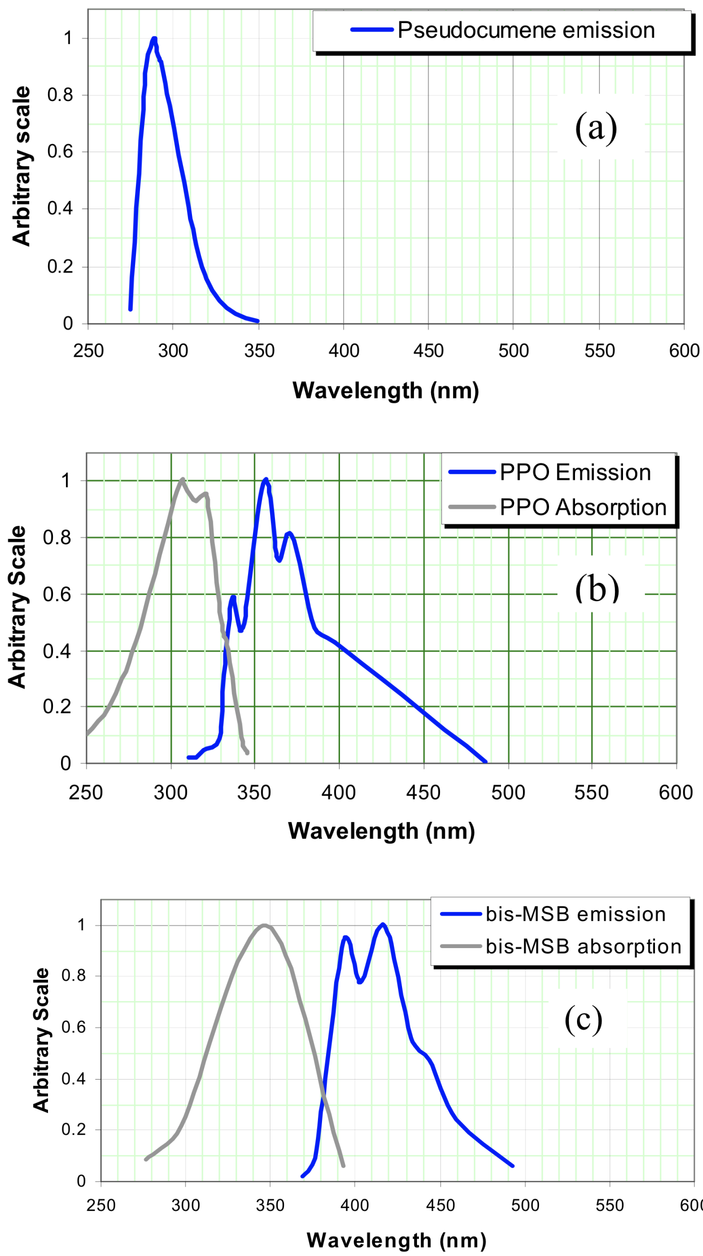

Figure 3.7: Light production by the NOvA liquid scintillator [1]. The emission spectrum of pseudocumene when traversed by an ionizing particle in (a); the absorption and emission spectrum of the first wavelength shifter PPO in (b); and the absorption and emission spectrum of the second wavelength shifter bis-MSB in (c).

3.2.2.2 The Wavelength-Shifting Fiber

In order to collect and transport the scintillation lights to the photosensor, each cell is equipped with a looped optical fiber. NOvA chose the multi-clad WLS fiber Y-11 from Kuraray [106], which has been previously utilized in the optical readout system of many large-area scintillation counters. The fiber's diameter is 0.7 mm, and for the FD, the fiber's length is about 31 m. The fiber has a core made of polystyrene (refractive index $n = 1.59$), with an acrylic inner cladding ($n = 1.49$) and a fluorinated-polymer outer cladding ($n = 1.42$). The outer cladding increases the acceptance angle for the internal reflection, thus enhancing the fiber's transmission.

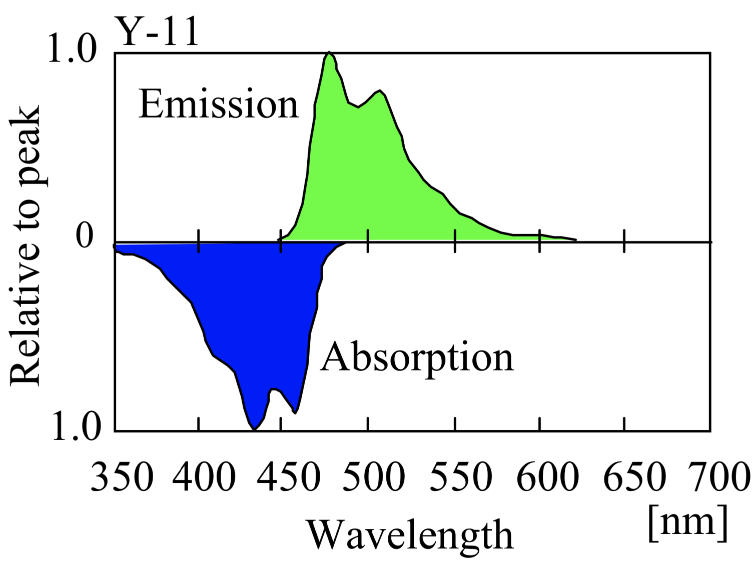

Figure 3.8: The absorption and emission spectra of the K27 dye used in Kuraray Y11 fibers.

The Kuraray Y-11 fibers use the K-27 fluorescent dye as the wavelength-shifting agent. The absorption spectrum of this dye is well matched to the emission spectrum of the NOvA liquid scintillators. The dye shifts the absorbed light toward the green region of the spectrum, from 450 nm to 550 nm, with the emission peak at 476 nm [106]. However, an overlap of the absorption spectrum and the emission spectrum exists, as seen in the top panel of Figure 3.8. As a result, the wavelengths shorter than 490 nm will attenuate out severely as the distances that photons have traveled increase. The result is a spectrum shifting toward even longer wavelengths after passing through typical lengths of fiber [1]; see the bottom panel in Figure 3.8.

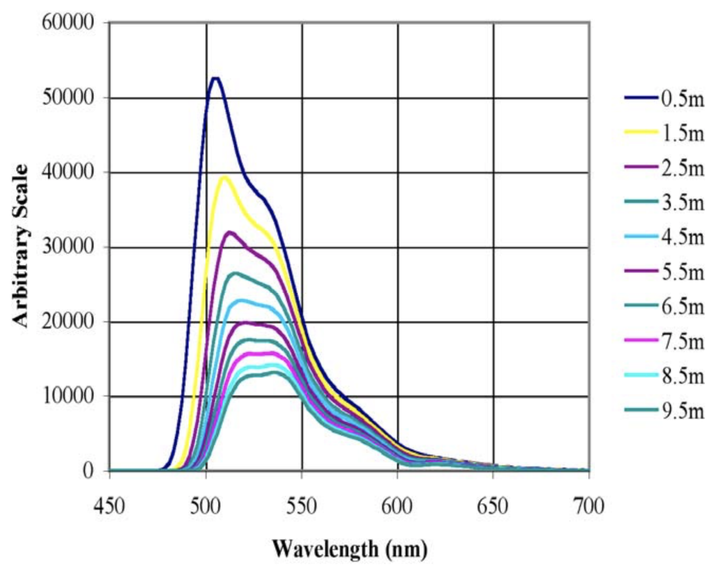

Figure 3.9: Spectrum of light exiting a 0.7 mm Y-11 fiber stimulated at distances from 0.5 m to 9.5 m.

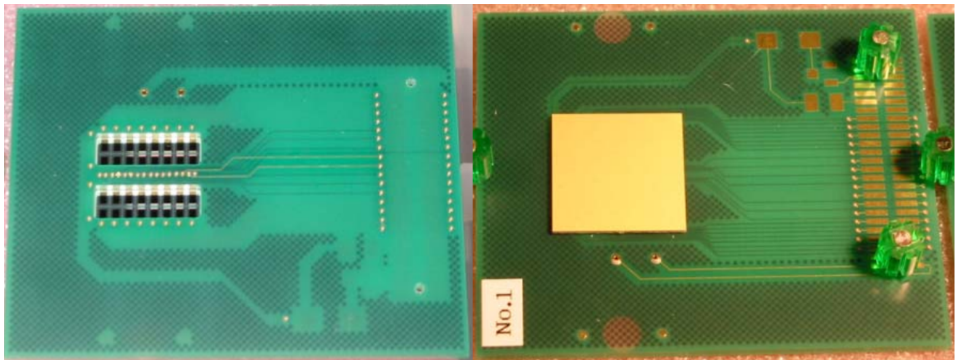

Figure 3.10: Front and back views of an APD carrier board showing the array of 32 pixels on a single chiplet.

3.2.2.3 The Avalanche Photo-Diode (APD)

At the end of the detection chain is a photosensor whose job is to transform the light signal from the fiber to an electronic signal ready to be further processed by the DAQ system. A custom-made version of Hamamatsu's S8550 APD is the choice of photosensor used in the NOvA experiment. There are 32 pixels mounted on each APD array; see Figure 3.10. The size of each pixel has been manufactured exclusively for NOvA to fit two fiber ends on each pixel. Total 32 pixels on an APD array map directly to 32 cells of each PVC extrusion module. The general performance parameters of an APD is shown in Table 3.4. The device's quantum efficiency is about 85% for wavelengths between 520 nm, and 550 nm, which are delivered by the WLS optical fibers. These APDs typically operate between 350 V - 450 V with a current of few nA per array (all 32 channels). The signal gain factor at this operational voltages is on the order of 100. To reduce thermal noise, which can mimic the physics signal, the APDs are

Pixel Active Area	1.95 mm − 1.0 mm
Pixel Pitch	2.65 mm
Array Size	32 pixels
Die Size	15.34 mm − 13.64 mm
Quantum Efficiency (> 525 nm)	85 %
Pixel Capacitance	10 pF
Bulk Dark Current (l_8) at 25°C	< 50 pA
Bulk Dark Current (l_8) at −15°C	< 2.5 pA
Peak Sensitivity	600 nm
Operating Voltage	375 ± 50 V
Gain at Operating Voltage	100
Operating Temperature (with TEC)	−15°C
Expected S/N Ratio (μ at far end of cell)	10:1

Table 3.4: Parameters of the NOvA Avalanche Photo-Diode [1].

cooled to -15° C using a thermal-electric cooler (TEC) device controlled by the front-end electronic board.

3.2.3 The Data Acquisition System

3.2.3.1 An Overview of the DAQ of the NOvA's FD

The core measurements of the NOvA experiment are $\nu_\mu \rightarrow \nu_e$ and $\bar{\nu}_\mu \rightarrow \bar{\nu}_e$ oscillation probabilities. The neutrinos of the NuMI beam will interact and leave characteristic signatures corresponding to their flavours in both detectors. The DAQ system has to correlate a recorded interaction with the actual beam pulse that caused it. This task is not trivial for the NOvA experiment design.

First, there exists no cable system for timing signal over 810 km from Fermilab to the Ash River that is fast enough to trigger the readout of the

FD at the arrival of a beam spill. The readout needs to happen independently of any knowledge of the beam conditions. This means the data needs to be buffered long enough to wait for any beam spill information to reach the FD site eventually. Second, due to the everchanging operational conditions of the Fermilab's accelerator complex, it is impossible to tell when a beam spill will arrive at the FD, nullifying the possibility of a predictive triggering scheme. Last but not least, the FD always witnesses busy detector activities since it is located on the surface and exposed to a high rate of cosmic rays. This makes activity-based triggering extremely inefficient. Without knowing the exact beam spill window, most beam neutrino interactions will be completely shadowed under a sea of cosmic particles penetrating the detector constantly.

The NOvA data acquisition (DAQ), therefore, operates in a readout mode where "snapshots" of the whole FD are continuously streamed into a computing server located on-site, which serves as a buffer zone for the data. A snapshot indicates the aggregated data from every APD channel, enough to capture all the physics happening in the detector during a specific time window. Those snapshots sit and wait to be further analyzed by a collection of trigger algorithms[3] at the buffer nodes. Each trigger scans through a snapshot, looking for a specific set of physics signatures. If the snapshot contains relevant physics information, it will be kept and transferred to permanent storage. Otherwise, it will be discarded.

[3]One of which handles the NuMI beam spill trigger.

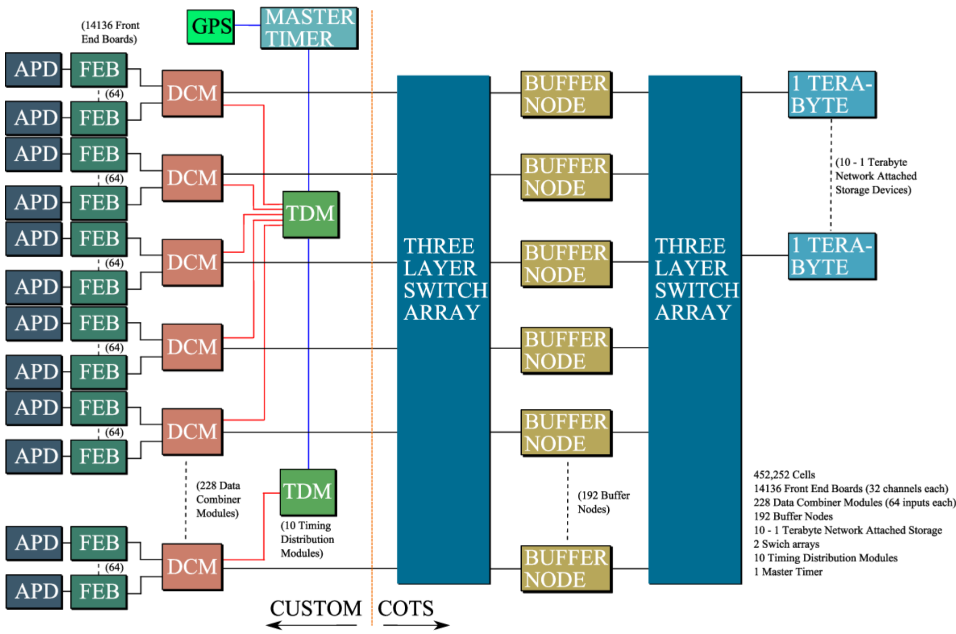

Figure 3.11: NOvA Data Acquisition System [11].

The formation of these snapshots starts at the front-end boards (FEBs) where all the hits in the APDs above a noise threshold will be conditioned, digitized, and time-stamped. Each FEB is summing the information of 32 channels from a single module of 32 cells. The FEBs send their information down to the data concentration modules (DCMs) to form bigger, synchronized data packets that are ready to be transmitted directly to the buffer farm via Gigabit Ethernet. Timing synchronization for these DCMs is handled by chains of Timing Distribution Units (TDU) consisting of one master node (MTDU) and 14 slave nodes (STDU). A cartoon describing the data stream of the DAQ system is shown in Figure 3.11. Once DCMs' data arrived at the buffer farm, specialized software will join them together and form the so-called miliblock that presents a snapshot of the entire detector during a 5 ms time window. Next, trigger algorithms (which will be discussed in detail in Chapter 5) would analyze this milliblock to decide whether or not it contains relevant physics information and should be kept.

This DAQ design tolerates extremely long latency in the propagation of the information about the beam. In parallel to the readout, a spill occurring at NuMI is timestamped with a counter synchronized to the NOvA's timing system. When this information finally reaches the FD site, a special trigger dedicated to the NuMI beam will search through all the buffered snapshots looking for any overlaps with the spill. This design brings about advantage as it provides a readout system without any dead time. This deadtimeless makes the detector sensitive to interactions from not only the NuMI beam but also external sources such as cosmic rays, atmospheric or cosmic neutrinos, theorized exotic particles like magnetic monopoles, as well as theorized new physics processes such as neutron antineutron oscillation.

The following sections will describe each component of the DAQ system for the NOvA detectors carefully.

3.2.3.2 Front-End Electronics

The first stage of the DAQ is interfacing between the analog signal section and the digital processing section. This step is executed on a custom-made front-end electronic board (FEB). Besides processing the data, the FEB carries the necessary components to control precisely the high voltage to the

APDs and the current to drive the TEC that cools the APDs. A block diagram of the FEB's design is shown in Figure 3.12.

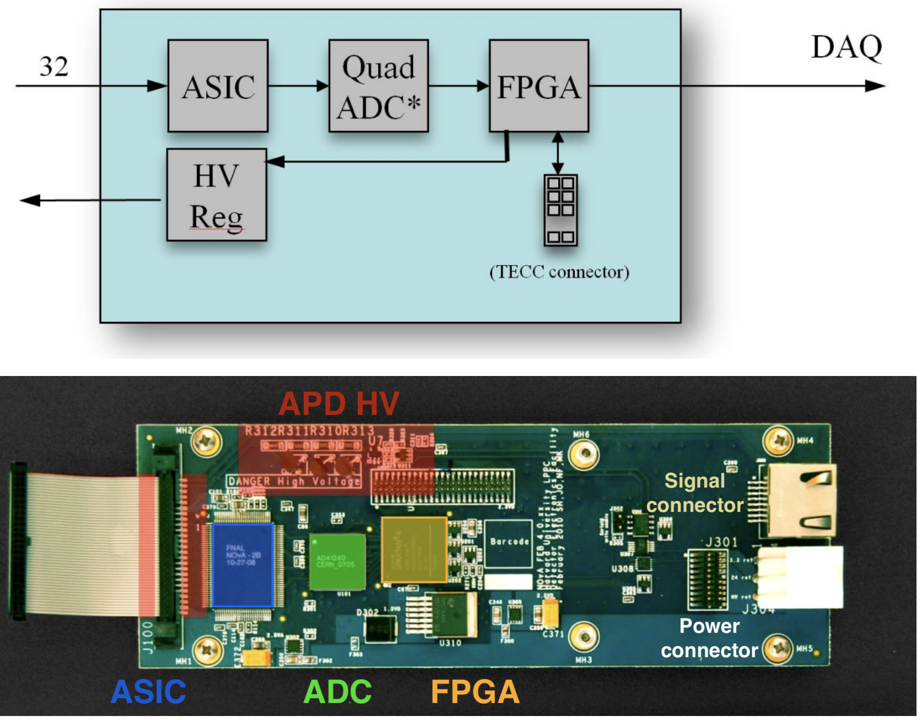

Figure 3.12: Block diagram of NOvA FEB components (top) and picture of a prototype FEB (bottom) showing the arrangement of these components on a PCB. Taken from [12].

The data processing section of this board features a custom low-noise ASIC, a semi-custom ADC device called AD41240 made by CERN Microelectronics and a private company named ChipIdeas, and a commercial Spartan 6 FPGA from Xilinx. The job of the ASIC is to amplify and shape the analog electrical signals from the APDs. It is designed to condition small signals that underwent the attenuation along the 31 m-long fibers in the FD.

The schematic of the NOvA's custom ASIC is shown in Figure 3.13. The signal from 32 APD channels is then multiplexed to the AD41240. This is a 12-bit ADC with 8 input channels sampling at a rate of 16 MSPS. An 8:1 multiplexing scheme is utilized so that each APD channel can be sampled at 2 MSPS (or every 500 ns) [4].

The third component - the Xilinx's FPGA does all the heavy lifting of digital signal processing, which includes triggering the signal, compressing the signal via zero-suppression, time-stamping, and buffering the data. The FPGA also provides control and monitoring of the TEC that cools the APDs, the high voltage that powers the APDs as well as the external interface to the DCMs using a custom protocol over inexpensive CAT5 cabling. The data packets that the FEBs send to the DCMs are called nanoslices [107].

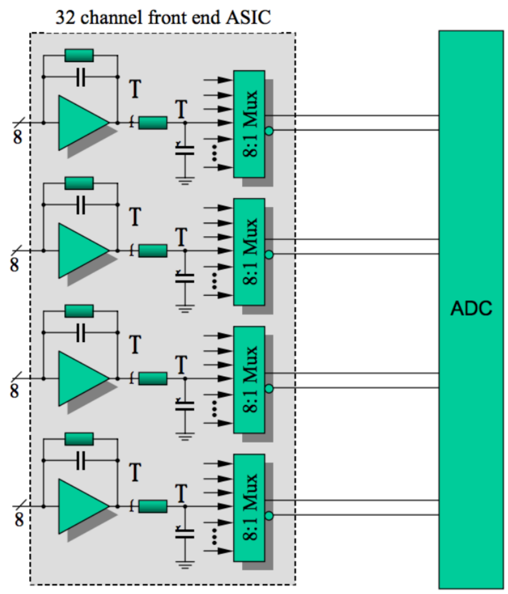

Figure 3.13: Schematic of the NOvA's custom ASIC [1].

Figure 3.14: Picture of the front panel of a DCM showing 64 Ethernet connection ports to FEBs.

3.2.3.3 Data Concentration Module

Data Concentration Module boards (DCMs) form the backbone of the DAQ system for the NOvA detectors. In the FD, there are a total of 168 DCMs coordinating the flow of data from 344,064 individual readout channels. They are grouped into 14 major detector sections called diblocks; each comprises of 6 DCMs for the vertical-oriented modules and other 6 DCMs for the horizontal-oriented modules, see Figure 3.15. Every DCM is a custom computer designed to collect serial nanoslices from up to 64 FEBs, see Figure 3.14. The DCMs first align and concatenate the nanoslices into a properly synchronized time window of 5 μs in length, which is called a microslice. A series of time-ordered microslices are further packetized to form a 5 ms time window called a milislice. The reason behind the existence of the milislice is that this load is usually 8-9 kB in size[5], which is optimum to

[4]The FEBs for the FD and the ND are not the same. The essential difference is the sampling rate. While the FD can function reasonably well at 2 MSPS, the ND needs at least 8 MSPS to keep up with busy detector activities during the beam spills window. Two things are required to address this issue for the ND. First, the ASIC must be capable of switching from an 8:1 multiplexing (slow mode) where one ADC channel is shared across 8 APD channels, to a 2:1 multiplexing (fast mode) where the ADC samples only 2 channels at the same time. A modified ASIC version implemented in the ND has this feature built-in. Under the 2:1 multiplexing, the sampling rate is 8 MSPS (or 125 ns per sample). In contrast, in the FD, a 16 MSPS ADC is always multiplexed up to 8 ways, for an equivalent 2 MSPS (or 500 ns per sample) for each APD channel. The second difference between the ND and FD is the choice of the ADC that digitizes the signals. The FEBs equipped for the ND use the commercial octal 12-bit ADC AD9222 from Analog Devices instead of the semi-custom device from CERN. The two ADCs are quite similar in terms of specification, with both being 8-channel 12-bit 16 MSPS (technically AD41240 is a 4-channel with two parallel outputs operating at double data rate). The CERN's AD41240 was chosen for the FD purely out of economic concern since it was available inexpensively in large quantities as surplus from the CMS experiment.

[5]This compact size is attained thanks to the zero-suppression performed at the FEB.

utilize a jumbo frame Ethernet protocol chosen for the data transmission between DCMs and buffer nodes [107]. Besides the data packetizing, a DCM extends the relative 32-bit high-resolution timestamp in a nanoslice to an absolute 56-bit timestamp in a microslice. This allows a timing system operating at 64 MHz (15.625 ns per tick) to encode up to 1.1 billion seconds or 35 years worth of ticks [108].

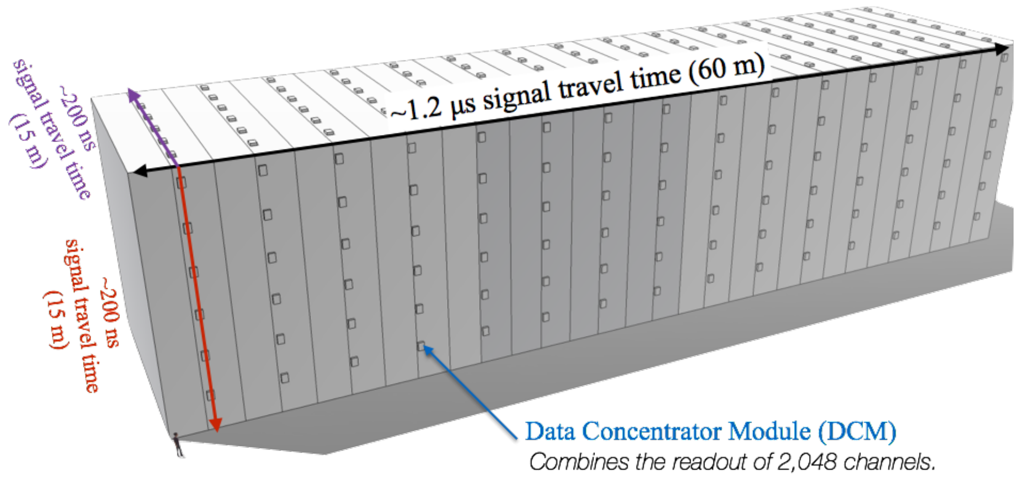

Figure 3.15: The NOvA FD is composed of 14 diblocks. Each diblock is about 1-kton in mass and contains 2048 readout cells in total. 12 DCMs are assigned to each diblock with 6 on the side handle the planes of horizontal modules (producing Y-view) while the other 6 on top handle the planes of vertical modules (producing X-view). Taken from [13].

Importantly, DCMs also works as a bridge for timing and control commands between the timing chain and individual FEBs. The role of DCMs in the timing system of the NOvA detectors will be explained in the next section.

3.2.4 Timing system

The timing system is essential to ensure the smooth operation of the DAQ and data integrity in the NOvA experiment. This system has to fulfill two primary tasks: (i) synchronizing the timing of 344,064 individual readout channels to provide proper tracking of particle interactions and (ii) marking the exact window of the NuMI spills required to perform beam neutrino trigger after the fact in the buffer nodes. The latter aspect of the timing system will not be discussed in this thesis as it is relevant solely for the studies of beam-related physics.

The timing system in NOvA is a hierarchical structure featuring custom hardware, which includes the timing distribution units (TDUs) and dedicated timing circuitries built-in on the DCMs and the FEBs. These devices are organized in a tree topology called a timing chain portrayed in Figure 3.16.

Each timing chain starts with a single master TDU (MTDU). It is linked to a GPS receiver from which it derives the absolute time. Directly under this unit is 14 slave TDUs (STDUs) that cover the detector's full length. Each STDU is daisy-chained to neighboring ones [6] via a copper cable that carries (i) a master `CLOCK`, (ii) a `COMMAND` channel, (iii) a `SYNC`, and (iv) a `SYNC RETURN`. A loopback is installed on the outermost STDU to allow the calibration of timing delay. One STDU is assigned to each diblock, bridging the 12 DCMs that handle the readout of that detector section to the rest of the chain. In

[6] An exception is the wiring between the MTDU and the first STDU due to the long distance between the two. This connection is established via a single-mode optical fiber.

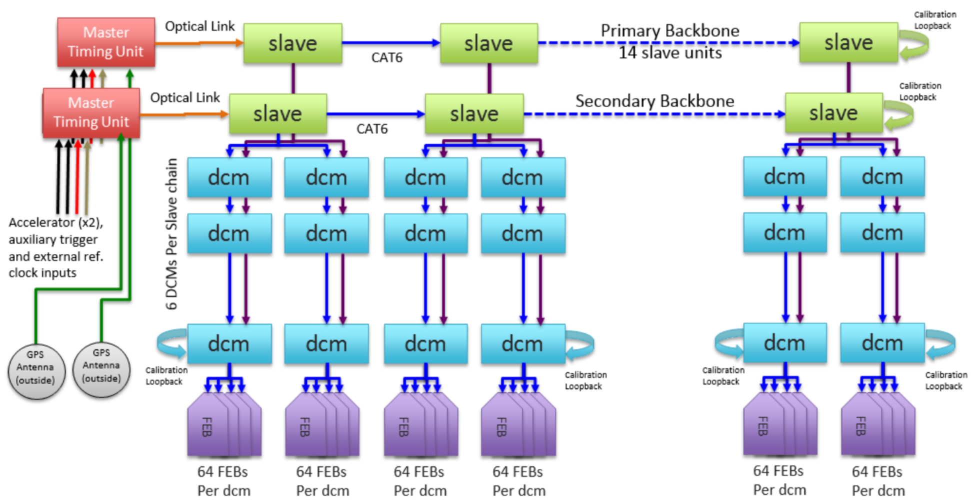

Figure 3.16: The arrangement of components (master TDU, slave TDUs, DCMs, and FEBs) in the NOvA's timing chains [14]. Each detector employs two identical timing chains in which one in use and the other serves as a fail-safe.

turn, those DCMs are daisy-chained in two separate groups with 6 DCMs corresponding to each view (top and side views) of the detector. Again, on the outermost DCM, a loopback is installed for delay calibration purposes. The FEBs are the most peripheral components on the timing chain. A total of 32 of them are connected to each DCM by the same copper cables that interconnect the rest of the system. A major difference here is the replacement of the `SYNC RETURN` line by a high-speed serial `DATA` line which carries the APD hit information from the FEBs to the DCMs.[7]

[7]Without the SYNC RETURN, the delay of a signal propagating along a FEB-DCM link could not be calibrated individually for each link. As a solution, all FEB-DCM links are manufactured exactly the same length.

To correctly reconstruct the interactions in the FD, every single readout channel needs to be synchronized to a universal NOvA wall clock. Figure 3.17 shows what happens to the event display when the FD is not properly synced.

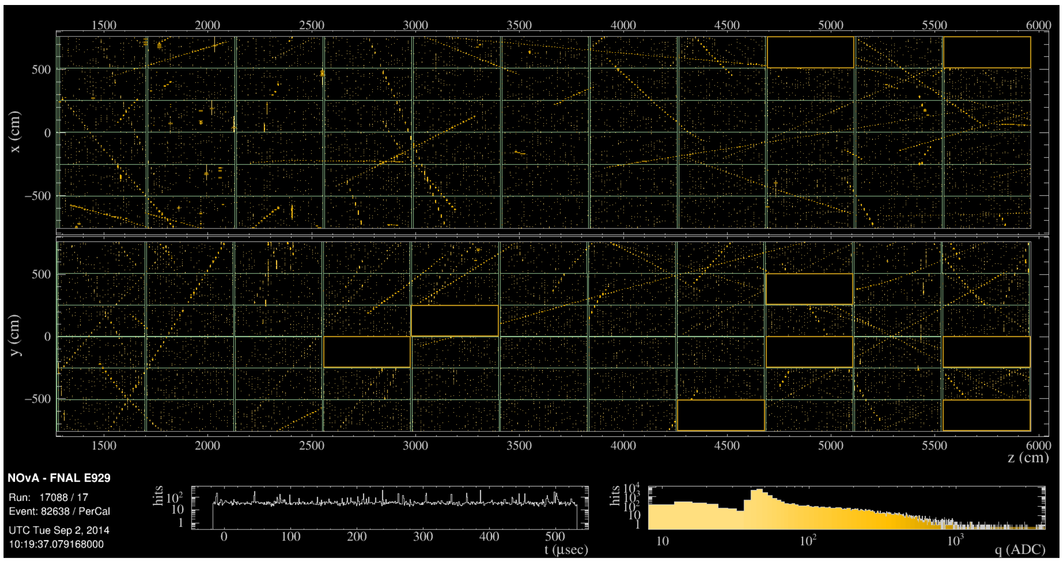

Figure 3.17: An event display of the FD shows several DCMs (outlined in yellow) that are out of sync with the rest of the detector. The result is seemingly empty DCMs. Taken from [13].

A prerequisite for the synchronization's success is that the delays of all components in the timing chain are calibrated in advance. Let assume that the delay calibration has been carried out properly. The timing system uses the scheme "At the tone the time will be . . . " to synchronize the detector. First, the MTDU examines the current time decoded from the GPS data and determines a moment sufficiently far ahead that would allow the completion of all data transmissions required for the synchronization. The value of this future moment in the format of a 56-bit NOvA timestamp is broadcasted over the

`COMMAND` line to all the components in the chain. Each component will load this value to a set of four 16-bit special registers and then enter the `PRESET_ENABLE` mode during which it awaits the arrival of a `SYNC` signal. Upon the reception, the `SYNC` will be buffered in a delay loop with the delay value pre-set during the calibration happening earlier. If properly calibrated beforehand, all the devices will exit the delay loop at the same time. The 56-bit value of the chosen "future" moment by design becomes the current timestamp and is loaded to the timer of all devices. Finally, the `PRESET_ENABLE` register is cleared, and the timing counter is allowed to advance. At this point, synchronization across all readout channels has been achieved, ensuring the smooth operation of the data-taking.

Chapter 4

Simulation of Neutron-Antineutron Oscillation

To distinguish a neutron-antineutron oscillation candidate, we need to visualize and quantify its associated characteristics. Simulating how such an event manifests itself inside the detector is the first step toward this goal. This chapter is dedicated to providing the readers with insights about the simulation process for the NOvA experiment in general, and the neutron-antineutron oscillation search in particular. More importantly, the dissection of a few simulated signal candidates at the end of this chapter is expected to lay some groundwork for the future discussion of the trigger and event selection designed for this study.

4.1 Overview of the NOvA Simulation Chain

The simulation in the NOvA experiment is a complex chain that involves several steps. These steps can be grouped into four main categories as following

1. First, there needs to be an event generator producing the primary particles whose interactions in the detector is desired. The expected result of this step is a list of final-state particles that emerge from the

interactions in consideration.

2. Second, the mentioned particle list will be ported to a Geant4 [109–111] modeling of the FD. Here, the propagation of the final states, together with their true energy depositions in the detector's active material, will be simulated.

3. Third, the energy depositions will be converted into the number of photoelectrons detected by the APDs. This conversion tackles the capture and attenuation of scintillation photons in the fiber and their absorption involving the APD's quantum efficiency.

4. Lastly, another custom simulation is developed to handle the readout of photoelectric signals. At the end of the simulation chain, datasets that resemble those collected from real experiment runs are returned.

The next section will focus on physics models employed to assist in the simulation of neutron oscillation events.

4.2 Primary Event Generator

At the beginning of the simulation chain, a generator is needed to provide the primary particles whose interactions within the detector are desired. For the case of neutrino oscillation studies, the particles of interest are neutrinos of various flavours. Their generation is handled by a suite of codes including FLUKA [112, 113], FLUGG [114], and GENIE [115].

FLUKA/FLUGG models how neutrinos are produced at NuMI via (i) the hadron production after high energy protons striking the target, (ii) the focusing of charged mesons by the horns, as well as (iii) the decays of secondary and tertiary particles into neutrinos. The end result is a set of flux files containing information about each individual neutrino's flavour, energy and momentum. These flux files are then used by GENIE to generate neutrino interactions within the detector geometry. GENIE is able to tackle all the details about the energy-dependent cross-sections, neutrino-induced hadron productions, and intranuclear transports. Finally, it composes a list of final-state particles which are ready to be used in the Geant4 detector simulation stage.

Compared to the interactions of neutrinos, the physics that needs to be simulated in the event of neutron-antineutron oscillation is not too much different. It can be summarised by the following series:

1. A spontaneous transition of a bound neutron into an antineutron set off in a target nucleus. The newly formed antineutron annihilates immediately with surrounding nucleons.

2. Following a pre-defined set of branching ratios, a mass of hadrons are produced.

3. Before escaping the nucleus as final-state particles, these hadrons possibly decay or re-interact with other nucleons in the target.

The utility needed to accurately simulate the intranuclear hadron transport (the 3^{rd} item mentioned above) has always been accessible in GENIE since its infancy [115]. The toolkit to address the two former items is developed recently [116] and made available since version 2.12.0 of the software. As it satisfies all the physics needs that were asked for, GENIE has been employed as the primary event generator for the neutron-antineutron oscillation search.

4.2.1 Modelling of Neutron Oscillation in GENIE

GENIE uses an object called the `EventRecord` to keep track of the simulation. It lists all participating particles together with the PID, energy, momentum, mass, position, parent ID, and most importantly, the state of interaction at which the particles participated. Example of an `EventRecord` is shown below in Figure 4.1. This example will be used to guide the readers through the simulation process henceforth.

First of all, GENIE requires an initial state isotope from the user's input. In this study, we limit our concern to the neutron oscillation occurring in ^{12}C. Extending the search to take into account other nuclear targets (^{14}N, ^{16}O, ^{35}Cl, etc.) present in the NOvA detectors will be a part of future work. A chosen isotope is referenced by its PDG nuclear code [117]. This code follows the numbering scheme `10LZZZAAAI` where `L`, `ZZZ` and `AAA` are the total number of s quarks, protons, and nucleons of the isotope, respectively. The single-digit `I` indicates the nuclear isomer, which assumes 0 for the ground states. In the example shown in the Figure 4.1, the target is an unexcited ^{12}C

```
|---------------------------------------------------------------------------------------------------------------|
|GENIE GHEP Event Record [print level:   3]                                                                     |
|---------------------------------------------------------------------------------------------------------------|
| Idx |          Name | Ist |        PDG |   Mother  | Daughter  |      Px |      Py |      Pz |       E |      m  |
|---------------------------------------------------------------------------------------------------------------|
|   0 |           C12 |   0 | 1000060120 |  -1 |  -1 |   1 |   3 |   0.000 |   0.000 |   0.000 |  11.175 |  11.175 |
|   1 |       neutron |   3 |       2112 |   0 |  -1 |   4 |   7 |   0.031 |   0.048 |  -0.193 |   0.936 | **0.940 | M = 0.914
|   2 |        proton |   3 |       2212 |   0 |  -1 |  -1 |  -1 |  -0.239 |  -0.154 |  -0.022 |   0.956 | **0.938 | M = 0.912
|   3 |           B10 |   2 | 1000050100 |   0 |  -1 |  15 |  15 |   0.208 |   0.106 |   0.215 |   9.330 |   9.324 |
|   4 |           pi+ |  14 |        211 |   1 |  -1 |   8 |   9 |  -0.146 |   0.108 |  -0.161 |   0.280 |   0.140 | FSI = 4
|   5 |           pi+ |  14 |        211 |   1 |  -1 |  10 |  11 |  -0.399 |  -0.130 |  -0.113 |   0.456 |   0.140 | FSI = 3
|   6 |           pi- |  14 |       -211 |   1 |  -1 |  12 |  13 |   0.270 |   0.431 |   0.250 |   0.584 |   0.140 | FSI = 3
|   7 |           pi0 |  14 |        111 |   1 |  -1 |  14 |  14 |   0.067 |  -0.516 |  -0.192 |   0.571 |   0.135 | FSI = 1
|   8 |        proton |   1 |       2212 |   4 |  -1 |  -1 |  -1 |  -0.324 |   0.294 |  -0.521 |   1.159 |   0.938 |
|   9 |        proton |   1 |       2212 |   4 |  -1 |  -1 |  -1 |   0.323 |  -0.075 |   0.302 |   1.040 |   0.938 |
|  10 |           pi+ |   1 |        211 |   5 |  -1 |  -1 |  -1 |  -0.294 |   0.073 |   0.298 |   0.447 |   0.140 |
|  11 |       neutron |   1 |       2112 |   5 |  -1 |  -1 |  -1 |  -0.032 |  -0.078 |  -0.185 |   0.961 |   0.940 |
|  12 |           pi- |   1 |       -211 |   6 |  -1 |  -1 |  -1 |  -0.066 |  -0.169 |  -0.181 |   0.292 |   0.140 |
|  13 |       neutron |   1 |       2112 |   6 |  -1 |  -1 |  -1 |   0.394 |   0.601 |   0.293 |   1.218 |   0.940 |
|  14 |           pi0 |   1 |        111 |   7 |  -1 |  -1 |  -1 |   0.067 |  -0.516 |  -0.192 |   0.571 |   0.135 |
|  15 |      HadrBlob |  15 | 2000000002 |   3 |  -1 |  -1 |  -1 |  -0.068 |  -0.129 |   0.186 |   5.533 | **0.000 | M = 5.528
|---------------------------------------------------------------------------------------------------------------|
|       Fin-Init:                                                |   0.000 |   0.000 |   0.000 |   0.047 |         |
|---------------------------------------------------------------------------------------------------------------|
| Err flag [bits:15->0] : 0000000000000000    |  1st set:                                                  none |
| Err mask [bits:15->0] : 1111111111111111    |  Is unphysical:    NO |   Accepted:   YES                     |
|---------------------------------------------------------------------------------------------------------------|
| sig(Ev) =       0.00000e+00 cm^2  | dsig(Ev;{K_s})/dK   =     0.00000e+00 cm^2/{K}   | Weight =         1.00000 |
|---------------------------------------------------------------------------------------------------------------|
```

Figure 4.1: An `EventRecord` as text output from a GENIE neutron oscillation generator. `Ist` indicates the stage of particle during the simulation. The code `Ist = 1` signifies the stable final-state particles ready for the Geant4 detector simulation. See Appendix A for the description of all `Ist` codes. The momentum $P_{x,y,z}$, the energy E and the mass m are all in the units of GeV/c.

with `PDG = 1000060120`. It was marked by a status code `Ist = 0` indicating that it is an initial state particle. Its vanished momentum means the nucleus is completely at rest.

After the target nucleus has been specified, GENIE proceeds by simulating the oscillating neutron. The position of this neutron will be randomized based on the nucleons density profile. For large nuclei ($A > 20$), the Woods-Saxon model [118] is employed but for smaller ones, such as ^{12}C, a simple Gaussian distribution model[1] is utilized. In terms of the momentum

[1]A nucleus is approximated as a sphere of radius $1.25A^{1/3}$ fm with Gaussian charge density.

and the binding energy, the Bodek-Ritchie Fermi gas model [119] provides the distributions from which the neutron's dynamical attributes are sampled.[2] This neutron is transitioned to an antineutron and then inserted to the `EventRecord` as part of the decayed state (`Ist = 3`). Due to GENIE bookkeeping, this "antineutron" appears in the `EventRecord` as a neutron, see the particle with `Idx = 1` in Figure 4.1. This caveat, nevertheless, does not affect the accuracy of the simulation.

In the next step, another nucleon will be picked to annihilate with the chosen oscillating neutron. For a ^{12}C target, this nucleon can be either a proton or a neutron with a selection probability of 6/11 or 5/11, respectively. Similar to the oscillating neutron, the sampling of dynamical properties (binding energy and Fermi momentum) for the selected nucleon are also based on the Bodek-Ritchie Fermi gas model. However, the position of this nucleon is set exactly to that of the oscillating neutron for simplicity. This second nucleon is added to the `EventRecord` as part of the decayed state (`Ist = 3`). The example in Figure 4.1 happens to feature a $\bar{n}p$ annihilation between an antineutron (`Idx = 1`) and a proton (`Idx = 2`).

The remnant nucleus is processed in the next step of the simulation. Its identity can be easily figured out by subtracting the initial isotope's Z and A to those of the nucleons participating in the annihilation process. For

[2] The `genie::NuclearModelI` interface allows GENIE to use other nuclear models via configurable user's physics options. However, the default Bodek-Ritchie Fermi gas model is used for all of the simulated data throughout this work.

the $\bar{n}p$ annihilation in the given example, the PDG code `1000060120` of a ^{12}C becomes `1000050100` which represents a ^{10}B. The remnant's momentum and energy are calculated to conserve the total energy and momentum of the system. This remnant is saved to the `EventRecord` as part of the intermediate state (`Ist = 2`). The fate of this remnant (its integrity, final energy, and momentum) is only determined after the generation of annihilation products, and subsequently, their transport out of the target nucleus are finished. At this point, this remnant became low energy nuclear fragments that enter the `EventRecord` collectively as a pseudo-particle called "hadronic blob" (`Ist = 15`).

Next, the annihilation products need to be simulated. Based on the branching ratios shown in Table 4.1, a final state is sampled using the Monte-Carlo method. Each particle in the selected final state will be assigned an energy-momentum 4-vector via the ROOT's method `TGenPhaseSpace` [120]. Here, the only constraint is the energy-momentum conservation of the two nucleons, which participated in the annihilation. These products are added to the `EventRecord` and marked as hadrons inside the nucleus with `Ist = 14`. This status code will notify GENIE to use a hadron transport package, which would be soon explained, to handle their decays or intranuclear re-interactions.

Hadrons that emerged inside a nuclear, which in this case via a neutron oscillation, might undergo the so-called final state interactions while trying to escape the remnant nucleus. These interactions, which primarily rescatters off the remnant's nucleons, will distort the distributions of the final state

	Reaction	Branching ratio	GENIE channel
	$\pi^+\pi^0$	1%	1
	$\pi^+2\pi^0$	8%	2
	$\pi^+3\pi^0$	10%	3
$\bar{n}p$	$2\pi^+\pi^-\pi^0$	22%	4
	$2\pi^+\pi^-2\pi^0$	36%	5
	$2\pi^+\pi^-2\omega^0$	16%	6
	$3\pi^+2\pi^-\pi^0$	7%	7
	$\pi^+\pi^-$	2%	8
	$2\pi^0$	1.5%	9
	$\pi^+\pi^-\pi^0$	6.5%	10
	$\pi^+\pi^-2\pi^0$	11%	11
$\bar{n}n$	$\pi^+\pi^-3\pi^0$	28%	12
	$2\pi^+2\pi^-$	7%	13
	$2\pi^+2\pi^-\pi^0$	24%	14
	$\pi^+\pi^-\omega^0$	10%	15
	$2\pi^+2\pi^-2\pi^0$	10%	16

Table 4.1: The antineutron annihilation branching ratios (BRs) used in the GENIE event generator, taken from the search for $n-\bar{n}$ oscillation by Super-Kamiokande [2]. The BRs for $\bar{n}p$ and $\bar{n}n$ are independent from each other.

observables. The larger the nuclei are, the more significant the effects of the FSI becomes [115]. Despite the fact that the ^{12}C nucleus has a relatively small size (only 2.7 fm), the FSI of the annihilation products still has a non-negligible impact on the topology as well as the visible energy of a $n-\bar{n}$ event. Thus, correctly simulating this process is desired for the accuracy of the simulation as a whole. GENIE utilizes a package called `INTRANUKE`[3] to carry out the intranuclear hadron transport. In the estimation of the re-interaction

[3]The first version of this package was developed to simulate the intranuclear rescattering of pions in the Soudan 2 experiment [121].

probability, the mean free path of a hadron product with energy E and at a radius r is defined simply as [115]

$$\lambda(E, r) = \frac{1}{\sigma_{\mathrm{tot}}^{\mathrm{hN}}(E) \times \rho(r)}, \tag{4.1}$$

where $\sigma_{\mathrm{tot}}^{\mathrm{hN}}$ is the total hadron-nucleon cross-section and $\rho(r)$ is the nuclear density profile. The cross-section model is tuned to data from bubble chamber experiments from the 70s and 80s which used hydrogen and deuterium as targets; see "Hadron-Nucleon Total Cross-Sections and Related Quantities" listing in [122] for more details about the dataset. As an example, a $0.5\,\mathrm{GeV}/c$ $\pi^{\pm}$ with a σ_{tot} around $50\,\mathrm{mb}$ (or $5\,\mathrm{fm}^{-2}$) [122] travelling inside a $^{12}\mathrm{C}$ with a fairly constant nucleon density of about $0.1\,\mathrm{fm}^{-3}$ [123], has an estimated mean free path of $2\,\mathrm{fm}$. On average, such $\pi^{\pm}$ would undergo at least one re-interaction before leaving the nucleus. With the mean free path available, the hadrons are then propagated through the nucleus until they either re-interact or leave the nucleus. If they re-interact, `INTRANUKE` uses a Monte-Carlo to immediately replace them by a prescribed final state without simulating and propagating the products in the subsequent interactions through the nucleus. The particles that leave the nucleus will enter the `EventRecord` as stable final-state particles, `Ist = 1`. After this point, those particles are ready for the rest of the NOvA simulation chain.

As the FD is on the surface and exposed to a high rate of cosmic particles, there is an addition generator called CRY [124] needed to simulate this effect in the detector. Like GENIE, CRY results in a list containing detailed information about the PID, the energy and momentum of all cosmic particles passing through the detector geometry. There also exists a utility [15] to embed one or a few of neutron oscillation events to a time window of 550 μs full of cosmic tracks and showers, see Figure 4.5. The main use for this type of simulation samples is to evaluate the trigger efficiency. This issue will be further discussed in Chapter 5.

4.3 The Detector Simulation in NOvA

4.3.1 Geant4 Modelling of the Detector

The simulation continues by taking all the final-state particles generated by GENIE (and CRY) and inputting them through an intricate Geant4 model of the FD. Geant4 simulates the trajectories and the energy depositions of those particles in the active material. This stage results in a list of "Fiber in Liquid Scintillator Hits" (or `FLSHits`), which represents the true energy deposition in the detector.

4.3.2 Optical Simulation of the Detector

This optical simulation aims to model the transport of scintillation photons from the points they spawn to the APD pixels where they end up being detected. A custom package called `PhotonTransport` has been developed to handle this simulation. The essence of this modeling was briefly outlined below.

First, the Birks-Chou's law converts the true energy deposition into the expected number of scintillation photons:

$$\frac{\mathrm{d}\mu_\gamma}{\mathrm{d}x} = S \times \frac{\frac{\mathrm{d}E}{\mathrm{d}x}}{1 + k_B\frac{\mathrm{d}E}{\mathrm{d}x} + k_C\left(\frac{\mathrm{d}E}{\mathrm{d}x}\right)^2}. \tag{4.2}$$

In this equation, $S = 3159.07\,\mathrm{MeV}^{-1}$, $k_B = 0.0125\,\mathrm{g/cm^2/MeV}$ and $k_C = 0\,\mathrm{cm^2/MeV^2}$ are the scintillation efficiency, the Birks' and Chou's constants, respectively [125].

Second, the expected number of collected photons $\mu_\gamma^{\mathrm{coll.}}$ that are able to enter the fiber and eventually reach the APD pixel is determined.

$$\mu_\gamma^{\mathrm{coll.}} = \frac{1}{2}N_\gamma \times (\Gamma_1 + \Gamma_2). \tag{4.3}$$

The transmission coefficients Γ take into account the light collection efficiency and attenuation of the WLS fibers. After entering a fiber, the photons are split equally to two groups with each traveling to the opposite ends of the fiber. Each of these groups will experience a distinct attenuation due to the difference in the length of travel. This explains the factor of 1/2 and the two values of the transmission coefficients $\Gamma_{1,2}$. The attenuation as a function of distance is measured directly in the fiber quality control tests. The estimation of the light collection efficiency as a function of the position along the cell, however, requires a dedicated ray tracing simulation subpackage called `PhotonSim` [126].

Lastly, the true number of photons $N_\gamma^{\mathrm{coll.}}$ captured by an APD pixel with a quantum efficiency ϵ and a noise factor F is obtained by a Poisson sampling with $\mu_\gamma^{\mathrm{coll.}} \times \epsilon \times F$ as the mean.

4.3.3 Readout Simulation

The final procedure is simulating the electronic signal response of the detector. As described in the previous chapter, the logic circuits inside a FEB will perform a series of operations including an analog amplification, a pulse shape conditioning followed by a pedestal subtraction onto the signal that the FEB received from an APD. A custom simulation package was developed to mimic all of these processes while incorporating electronic noise [126].

4.4 Characteristics of Signal Events

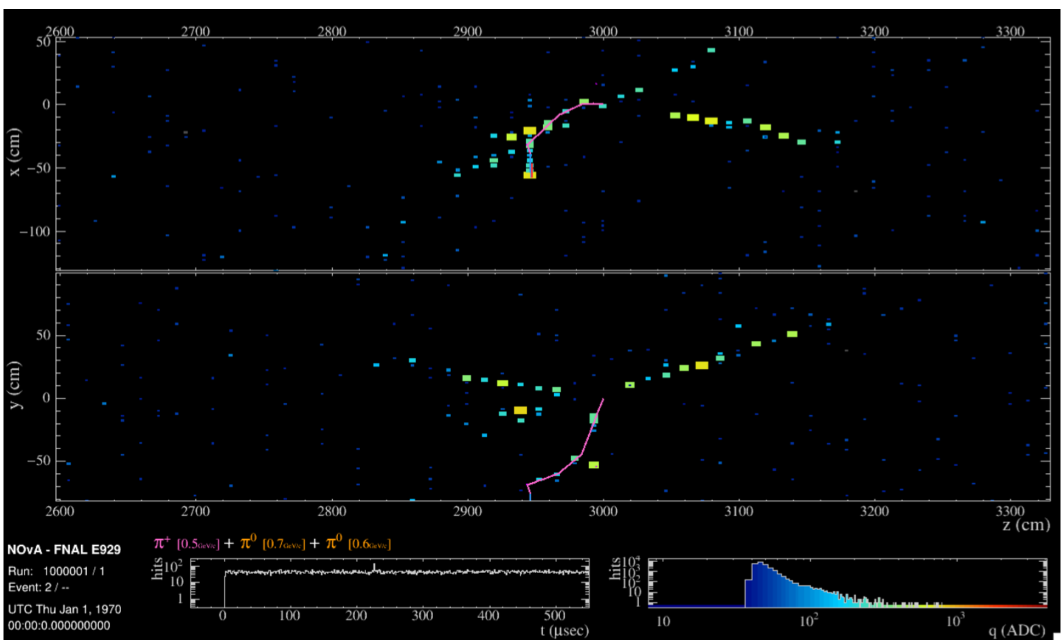

Figure 4.2: Display of a $p + \bar{n} \rightarrow \pi^+ + 2\pi^0$ simulated event.

The displays of selected simulation events from all 16 $\bar{n}$-nucleon annihilation channels can be found in Appendix A. The example of a

$p+\bar{n} \to \pi^+ + 2\pi^0$ is shown below in Figure 4.2 for quick reference. A glimpse of this display can provide some signatures of neutron oscillation events. These signal events are characterized by a high multiplicity of hadrons, which are mostly pions. These hadrons form a pattern of tracks and showers that center around the interaction vertex and extend a few hundred centimeters on average. Figure 4.3 shows clearly the spherical nature in the topology of these signal events.

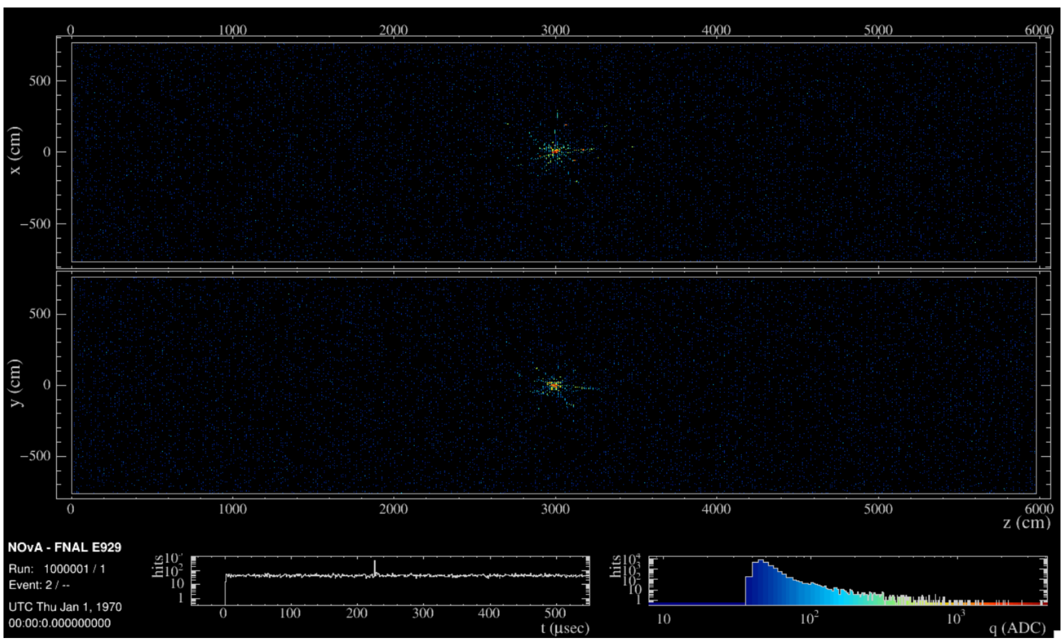

Figure 4.3: An event display of 10 signal candidates with their vertices right at the center of the FD, overlaying on top of each other. The hits are distributed spherically around the common vertex point.

In terms of energy characteristics, the annihilation between an antineutron and a nucleon is expected to produce total energy of a bit less than 2 GeV. However, due to the final state interactions, which might result in the formation of components like neutrons, gammas, or very low energy hadronic fragments, only more than half of the energy is visible [127], see Figure 4.4.

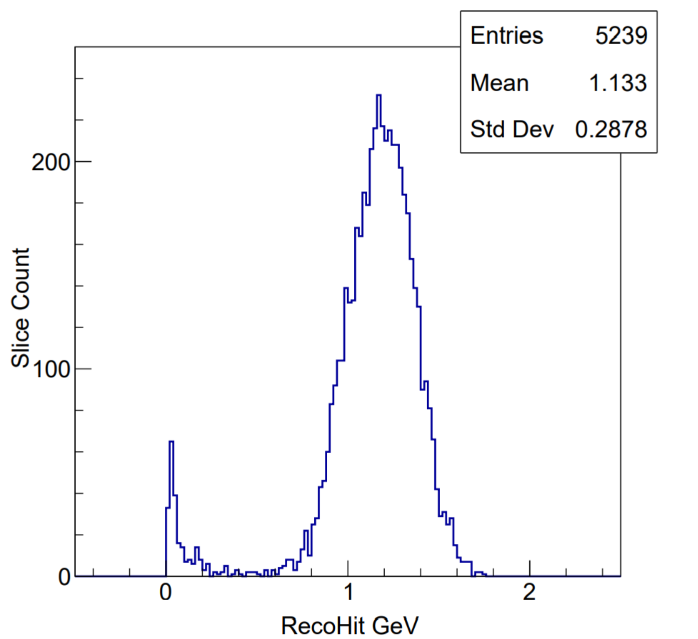

Figure 4.4: Reconstructed energy of simulated neutron oscillation events. The smaller peak near zero is due to failure of slicing algorithms where a single interaction is reconstructed as multiple ones.

By now, we might already have a notion of how to recognize signal events for the search. More intricate characteristics regarding the energy distribution, the timing, and the symmetric topology of an event will be considered in the following chapters.

A sample of 1.6M simulated signal events (100k events per annihilation channel) has been produced to assist the development of the trigger and the event selection. In order to evaluate the trigger efficiency, a sample of 10,100 signal events overlaid onto CRY cosmic particles is also produced, see Figure 4.5.

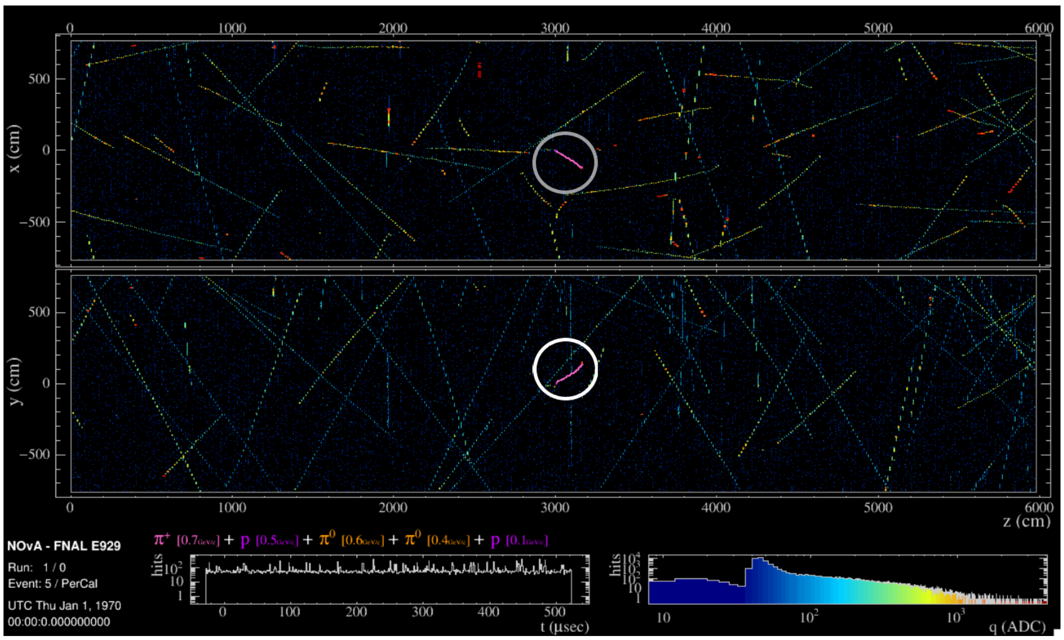

Figure 4.5: An neutron oscillation interaction, marked by the while circles, is overlaid onto a CRY simulation of cosmic ray particles. Taken from [15].

Chapter 5

The Neutron Oscillation Trigger in NOvA

As discussed in Chapter 3, the DAQ system in the NOvA experiment works in a continuous mode. Signals from all the front-ends will be readout, synchronized, and transferred to the buffer nodes continuously, without the need of any real-time triggers. For the FD, which is composed of more than 344,064 readout channels, the throughput of the raw data is quite enormous, about 1 GB/s. This rate greatly exceeds the storage capacity of any data centers at Fermilab. Furthermore, due to the lack of real-time physics triggers, only a fraction of these data contains the events that are meaningful for physics analyses. In order to retain the interesting physics interactions, and at the same time, maintain a sustainable data transfer, NOvA comes up with the design of a high latency trigger system which processes the buffered data and grants the permanent storage privilege only to those containing desired physics information. This trigger is required to be fast, have high efficiency, and be able to cope with a background rate of roughly 120 kHz as a result of the constant cosmic muon bombardments. This chapter will elucidate the working principle of this system by analyzing the concrete example of the neutron anti-neutron oscillation trigger.

5.1 Trigger System in NOvA

In NOvA, the operation of the trigger system is strongly coupled to that of the DAQ, which has been covered in Chapter 3. As a quick reminder to the readers, the FEBs readout the APD's digitized hits every $50\,\mu$s and feed them to the DCMs. At the DCM's FPGA, these hits will be joined together to form a microslice [107], a structure containing the data from all 64 FEBs during the $50\,\mu$s time window. Another DCM application will further concatenate those microslices into a longer chunk of 5 ms, or the millislices [107]. A millislice of 8-9 kBytes in size is the perfect payload for the jumbo-frame transport protocol which connects the DCMs and the buffer nodes.

The routing of these millislices from the DCMs to the nodes in the computing farm is performed in the round-robin fashion: each successive set of 5 ms millislices from all the DCMs is sent to the a buffer node queing in a round robin chain, see Figure 5.1. A 5 ms snapshot of the whole detector, or a milliblock [107], will be created and buffered in that node for a minimum of 20 s. The cap of buffering time is, however, varying on each node and depends how fast the data is processed then cleared from the buffer. With about 200 active nodes, the total buffer capacity can reach 30 minutes under normal operating conditions. This enables the high latency trigger system to trace back upto half an hour in time and search for the data containing interesting physics, long after the event had happened. Data with no desired physics will be discarded eventually.

Trigger decisions are made by the Global Trigger (GT). This decision

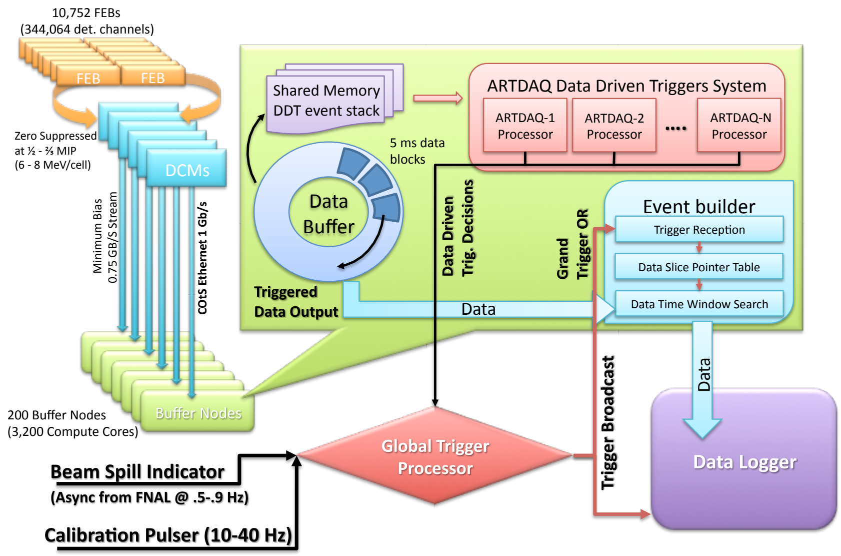

Figure 5.1: A schematic overview of the FD DAQ system [16].

provides the buffer nodes with three pieces of information to specify the time window for the buffered data to be extracted and the physics category of the event in consideration: (i) the start time t_0, (i) the duration Δt (just $50\,\mu$s for the case of the neutron oscillation trigger), and (iii) the trigger bit. This system allows maximal flexibility as it is capable of issuing a variety of triggers ranging from a short neutrino beam spill ($\Delta t \sim 100\,\mu$s) to a long supernova exposure ($\Delta t \sim 100\,$s). The GT is driven by one of the following: the NuMI indicator, the cosmic pulser and the data-driven triggers (DDTs). The NuMI indicator issues a fixed time shortly after a spill has occurred at Fermilab. This signal allows NOvA to record the accelerator neutrino events, which form the primary dataset for neutrino oscillation studies. The cosmic pulser fires at a set frequency of 10 Hz to help collecting samples of cosmic ray interactions which are crucial for calibration and data quality monitoring purposes. The data-driven triggers are issued by a special application running on each buffer node. It composes of various selection algorithms that run simultaneously on separate threads. Each algorithm examines the buffered data, which live on a shared memory and is accessible to all threads, to hunt the events that possess specific signatures. If a DDT determines that an event with desired characteristics has been found, a notification will be sent back to the GT. Furthermore, the GT is able to use a consensus of such notifications across multiple buffer nodes to broadcast a trigger to the whole farm. This ability enables the trigger of long events with a duration extending much beyond the 5 ms window of a milliblock, such as supernova neutrino bursts which typical last upto 10 seconds.

Lastly, we will briefly mention how the data is permanently stored for further offline analysis. This is achieved by the Data Logger. This system includes a unique commodity server which receives trigger-selected data from the buffer nodes and convert it into a format convenient for permanent storage or further usage, see Figure 5.1. A global trigger issued to the buffer nodes will also be replicated to the Data Logger for verification. Once validated, the data formatted by the Data Logger are then written to a local disk, waiting to be transferred to the Fermilab mass storage via a separate file transfer system. The sizes of the data including only the minimal bias sample (from cosmic pulser trigger) and the NuMI spill data (from NuMI indicator) are about

25 TB/yr for the FD and about 1 TB/yr for the Near Detector. To serve the online data monitoring purposes, the Data Logger also logs the data to a memory segment shared to external applications such as the online monitoring and the online event display [128].

5.2 Neutron Oscillation Data-Driven Trigger

In this section, the development of the data driven trigger (DDT) dedicated to gather the relevant data for the neutron oscillation search (`NNbarDDT`) in the NOvA experiment will be discussed.

Even though NOvA, as mentioned in previous chapters, introduces a lots of advantages to the search of neutron anti-neutron oscillation, its location brings about a major caveat. The NOvA FD is on surface, thus it is exposed to a high cosmic rate of 120 kHz. To be able to select the signal events, we need an algorithm that can filter out the interactions from the frequently present cosmic rays and identify only those that have the topological characteristics of an antineutron annihilation. An additional constraint is the tight trigger rate limit of 5 Hz assigned to the search. Exceeding this limit would negatively affect the performance of the trigger and data logger systems. As such, the challenges to the development of this DDT algorithm is to achieve a high efficiency in selecting the signal candidates while reducing the background cosmic rate from 120 kHz down to approximately 5 Hz.

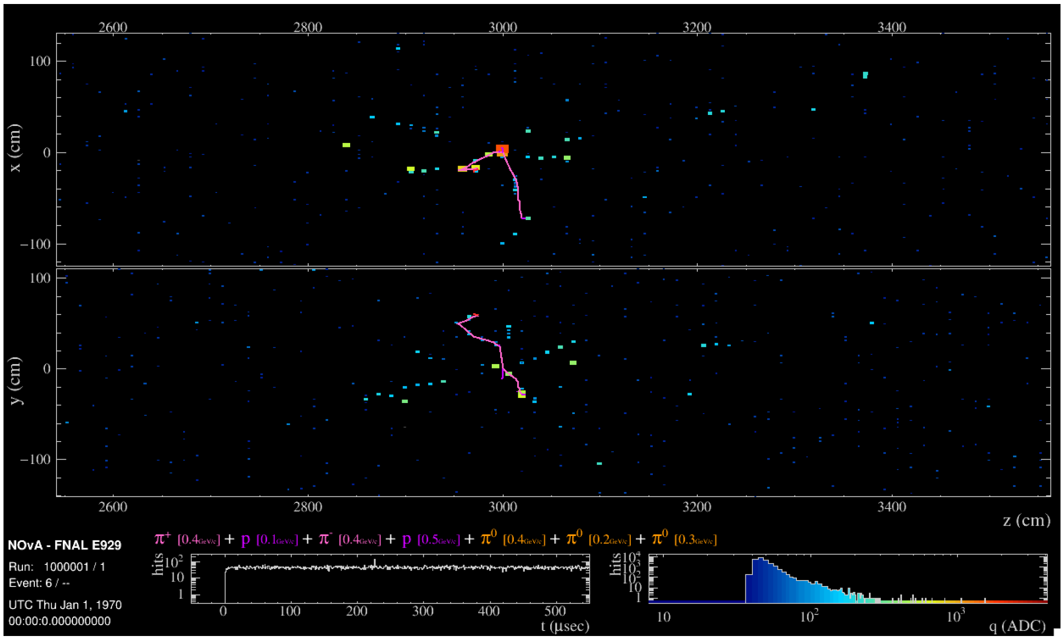

Figure 5.2: Example of an simulated event of $\bar{n} + p \rightarrow 2\pi^{+} + \pi^{-} + 2\omega^{0}$ in the FD.

To assist the development of the selection algorithm, a signal sample consists of 10,100 simulated signal events with their vertex positions uniformly randomized throughout the FD has been used. The details of this signal simulation has been covered in Chapter 4. For the background, we directly use a cosmic ray sample collected during an exposure time of 2.8 s at the FD which contains in total 328,274 interactions. The signature of a neutron anti-neutron oscillation event is the annihilation of the newly formed antineutron in the target nucleus. This would be observed as an isolated, shower-like cluster of hits in the detector with total energy depositions ranging from 1.5 to 2 GeV, see Figure 5.2. A more complete list of event displays from all other annihilation channels can be found in the Appendix A. Basically, the `NNbarDDT` algorithm would identify the hit clusters whose topology resembles a star-like shower with 4-5 prongs emerging from a common vertex at the center. The cuts that relate to the energy deposition is not included since we realized that without the kinematic constraint the `NNbarDDT` can collect various categories of interactions owning similar topological traits, which allows studies other than the $n-\bar{n}$ oscillation. As a result, only five cuts that focus on the topology of the events are chosen in the final algorithm. Their performance is summarized in the Table 5.1 and Table 5.2 below. The details of those selection criteria will be discussed in the following sections.

Selection cuts	Slice count	Fraction	Trigger rate (Hz)
Pre-containment	328274	1.0	118637
Containment	8762	2.7×10^{-2}	3167
Width-length ratio	59	1.8×10^{-4}	21
Cell number multiplicity	26	7.9×10^{-5}	9
Hit count asymmetry	20	6.1×10^{-5}	7
Hit extent asymmetry	15	4.6×10^{-5}	5

Table 5.1: Trigger rate reductions with topology based cuts only.

5.2.1 The Problem of FEB flashers

One well known problem of the NOvA DAQ system is the so-called FEB flashers. This manifests as a local group of channels from a single FEB producing signals way above the DCS threshold during an extended duration

Selection cuts	Slice count	Signal efficiency (%)
Pre-containment	10100	100
Containment	6845	68
Width-length ratio	6139	61
Cell number multiplicity	5991	59
Hit count asymmetry	5976	59
Hit extent asymmetry	5786	57

Table 5.2: Signal efficiency with topology based cuts only.

of time, upto 30 μs, see Figure 5.3. This phenomenon usually occurs a few μs after a high energy particle passing through the detector and leaving a large amount of charge in a single pixel on a FEB. In spite of having a highly recognizable topology to a human, a FEB flasher can effectively trick the `NNbarDDT` algorithm into classifying it as a signal event. In the earlier versions of this DDT, the FEB flashers can be filtered out easily with energy-based cuts. But once we decided to exclude those cuts from the selection criteria, we need to rely on a pre-existing package to remove the FEB flashers.

The FEB flasher filter receives a list of raw hits sorted in FEB number and time as an input. When looping through this list, the filter will check for saturated hits (ADC value exceeds 3400) and log their corresponding FEB numbers and timing into a map. The filter then runs through the map of found saturated hits and checks all the hits within the same FEB to see if they form the so-called flasher hits. A flasher hit is from the same FEB, lying within 20 ns with a saturated hit and having an ADC

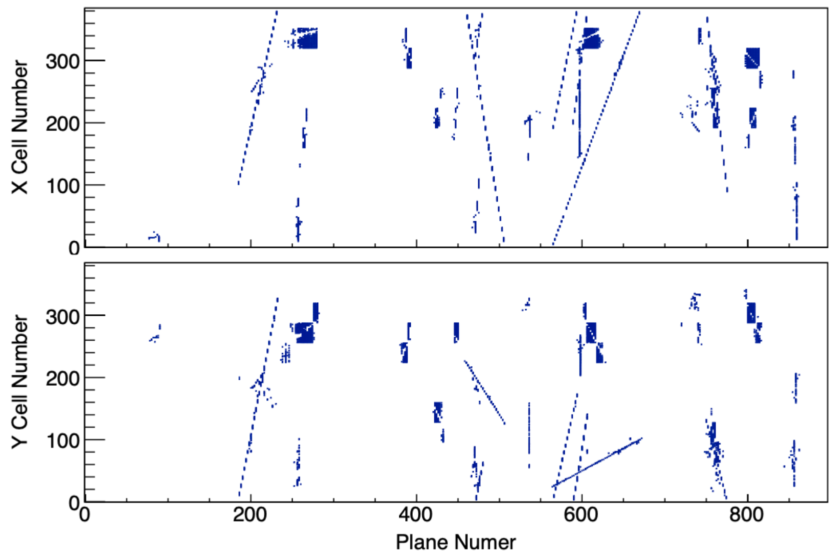

Figure 5.3: FEB flashers appear after removing energy based cuts.

value less than 500. Once a group of hits is identified as a flasher, it will be ignored from all of the selection criteria.

5.2.2 Containment Cuts

The first criterion to be applied is the containment cut. Only the interactions that are fully contained in the volume specified by the following conditions will proceed with further cuts:

$$\begin{cases} z & \in & [3, 891] \\ x & \in & [4, 377] \\ y & \in & [6, 347], \end{cases} \tag{5.1}$$

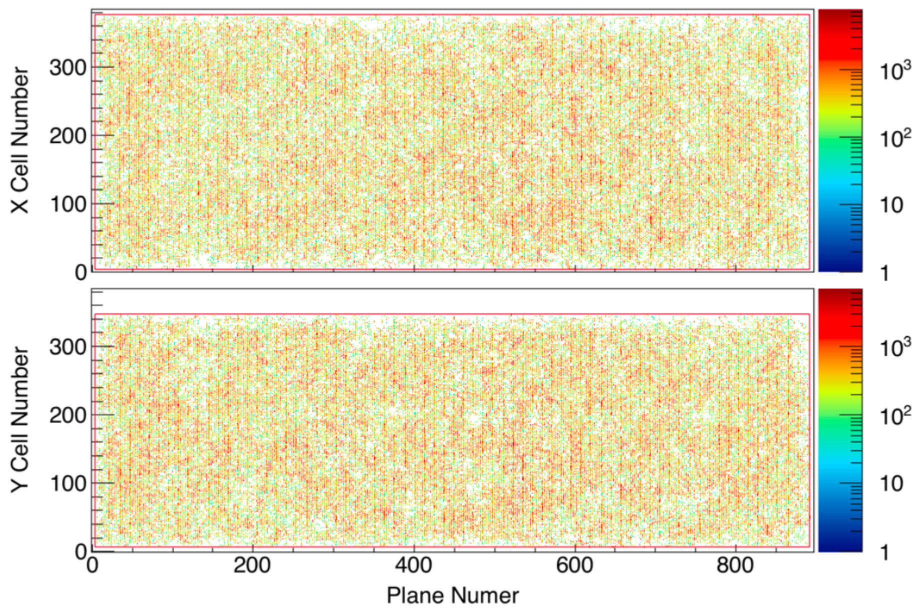

Figure 5.4: Hits weighted by ADC after containment cuts applied to the signal sample. The red lines indicate the boundary of the containment volume.

in which x, y, z represent the cell number in the $X - Z$ view, $Y - Z$ view and the plane number of a hit, respectively, see Figure 5.4. Since most of the cosmic rays enter the FD from above, the strong cut on y reduces the trigger rate significantly. However, the signal efficiency is also scaled down as the containment volume gets smaller. The set of cuts in (5.1) is found to be an optimal one, maximizing the trigger rate reduction while maintain a high overall signal efficiency.

5.2.3 Width-to-Length Ratio

A topological variable that proves effectiveness in separating the signal from the cosmic background is defined as the ratio of width to the length of a slice, one for each view. To be precise, a slice will be reconstructed by a Hough tracker. Consider one detector view, the longest among the tracks that compose the slice defines the length L, while the largest distance from an individual hit to the longest track defines the width W of the slice.

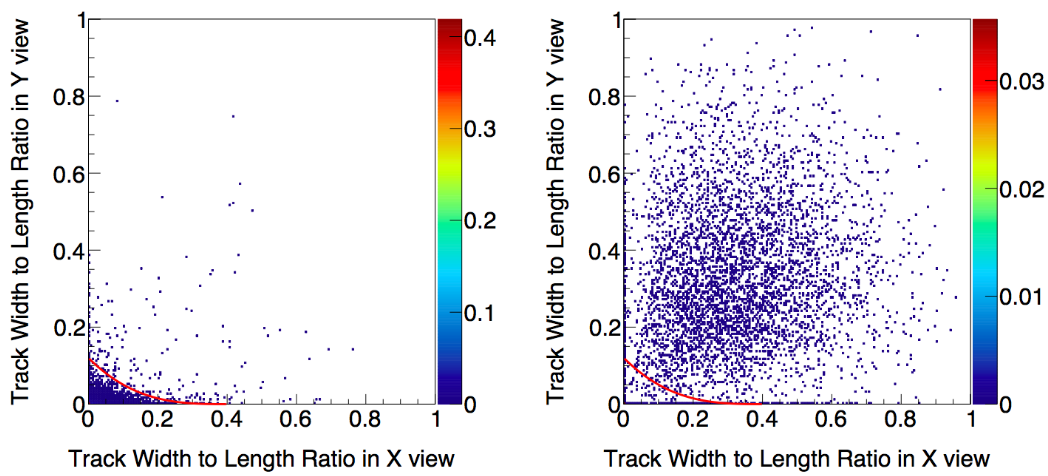

(a) cosmic (b) signal

Figure 5.5: Track width-to-length ratio. Slices in the region below the red curve, which is indicated by the inequality in (5.2), are cut off (99% cosmic rays and 10% signal).

As one might expect, a cosmic ray track is usually thinner than an antineutron annihilation shower, see Figure 5.5. From the distribution of the signal and cosmic background, we decide the cut region to be

$$R_y \leq -3.125\,(R_x - 0.4)^3\,, \tag{5.2}$$

in which, $R_x = W_x/L_x$ and $R_y = W_y/L_y$ are the width-to-length ratio for the slices in $X-Z$ and $Y-Z$ views, respectively.

5.2.4 Cell Number Multiplicity

Another topological characteristics that distinguish a signal candidate from a cosmic ray is the cell number multiplicity. Cell number of a hit represent its transverse position in the detector. A track-like slice (except for a horizontal one) like the one resulted from a cosmic ray, will have a low cell number multiplicity. In other words, each of the detector transverse positions will likely be occupied by only one of its hits, see Figure 5.6a. On the other hand, a star-like shower from a signal candidate will have a tendency of getting high cell number multiplicity, see Figure 5.6b. In a way, this variable resembles the particle multiplicity in the final state of an interaction.

To precisely quantify this topological trait, the cell number multiplicity is defined as

$$M = \frac{N_{\text{multiple}}}{N_{\text{distinct}}}, \tag{5.3}$$

in which, N_{multiple} is the count of cell numbers with multiple hits and N_{distinct} is the count of distinct cell numbers (the number of cell numbers with at

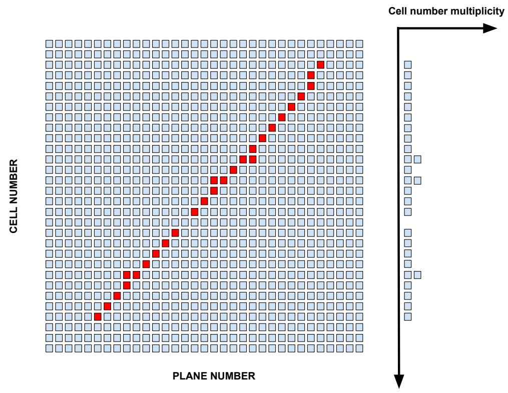

(a) Background

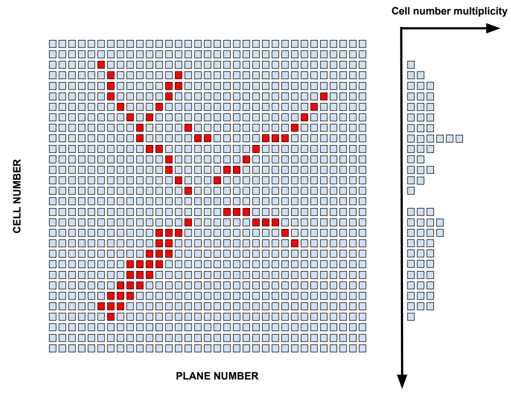

(b) Signal

Figure 5.6: A cartoon of event displays for a signal event and a background cosmic event to demonstrate the concept of cell number multiplicity.

least one hit). This number M will be calculated for each of the views. For example, the Figure 5.6a, N_{multiple} is 3 and N_{distinct} is 24, while in Figure 5.6b, N_{multiple} is 21 and N_{distinct} is 24. Thus, the cell multiplicity M for the background slice is 0.125 and that for the signal slice is 0.875.

Figure 5.7 shows the distribution of the cell number multiplicity calculated for the simulated signal and the cosmic background samples. A clear difference in converging tendencies for the two samples in the (M_x, M_y) space provides us with a highly effective cut. The cut regions are chosen as

$$M_y \leq 0.1 \exp\left(-\frac{M_x}{0.05}\right) + 0.02, \tag{5.4}$$

with M_x and M_y are the cell number multiplicity in the $X - Z$ and $Y - Z$ views, respectively.

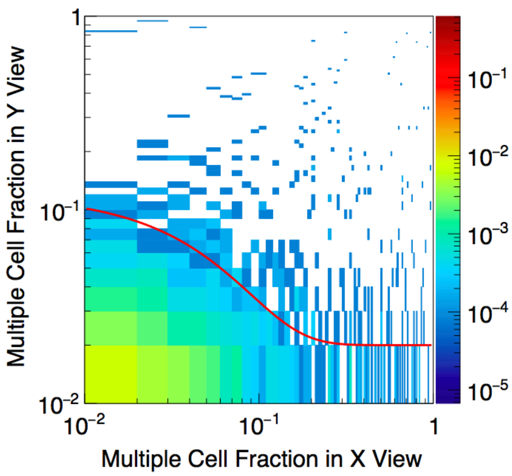

(a) cosmic

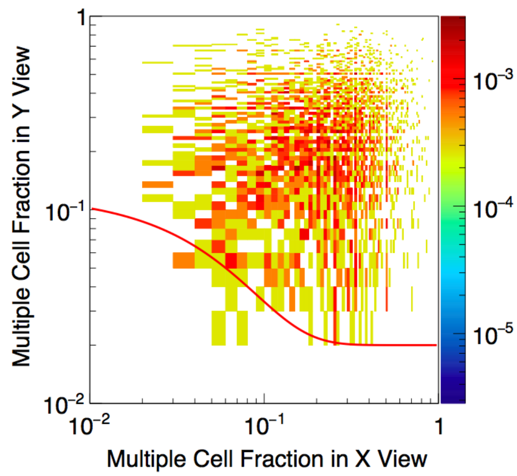

(b) signal

Figure 5.7: The distribution of the cell number multiplicity for the signal and background samples. Slices in the region below the red curve, which is indicated by the inequality (5.4), are cut off (97% of cosmic rays and 4% of signal candidates).

5.2.5 Hit Count Asymmetry

Due to the fact that the cosmic rays bombarding the FD from the top and with a preference of vertical direction, there exists an asymmetry in the way hits from cosmic ray interactions are distributed between the two views of the detector. On the other hand, an annihilation event does not have an angular preference for its energy depositions. The hit count asymmetry marks a way to exploit this intrinsic difference between two types of events. We will define this asymmetry as

$$a = \frac{N_x - N_y}{N_x + N_y}, \tag{5.5}$$

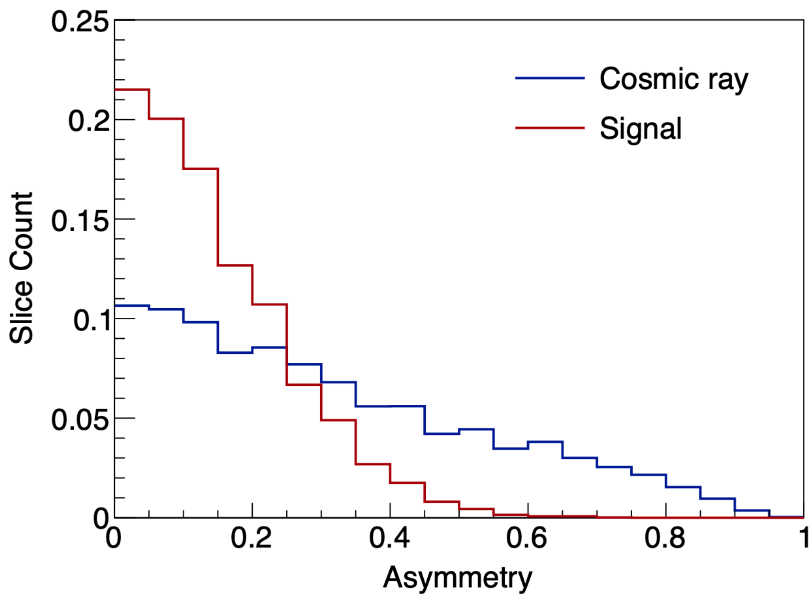

Figure 5.8: Distribution of the hit count asymmetry. Slices with $a > 0.5$ are cut off (21% of cosmic rays and 0.6% of signal candidate).

where N_x and N_y are the counts of hits in $X - Z$ and $Y - Z$ views of the detector, respectively. a will be a value between 0 and 1, with $a \to 0$ signifies a quite symmetrical event geometry.

The distribution of this variable calculated for the signal and background samples is shown in Figure 5.8. Slices with high hit count asymmetry, marked by $a >= 0.5$, are cut off.

5.2.6 Hit Extent Asymmetry

Similar to the hit count asymmetry, we can defines the plane and cell extent asymmetries.

$$a_Z = \frac{Z_{\text{max}} - Z_{\text{min}}}{Z_{\text{max}} + Z_{\text{min}}}, \tag{5.6}$$

$$a_C = \max_V \left(\frac{C_{\text{max}} - C_{\text{min}}}{C_{\text{max}} + C_{\text{min}}} \right). \tag{5.7}$$

In the first equation, a_Z is the plane extent asymmetry, $Z_{\text{max/min}}$ are the maximum and minimum plane number of hits, regarding both views. In the second equation, a_C is the cell extent asymmetry, $C_{\text{max/min}}$ are the maximum and minimum cell number of hits in each view. $\max(\ldots)$ mean taking the larger value after a_C for each of the two views is calculated. Again, we observe a difference in distribution of signal and background samples in the (a_C, a_Z) space, see Figure 5.9. The signal region is then defined by

$$a_Z \leq -0.6\ a_C + 0.6. \tag{5.8}$$

This selection criterion primarily removes the cosmic ray interactions which extends the whole length of the detector ($a_Z = 1$) or over many planes.

5.2.7 DDT Selected Events

As mentioned in the introduction, the combination of those five selection cuts has been successful in reducing the trigger rate from 12 kHz to

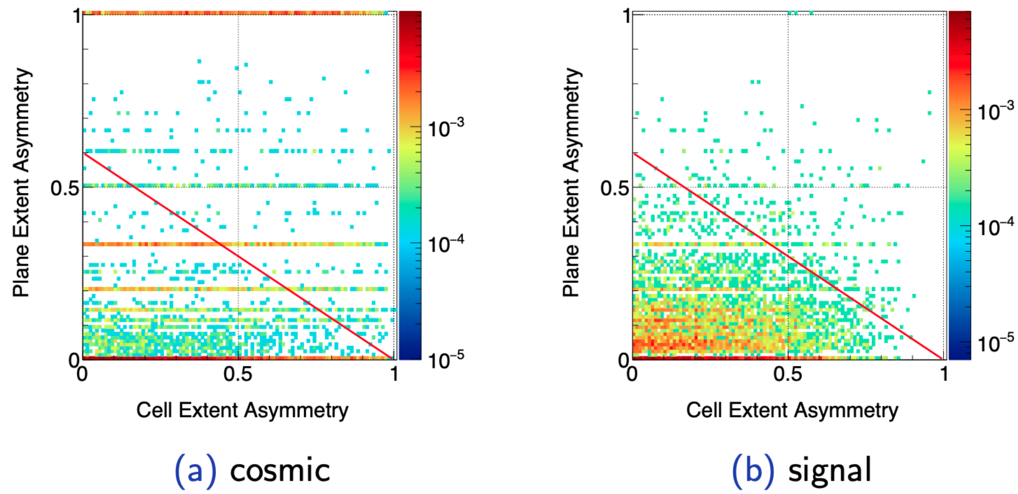

Figure 5.9: Distribution of the plane and cell extent asymmetries. Events above the red curve are cut off (28% of cosmic rays and 5% of signal candidates).

5 Hz while retaining a relatively high signal efficiency of 57%. As a reminder, we used a sample of 328274 cosmic ray interactions, with an exposure of 2.8 s, for the background. Fifteen of those interactions survive all the cuts and created a trigger decision, leading to the quoted 5 Hz trigger rate. The event displays of those interactions are shown in Figure 5.10 below.

The geometry of the survived interactions resembles more or less the wanted antineutron annihilations. This has proved the success in developing a DDT algorithm to search for the neutron anti-neutron oscillation.

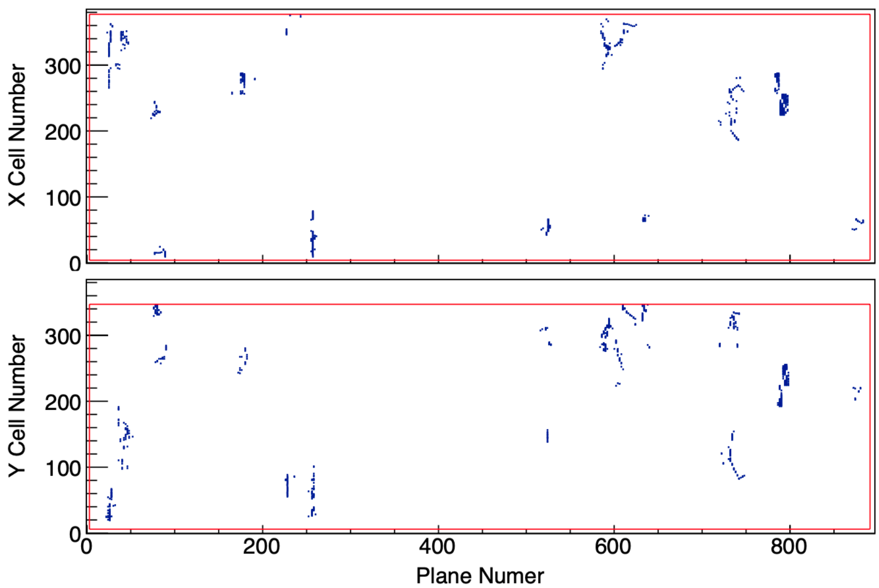

Figure 5.10: Hits of the remaining 15 cosmic slices after all the cuts. Red lines indicates the boundary of the containment volume.

5.3 Deployment and Monitoring

The DDT algorithm has been tested for the NOvA's FD during the 2018 Fermilab's summer shutdown. Once deployed, the selection algorithm produced a trigger rate of more than 8 Hz, higher than its designed value. However, since the global trigger and data logger did not experience any throttling, the `NNbarDDT` algorithm was accepted to deploy without further modifications. When validating the new data stream, we also learned that the algorithm has collected a large sample of cosmogenic neutrons and high energy cosmic showers, which might become valuable to other studies in NOvA. The DDT has been stable and constantly taking data since September 6th, 2018. As of August 5th, 2019, the total exposure of the

`NNbarDDT` is 693.3 days. The trigger rate is stable at about 8.1 Hz, amount to 7×10^5 triggered events per day with daily raw data throughput exceeds 50 GB.

Chapter 6

Background Modelling

The primary sources of background for the neutron oscillation search in NOvA are the cosmogenic particles (neutrons and gammas) and the atmospheric neutrinos. Being on the surface, the NOvA Far Detector is continuously bombarded by cosmic muons at a rate of about 120 kHz. A significant amount of these muons can interact with the overburden above the detector, generating fast neutrons that can travel to the interior and mimic anti-neutron annihilation showers. These cosmogenic neutrons are the dominant background of the search. Another smaller component is atmospheric neutrinos. With the energy requirement for the event selection, atmospheric neutrinos amount to only a hundred events a year. Simulation samples of fast neutrons and atmospheric neutrinos are produced to develop the background rejection criteria and estimating the background for the analysis. The details of the simulation and the background rejection will be discussed in this chapter.

6.1 Atmospheric Neutrinos Background

High energy primary cosmic rays (typically protons) constantly strike the atomic nuclei in the Earth's atmosphere. This results in cascades of secondary particles composed mostly of $\pi^{\pm}$ and $K^{\pm}$. These unstable mesons decay as they travel towards Earth's surface and produce a sea of atmospheric neutrinos. Most of these neutrinos pass through the detector without leaving any traces. With a slim chance, however, a neutrino can collide with a nucleus via a neutral (NC) or charge current (CC) interaction, leaving a shower of hadronic particles that look isolated from any other activity in the detector. If the neutrinos has an energy of 1-2 GeV, the hadronic shower produced in its interaction can resemble an antineutron annihilation, see Figure 6.1. Thus, atmospheric neutrinos constitute an irreducible component of the background in the search for neutron-antineutron oscillation. Being able to simulate the atmospheric neutrinos in order to understand their interactions in the detector as well as to estimate their contribution to the background of the search is an important objective of this analysis.

The first ingredient for the simulation of the atmospheric neutrino background is the flux. So far, there are two common flux models available: (i) the BGLRS[1] model [129], and (ii) the HKKMS[2] model [130]. This work

[1]Abbreviation of authors' names: Barr G. D., Gaisser T. K., Lipari P., Robbins S., and Stanev T.

[2]Abbreviation of authors' names: Honda M., Kajita T., Kasahara K., Midorikawa S., and Sajjad Athar M.

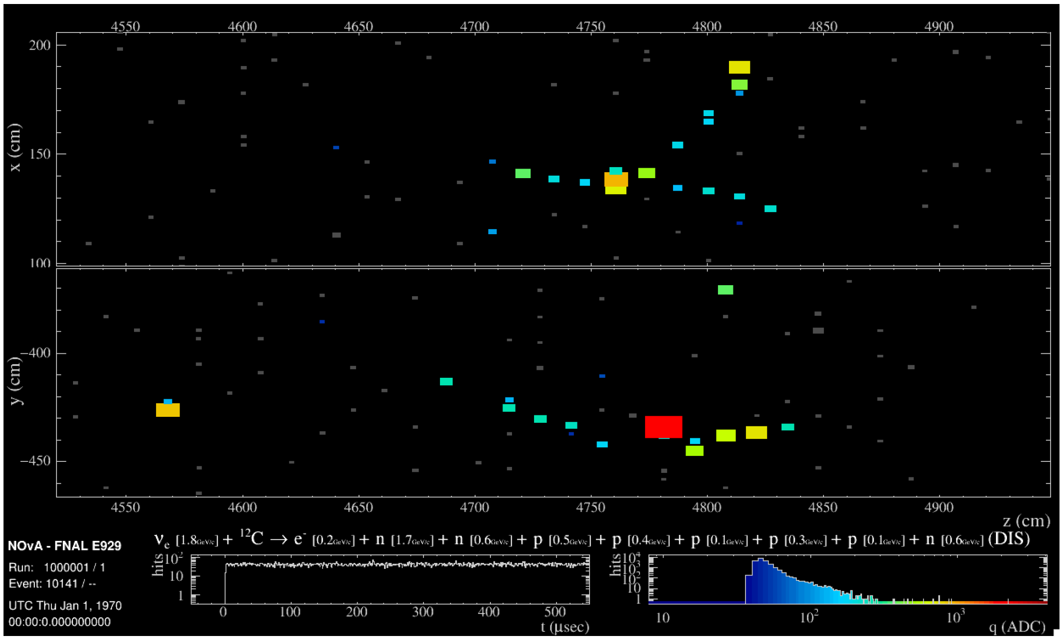

Figure 6.1: A simulated atmospheric electron neutrino event. The ν_e with a momentum of 1.8 GeV/c impinges on a ^{12}C nucleus producing various hadronic particles. This event mimics an antineutron annihilation in terms of both topological and energy characteristics.

currently employs the former one. The details of this flux model can be found in the Appendix C.

A package is to simulate the atmospheric neutrinos in the NOvA's FD, providing that a flux model is given as an input. The author has been able to successfully produce a simulated atmospheric neutrinos dataset using the BGLRS flux. Figure 6.1 shows an example display of an event in the dataset. However, a background model regarding the atmospheric neutrinos has not been complete as we lack a tool to validate the input flux model. There is a caveat in applying the currently available flux models in the simulation setup of NOvA: none of them computed the flux specific for the NOvA's FD site. Instead, we have to use the flux calculated for the Soudan underground mine, which locates 40 miles away. Even though the two sites are quite close, differences in the geomagnetic field and the overburden depths need to be studied to validate the use of this flux model.

6.2 Cosmic Rays Induced Background

The second and also contemplated to be the dominant source of backgrounds for the search of neutron-antineutron oscillation is the cosmogenics neutrons. When a high energy cosmic muon collides with an atomic nucleus of the atmospheric layers above the FD, it induces a cascade of hadronic particles. Fast neutrons with energy upto a few GeV can travel a large distance from the cascade and, due to being neutral particles, enter the detector's inner volume without leaving any traces. Once being insides, this neutron can scatter off the nuclei of the detector's materials and produce recoil shower(s). These showers have a topological trait similar to that of an antineutron annihilation. Among them, those with an appropriate visible energy will contribute the background of the search.

6.2.1 Cosmogenic Neutrino Simulation with CORSIKA

A solid background model requires the estimation of cosmogenic neutron flux into the FD. The current approach is simulating the air showers induced by high energy cosmic primaries including protons and atomic nuclei. Among the secondaries in the cascade, fast neutrons will be sampled to transport to the FD. An energy cut ($E > 500\,\mathrm{MeV}$) is applied to the neutrons that reach the FD to cut down the number of particles need to be simulated in the Geant4.

The air shower simulation is handled by `CORSIKA` v7.70 [131] (**CO**smic **R**ay **SI**mulations for **KA**scade). This is a Monte Carlo simulation program developed to study the evolution and properties of extensive air showers in the atmosphere, see Figure 6.2. `CORSIKA` incorporates a variety of models to handle the hadronic and electromagnetic interactions at both high ($> 100\,\mathrm{GeV}$) and low energy regimes. For the work presented in this thesis, a large library of simulated air showers induced by primary protons using the physics models listed in Table 6.1 is produced.

	Physics Models
High-Energy Hadronic Interaction	DPMJET [132]
Low-Energy Hadronic Interaction	GHEISHA [133]
Electromagnetic Interaction	EGS4 [134]

Table 6.1: Physics models of the CORSIKA simulation used in this work.

A custom package called `CORSIKAGen` is developed to sample the secondary particles in the air shower library and port them to the Geant4 step in the NOvA simulation chain. This algorithm addresses the normalization of the primary particle flux, the detector surface coverage, as well as the offset in position and timing of secondary particles entering the detector geometry. An example of simulated cosmic particles from `CORSIKA` generator is shown in Figure 6.3.

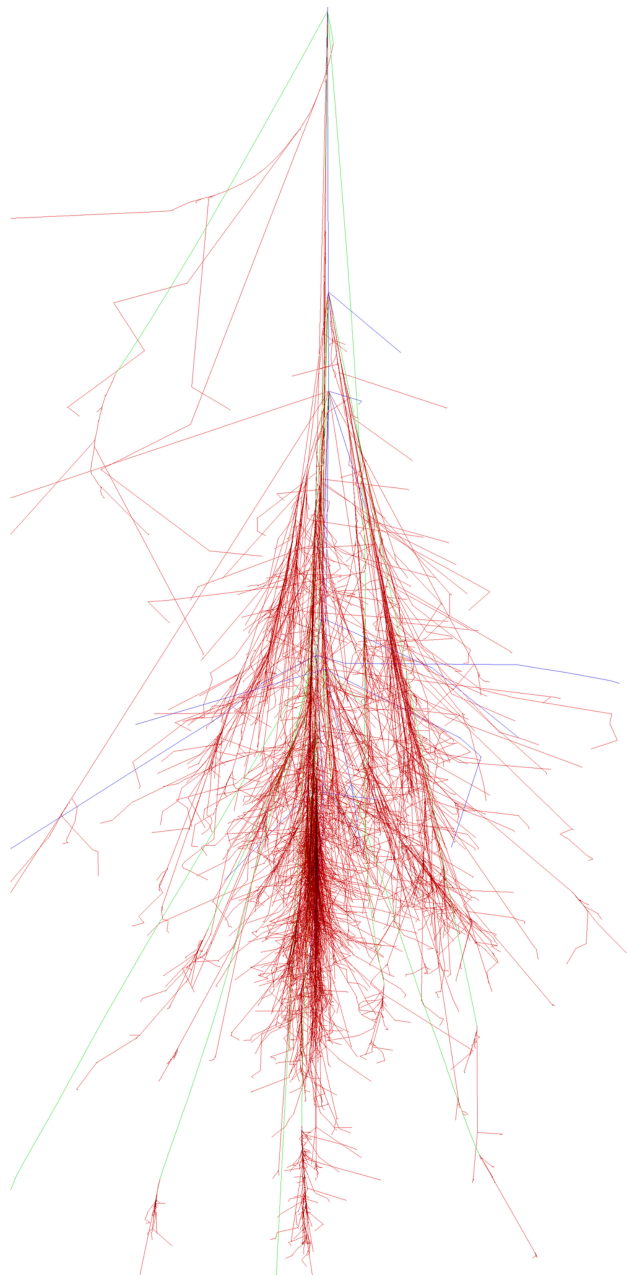

Figure 6.2: Display of an air shower induced by a primary proton at 100 GeV.

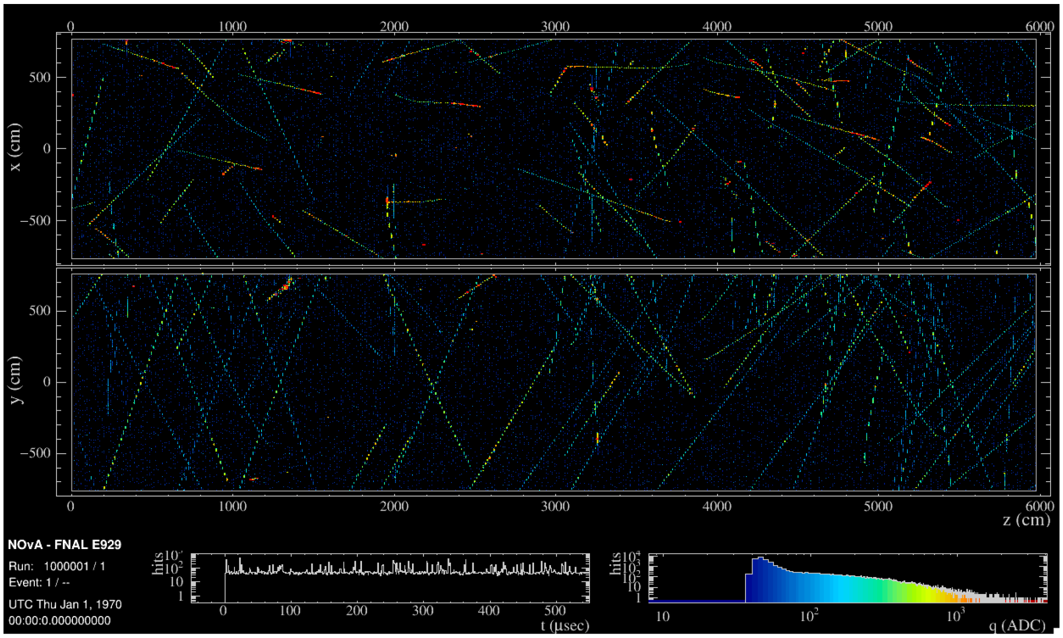

Figure 6.3: Display of a simulated cosmic particles event record. The particles shown in the event display are secondaries sampled from a library of `CORSIKA` air showers.

6.2.2 Model Validation

To validate this background model, the `CORSIKAGen` secondary particles' rates and spectra that enters the FD are compared against those generated by CRY [124]. CRY is a package to generate correlated cosmic-ray particle showers which has been used in NOvA since the beginning of the experiment. Despite a couples of drawbacks[3], CRY provides a good baseline for the validation purposes.

[3]CRY has a limited hadronic interaction model. Also, it only provides the flux of cosmic ray particles for three elevations: at sea level, at 2100 m, and at 11300 m. The sea level CRY flux is used in the NOvA simulation even though the FD actually lies about 330 m above it.

First, the rates of the secondaries passing through the FD during the same exposure of 1 second are considered, see Table 6.2. Three is an agreement in the rates of muons, electrons and gammas produced by CRY and the custom `CORSIKAGen`. However, the `CORSIKAGen` shows to produce a lot more protons and neutrons. The reason of this discrepancy is being studied.

	CRY	**CORSIKA**	**Difference**
muon	112692	103981	-7.7%
electron	9272	9301	+0.3%
proton	1556	3860	+148%
neutron	13553	38244	+182%
gamma	18972	19816	+4.4%

Table 6.2: A comparison of the rates of different secondary particle generated by CRY and `CORSIKAGen`.

Second, the distributions of momentum, azimuthal and zenith orientations of each types of secondary particles are examined, see Figures 6.4, 6.5, 6.6, 6.7 and 6.8 below. These spectra shows a good agreement between the results of CRY simulation and the custom developed package `CORSIKAGen`.

One major difficulty in the continuing development of this background model is the huge amount of computing time needed. The most timing consuming steps are (i) the CORSIKA simulation of secondary particles to build an air shower library and (ii) the Geant4 simulation of a large number of particles in the large detector geometry. Currently, there is no good solution to the former problem. As we want to enlarge the air shower library to improve the statistics, we have to deal with the extensive simulation time. For the latter issue, we are working on an improvement to the sampling algorithm in which only neutrons are kept for Geant4 detector simulation.

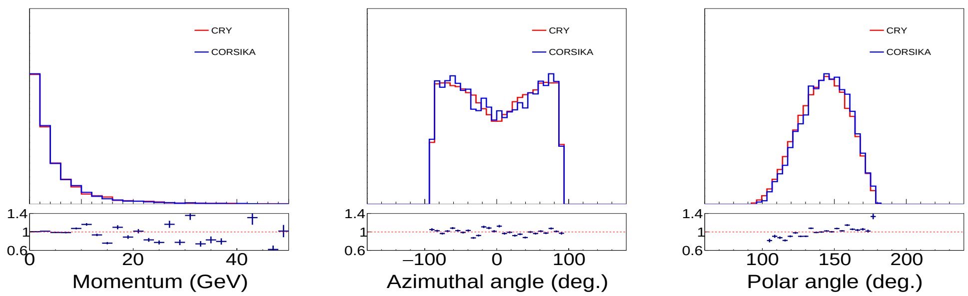

Figure 6.4: Distributions of momentum (left), azimuthal angle (center), and polar angle (right) of muons in CRY (red) and `CORSIKAGen` (blue).

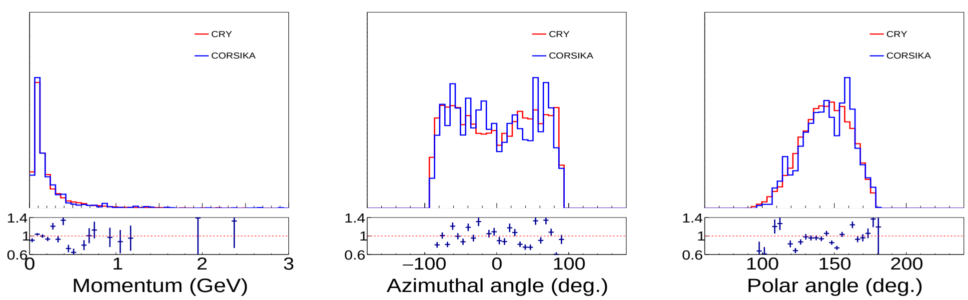

Figure 6.5: Distributions of momentum (left), azimuthal angle (center), and polar angle (right) of electrons in CRY (red) and `CORSIKAGen` (blue).

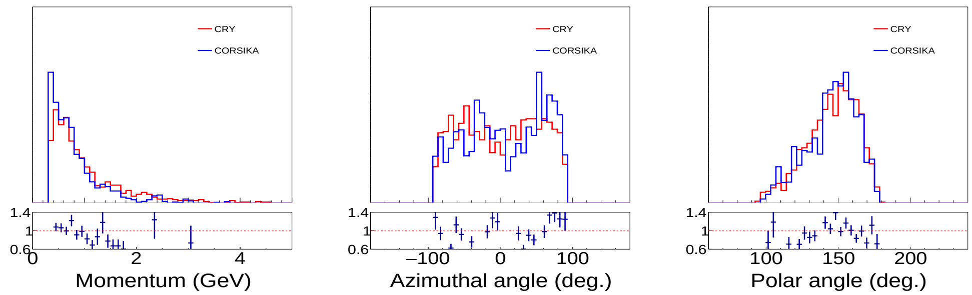

Figure 6.6: Distributions of momentum (left), azimuthal angle (center), and polar angle (right) of protons in CRY (red) and `CORSIKAGen` (blue).

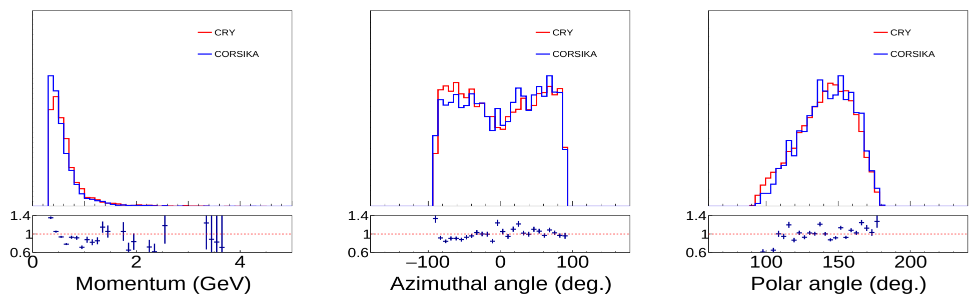

Figure 6.7: Distributions of momentum (left), azimuthal angle (center), and polar angle (right) of neutrons in CRY (red) and `CORSIKAGen` (blue).

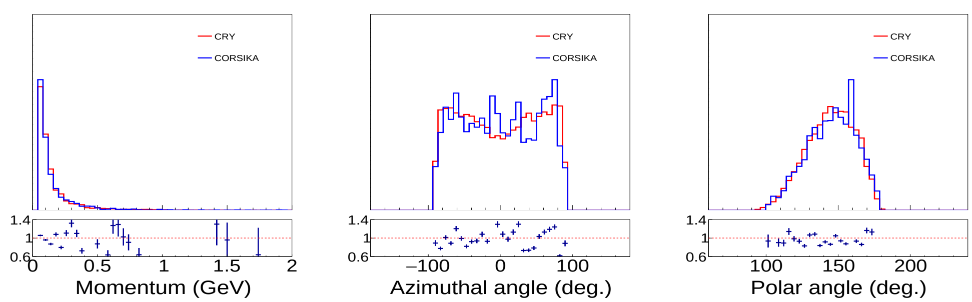

Figure 6.8: Distributions of momentum (left), azimuthal angle (center), and polar angle (right) of gammas in CRY (red) and `CORSIKAGen` (blue).

6.3 Data-Driven Background Model

Due to the incompleteness of the background models as discussed above, for the study presented in this thesis, we chose a data-driven approach to the background estimation of the search. We decided to unblind 30% of the real data under an assumption that all the events contained in it are background. This together with a simulated signal dataset are used in the development of the event selection and background estimation, which will be explained in more details in the next Chapter. The rest 70% of the data is only disclosed when all the aspects of the analysis has been finalized to avoid any bias from experimenters.

Chapter 7

Data Analysis Procedure

7.1 Event Reconstruction

7.1.1 Single Cell Hit Reconstruction

The building blocks of the raw data are `RawDigits`. They represents the signal from APD pixels when a hit with an amplitude larger than a set threshold is registered. A `RawDigit` contains basics information like the cell and plane numbers of the hit, as well as the waveform of the APD's signal in the form of arrays of ADC and TDC values of the sampling points, see Figure 7.1. The first step in the reconstruction chain is to turn a `RawDigit` into a `CellHit` which add the number of photoelectrons (PE) and the hit start time in nanoseconds to the information already available at the `RawDigit` level. In the NOvA's analysis software suite, this conversion is carried out by a package called `CalHit`.

The PE can be found via a simple conversion

$$\mathrm{PE} = S_{\mathrm{peak}} \times C, \tag{7.1}$$

where S_{peak} is the ADC value of the peak of the waveform, and C is the conversion factor between ADCs and PEs. For the FD, with the APDs operating at a gain factor of 140 the value of C is 2.8 ADC/PE. It's important to notice that the PE value here is not taking into account the fiber attenuation whose value requires the x, y, z position of the hit to be estimated.

The time T_0 of a `CellHit` is calculated by fitting the sampled waveform of the APD signal to a known response function of the form

$$S(t) = A \times \exp\left(-\frac{t - T_0}{\tau_{\text{fall}}}\right) \times \left[1 - \exp\left(-\frac{t - T_0}{\tau_{\text{rise}}}\right)\right] + B, \tag{7.2}$$

where A is the normalization factor which depends on the PE, B is the detection threshold chosen to be about 35 ADC or 12.5 PE (equivalent of 0.5 MIP in the NOvA liquid scintillator), τ_{rise} of 380 ns and τ_{fall} of 7 μs are, respectively, the fall time and rise time of the signal model [17].

7.1.2 Interaction Clustering

An event record collected by the `NNbarDDT` contains the cell hits from all the interactions that happen in the detector in a time window of 50 μs. Among those hits, there exists at least, and most of the time, one neutron anti-neutron oscillation candidate, see Figure 7.2. The process to find all hits associated with this candidate event is described in this section.

After the single cell hit reconstruction, a package called `Slicer4D` [135] is employed to group the cell hits into the interaction clusters they belong to. `Slicer4D` clustering is based on the DBSCAN algorithm [136]. In this algorithm, two classes of hits are defined: (i) core points are cell hits that have more than the minimum number of neighbors lying within a distance

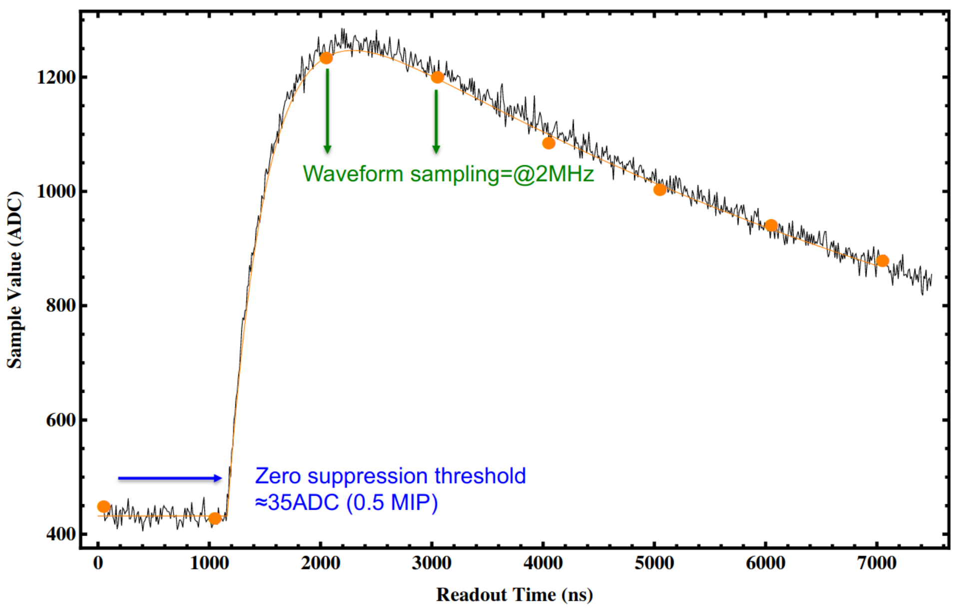

Figure 7.1: The sampling points of an APD signal waveform are shown by the orange dots. The solid orange line is the known response function (7.2) fitted to the data. The plot is taken from [17].

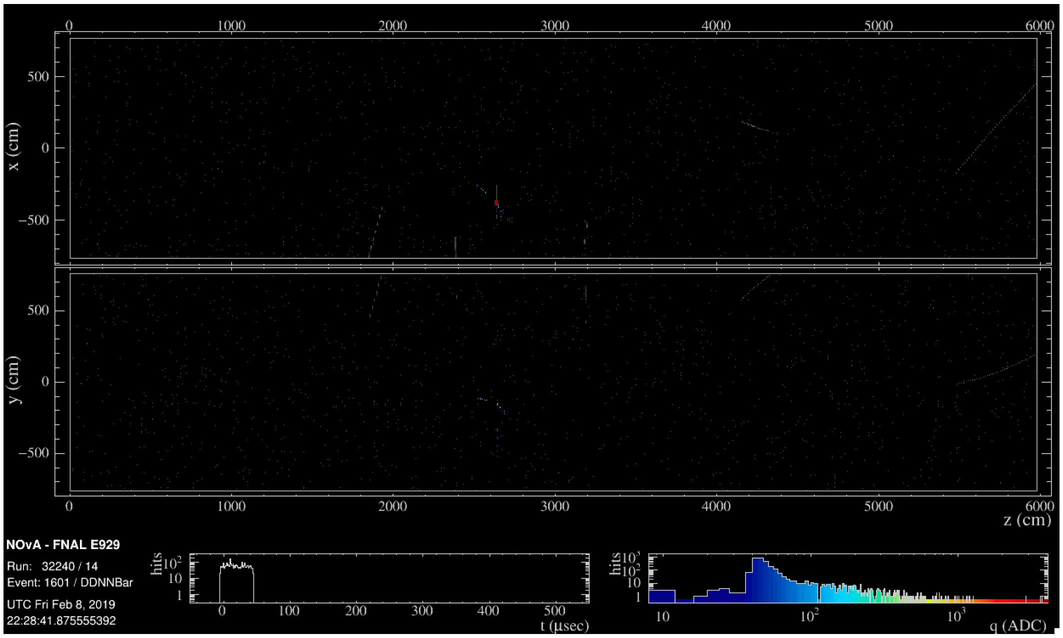

Figure 7.2: A display of a `NNbarDDT` event record. The signal-like cluster, highlighted by the ADC-scaled colors, is found thanks to the `Slicer4D` and `NNbarFilter` steps. Hits of noises and cosmic muons interactions are shown in gray.

threshold, and (ii) border points are cell hits have less than the minimum number of neighbors, see Figure 7.3. A border point is included in the cluster if it is a neighbor of at least one core point. `Slicer4D` starts by looping over each cell hit, determining whether the hit a core point. If it is, a cluster is initiated and this hit is immediately added to this cluster. `Slicer4D` then extends the search to all neighbors of that initial hit, and add them to the same cluster if they are also core points. The stopping condition of the algorithm is that all core-searching branches end up with border points. Unclustered cell hits are marked altogether as a noise cluster.

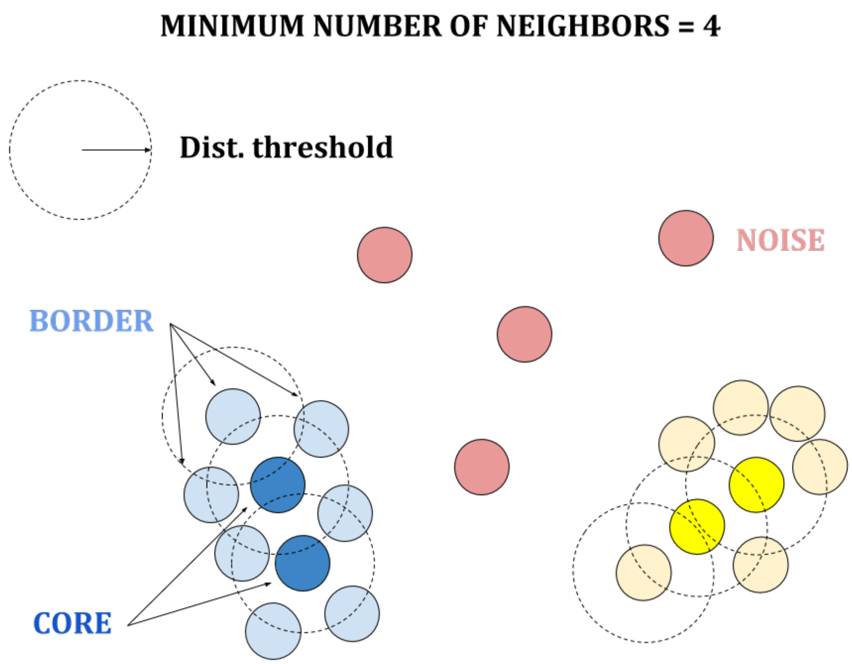

Figure 7.3: An illustration of DBSCAN algorithm with the minimum number of neighbors of 4 and the distance threshold is represented by the dashed circle. Two clusters of hits are found and color-coded in blue and yellow. Core points are shown in dark tone while border points are in lighter tone. The unclustered point is marked as a noise.

To determine if two hits are neighbors of each other, a score function is defined. This function put a penalty on the space-time distance between the hits as well as hits with low PE values [135], which poses a high chance of being noise. The function takes the form

$$\epsilon = \left(\frac{\Delta t - d/c}{T_{\text{res}}}\right)^2 + \left(\frac{\Delta z}{D_{\text{pen}}}\right)^2 + \left(\frac{\Delta xy}{D_{\text{pen}}}\right)^2 + \left(\frac{\text{PE}_{\text{pen}}}{\text{PE}}\right)^2. \tag{7.3}$$

In the time penalty term, Δt is the difference in the start times of two hits and T_{res} is the timing resolution. For PE penalty term, PE is the number of photo-electrons of both hits added in quadrature, and $\mathrm{PE_{pen}}$ is a penalty parameter whose value makes the PE penalty term being 1. When applying the DBSCAN algorithm to NOvA data, a minor complication comes from the fact that the detector has two view (XZ and YZ). When considering two hits in the same detector view, d is simply the 2D distance between the hits. On the other hand, in the case two hits in consideration are in two different views, Δxy is set to 0, d becomes the 1D distance in z-axis. The D_{pen} takes a value so that distance penalty (the sum of the 2^{nd} and 3^{rd} terms in (7.3) in the case of same view hits, and just the 2^{nd} term in the case of different view hits) being 1.

The xy correlation of a hit with its neighbors that lie in the other view allows the estimation of its distance from the readout. This piece of information is crucial in calculating the fiber attenuation factor and, in turn, the `PECorr` - the photo-electrons produced at the point where a charged particle passes through a cell. Using the results of energy calibration, this value of `PECorr` is converted into the energy the particle deposited in the cell. The x, y, z, `PECorr` and energy deposition, together with the information already available in the `CellHit` will be packaged in a new object called `RecoHit`. Each hit in an interaction cluster will be associated with a `RecoHit`.

After the interaction clusters have been identified, a filter called `NNbarFilter` is used to single out the signal-like from the rest of the event record. This filter is basically an offline version of the `NNbarDDT` which proved effectiveness in removing the cosmic muon tracks while retaining the multi-prong spherical events. The signal-like events will be saved separately for further reconstruction steps. Figure 7.2 shows an example of `NNbarDDT` event record that has gone through both the slicer and the signal filter. Cell hits of the signal-like interaction are color-coded by their ADC values.

7.1.3 Vertex Reconstruction

An important step in reconstructing a neutron anti-neutron oscillation event is to find the vertex of the interaction. In the NOvA's analysis software suite, a vertex finding algorithm called `fuzzykvertex` is already developed to handle the case of the neutrino interactions. However, when applied to the neutron oscillation search, the conventional `fuzzykvertex` usually fails to locate the correct vertex due to a high hadron multiplicity. For this reason, a different vertex finding method is developed for this study.

First, we study the characteristics of the true vertex which is readily available in the signal simulation. In particular, we will consider how the energy deposition is distributed with respect to the true vertex. Call the energy of the i-th hit in a cluster E_i. The number η_i indicates whether the i-th hit is in top view (XZ view) with $\eta_i = 0$, or side view (YZ view) with $\eta_i = 1$. Lastly, $x^{(v)}, y^{(v)}, z^{(v)}$ and x_i, y_i, z_i are the coordinates of the true vertex and i-th hit, respectively. We define $\mathcal{R}_x^E$, $\mathcal{R}_y^E$, $\mathcal{R}_z^E$ as the ratios of the sums of the energy of the hits that satisfy

$$\begin{cases} \eta_i = 0 \\ x_i > x^{(v)} \end{cases}, \begin{cases} \eta_i = 1 \\ y_i > y^{(v)} \end{cases}, z_i > z^{(v)}$$

respectively, to the total visible energy of the cluster

$$E^{\text{vis}} = \sum_i E_i.$$

In other words, $\mathcal{R}_x^E$, $\mathcal{R}_y^E$, $\mathcal{R}_z^E$ tell us the what proportion of the energy is deposited to one side with respect to the vertex in each dimension X, Y or Z respectively. The quantities can also be written explicitly as

$$\mathcal{R}_x^E = \frac{\sum_{i=0}^{N}(1-\eta_i)\ \theta\left(x_i - x^{(v)}\right) E_i}{\sum_{i=0}^{N} E_i},$$

$$\mathcal{R}_y^E = \frac{\sum_{i=0}^{N}\eta_i\ \theta\left(y_i - y^{(v)}\right) E_i}{\sum_{i=0}^{N} E_i},$$

$$\mathcal{R}_z^E = \frac{\sum_{i=0}^{N}\theta\left(z_i - z^{(v)}\right) E_i}{\sum_{i=0}^{N} E_i},$$

in which, N is the total number of hits, $\theta(x)$ is the step function

$$\theta(x) = \begin{cases} 0 & (x < 0), \\ 1 & (x \geq 0). \end{cases}$$

Figure 7.4 shows the distributions of $\mathcal{R}_x^E$, $\mathcal{R}_y^E$, $\mathcal{R}_z^E$ in a sample of 100k simulated $n + \bar{n} \to \pi^+ + \pi^- + \pi^0$ events. Due to the symmetrical nature of signal events, the total energy will have a tendency to split up equally between the XZ and the YZ views. The distributions of $\mathcal{R}_x^E$ and $\mathcal{R}_y^E$ centering about 0.25 and of $\mathcal{R}_y^E$ centering about 0.5 are indication that cell hits energy, on average, is symmetrically spread around the true vertex.

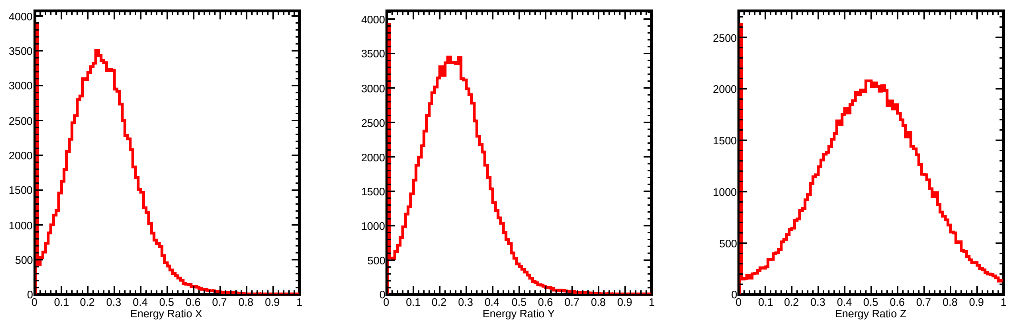

Figure 7.4: Symmetrical spreading of hit energy around the true vertex of a simulated signal event is shown by the distributions of $\mathcal{R}_x^E$ (left), $\mathcal{R}_y^E$ (center), and $\mathcal{R}_z^E$ (right).

As a result, we can define an algorithm looking for the vertex of a signal candidate using the visible energy and topology of its cell hits. The reconstructed vertex is set to be the point of energy balancing. In particular, we define the energy ratios as functions of coordinates of hits

$$R_x^E(x) = \frac{\sum\limits_{i=0}^{N}(1-\eta_i)\ \theta\left(x_i - x\right) E_i}{\sum\limits_{i=0}^{N} E_i},$$

$$R_y^E(y) = \frac{\sum\limits_{i=0}^{N}\eta_i\ \theta\left(y_i - y\right) E_i}{\sum\limits_{i=0}^{N} E_i},$$

$$R_z^E(z) = \frac{\sum\limits_{i=0}^{N}\theta\left(z_i - z\right) E_i}{\sum\limits_{i=0}^{N} E_i}.$$

The coordinates $x_{\text{Reco}}^{(v)}$, $y_{\text{Reco}}^{(v)}$, $z_{\text{Reco}}^{(v)}$ of the reconstructed vertex is then found by solving this set of equations

$$\begin{cases} R_z^E(z_{\text{Reco}}^{(v)}) = 1/2 \\ R_x^E(x_{\text{Reco}}^{(v)}) = 1/4\ . \\ R_y^E(y_{\text{Reco}}^{(v)}) = 1/4 \end{cases} \tag{7.4}$$

Physically, this means the energy of all of the hits to the left of the vertex is equal to the energy of all the hits to the right of it. Similarly for other dimensions (up/down, front/back).

To find the time coordinate of the vertex, a regression is performed, see Figure 7.5. The hits that lie within a region aggregating 50% of the total visible energy of the event are selected. Their distances to the reconstructed vertex are plotted against their timing. A simple linear regression is performed to find the timing corresponding to the distance value of 0. This is then set to be the time of the reconstructed vertex.

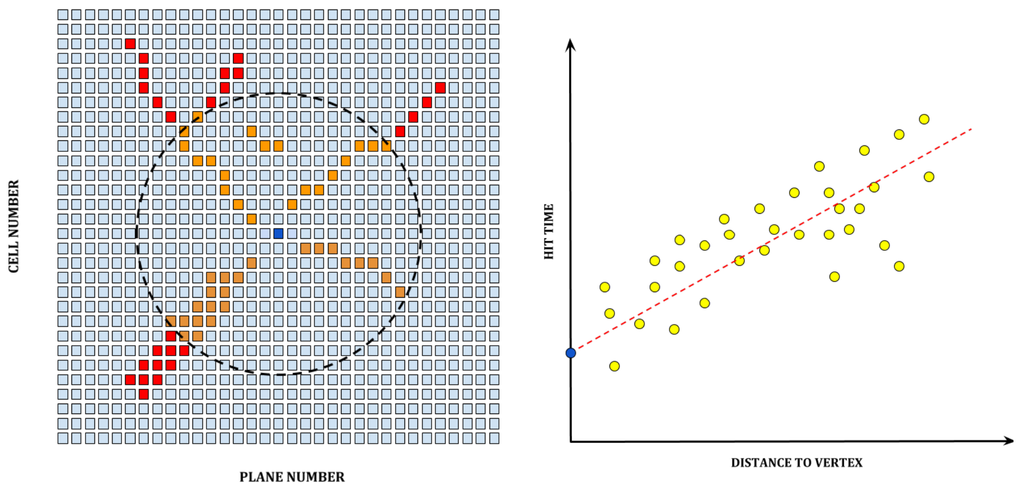

Figure 7.5: An cartoon illustrating the method of finding the vertex's time. In the event display (left) the blue point indicates the position of the reconstructed vertex. A dashed circle shows the selection region. The sum of energy from hits within this circle accounts for 50% of the event's total energy. Selected hits are marked in orange. Timing regression (right) is performed to find the timing of the reconstructed vertex.

7.1.4 Prong Reconstruction

One of the prominent signatures of a neutron anti-neutron oscillation event is the high multiplicity of hadrons, mostly pions. To take advantage of this characteristics, previous searches usually try to calculate the number of prongs [58, 59] or similar quantities such as number of Cherenkov rings [2, 60] and incorporate it in the selection algorithm. Understand the benefits that this approach can bring to the analysis, efforts in developing a prong reconstruction with limited PID ability has been expended. However, this is an ongoing work and needs more time to be completed. The event selection presented in this work does not rely on any prong-related variable cuts.

7.2 Event Selection

The backbone of this search is the event selection algorithm which distinguishes the signal candidates from the background. Due to the lack of a robust background model, as mentioned in Chapter 6, the search resorts to a data-driven strategy in which the real data is partially unblinded and used for the development of the analysis. Only after all aspects of the analysis have been finalized, the rest of the data is disclosed.

As of August 5th, 2020, the `NNbarDDT` has aggregated 693.3 days worth of exposure. The study in this thesis unblinds the data collected from 9/6/2018 to 1/1/2019, which is about 15% of the total amount. We treat this dataset under a conservative assumption that all signal-like events contained in it are background. It is mainly used to evaluate the background rejection ability of the event selection. Another use of it is in the background estimation which is addressed in the next section. This dataset contains 28,670,930 event records. After undergoing the reconstruction process, a total of 26,660,745 signal-like clusters was identified and retained.

The signal model is available via a dataset of 1.2 million simulated neutron oscillation events which includes all 16 anti-neutron annihilation channels. Before going through the event reconstruction, the `NNbarDDT` was applied to these simulated event to mimic the effect of detector trigger. 688,442 event records was retained after the DDT process. After the reconstruction, 640,613 simulated signal clusters remain.

7.2.1 Selection Variables

The event selection in this study utilizes 9 variables. In this section, we will discuss how to compute theses variables, their physics meanings, as well as their performances in background rejection and signal selection.

7.2.1.1 Hit Counts in XZ and YZ Views

The number of hits in each view, Figure 7.6, and their difference, Figure 7.7, are the first set of variables used for the selection. While the signal has a spherically symmetric topology that leads to an equal distribution of hits between XZ and YZ views, the background of atmospheric neutrinos and cosmogenic neutrons both have a tendency of depositing slightly more hits into the YZ view due to a vertical direction preference of those particles, see Figure 7.7.

7.2.1.2 Energy-related Variables

Total visible energy is an important variable to distinguish the signal candidates from the background. As previously discussed in Section 4.4, a neutron-antineutron oscillation event will deposit an energy of about 1-2 GeV in the detector. This total visible energy is calculated simply as the sum of reconstructed energy from all the hits in the cluster. Figure 7.8 shows the distinction between the visible energy distributions of the simulated signal

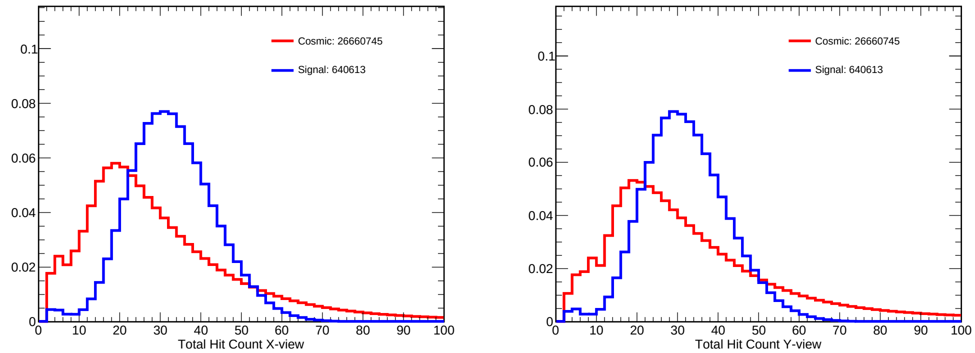

Figure 7.6: Hit counts in XZ (left) and YZ (right) views of the simulated events (blue) and the FD data's signal-like events (red).

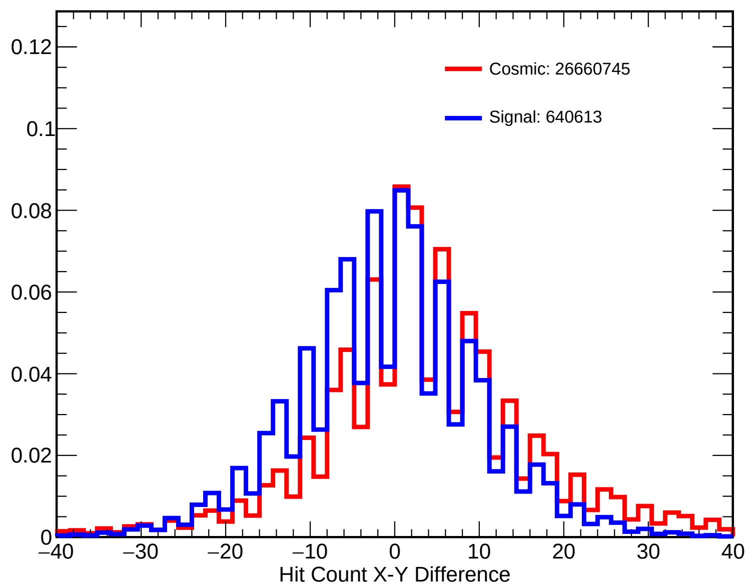

Figure 7.7: Difference between hit counts in XZ and YZ views of the simulated events (blue) and the FD data's signal-like events (red).

events (blue) and the FD data's signal-like events (red).

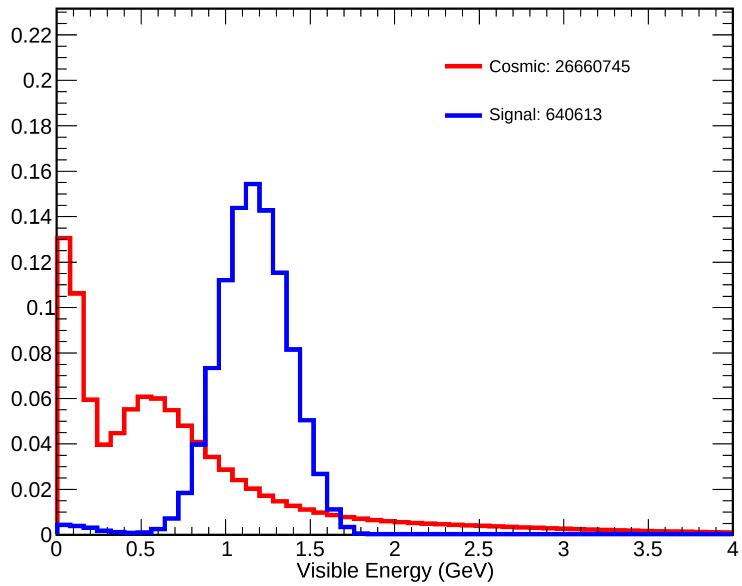

Figure 7.8: Visible energy (in GeV) distributions of the simulated events (blue) and the FD data's signal-like events (red).

Another set of energy-related variables that show a good distinction between the signal and background are the average hit energy in XZ and YZ views, see Figure 7.9. This variable is simply quotient between the total visible energy of all the hits and the hit count in each view.

7.2.1.3 Timing Variables

Timing of an event also plays an important role in separating the signal from the background. Two timing variables considered in this study are (i) the duration (in ns) of an event, Figure 7.10 and (ii) the correlation between the timing of a hit and its distance from the vertex.

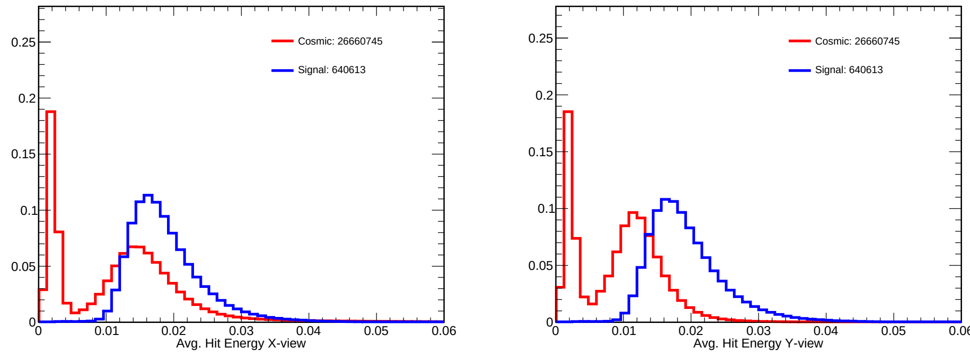

Figure 7.9: Distributions of average hit energy (in GeV) in XZ (left) and YZ (right) views of the simulated events (blue) and the FD data's signal-like events (red).

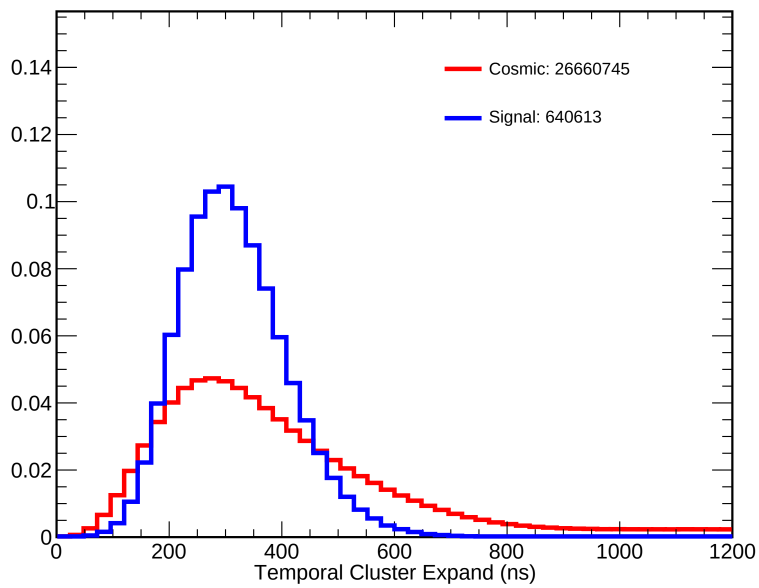

Figure 7.10: Time duration (in ns) distributions of the simulated events (blue) and the FD data's signal-like events (red).

The method to calculate this hit position-timing correlation is similar to the one used to figure out the vertex timing shown in Section 7.1.3. First, a region that contains 90% of the visible energy of the event is defined. The timing and distance to the vertex from all the hits in this region will then be placed in a scatter plot, similar to the one in Figure 7.5. The correlation factor of this scatter plot is calculated using the `TGraph::GetCorrelationFactor()` method [137] and used as the selection variable shown in Figure 7.11.

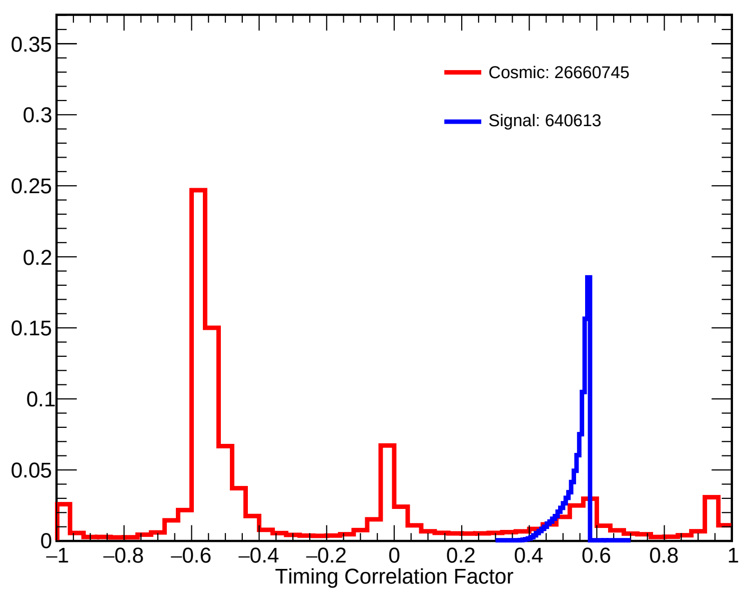

Figure 7.11: Hit position-timing correlation distributions of the simulated events (blue) and the FD data's signal-like events (red).

For signal events, hits closer to the reconstructed vertex will likely to happen earlier than the hits further away. This drives the signal's hit position-timing correlation factor to a positive value, close to 1. On the other hand, atmospheric neutrinos and cosmogenic neutrons come into the detector with non-zero momenta. As a result, hits on the incoming side with respect to the reconstructed vertex will happen earlier than those on the outgoing side. Thus, the position-timing symmetry with respect to the vertex is not retained for the background events. Distribution of the correlation factor, Figure 7.11, shows a clear distinction between the signal and the background.

7.2.1.4 Vertex y Position

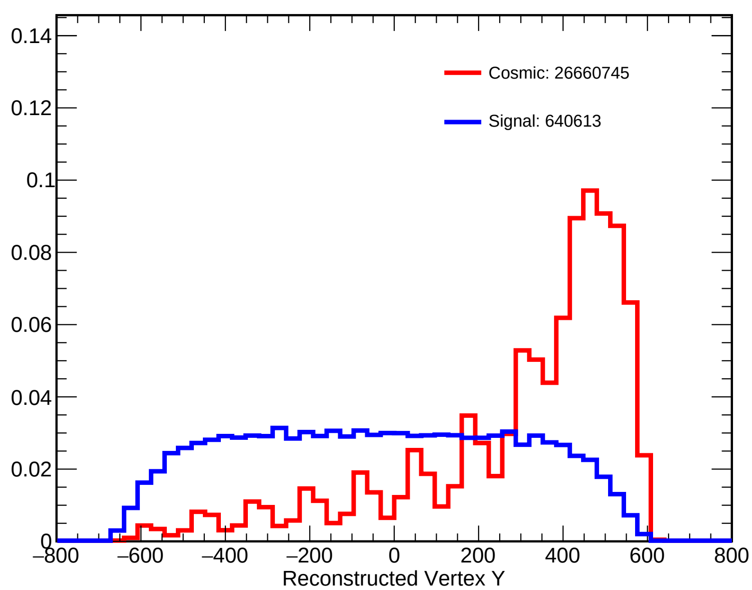

Figure 7.12: Vertex's reconstructed y position (in cm) distributions of the simulated events (blue) and the FD data's signal-like events (red).

Lastly, the y position of the reconstructed vertex is considered. The signal are random events that can happen anywhere within the detector volume. However, the background has a tendency of occurring in the upper section of the detector, see Figure 7.12.

7.2.2 Selection Cuts

In this study, we use the most basic selection method of applying rectangular box cut on each selection variable. First attempt on multivariate methods is in progress and only outlined in the Appendix D.

The list of cuts are summarized in Table 7.1. They are manually optimized to aggressively remove the number of background events while achieving a decent signal efficiency.

Cut 1	$\texttt{TotalHitCountInXView} < 55$
Cut 2	$\texttt{TotalHitCountInYView} < 55$
Cut 3	$\texttt{HitCountXYDifference} < 10$
Cut 4	$0.9\,\text{GeV} < \texttt{TotalVisibleEnergy} < 1.6\,\text{GeV}$
Cut 5	$14\,\text{MeV} < \texttt{AverageEnergyPerHitYView} < 40\,\text{MeV}$
Cut 6	$12\,\text{MeV} < \texttt{AverageEnergyPerHitXView} < 40\,\text{MeV}$
Cut 7	$\texttt{TemporalClusterExpand} < 550\,\text{ns}$
Cut 8	$0.47 < \texttt{PositionTimingCorrelationFactor} < 0.58$
Cut 9	$-600\,\text{cm} < \texttt{ReconVertexY} < -150\,\text{cm}$

Table 7.1: The selection cut applied on each variable.

A set of plots called "$N - 1$ plots" are produced to evaluate the effectiveness of each selection variables. These plots will show the distribution of a variable after cuts on all others except that variable have been applied.

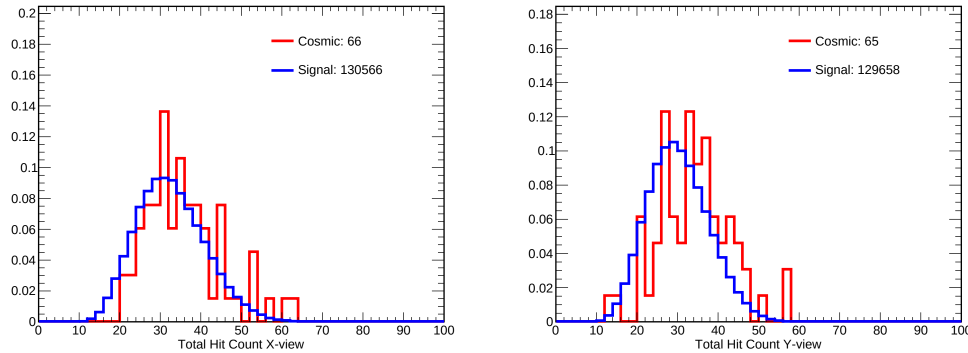

Figure 7.13: The $N-1$ for the total hit counts in XZ view (left) and YZ view (right). Distribution of the variable for the simulated signals and cosmic data backgrounds are shown in blue and red, respectively.

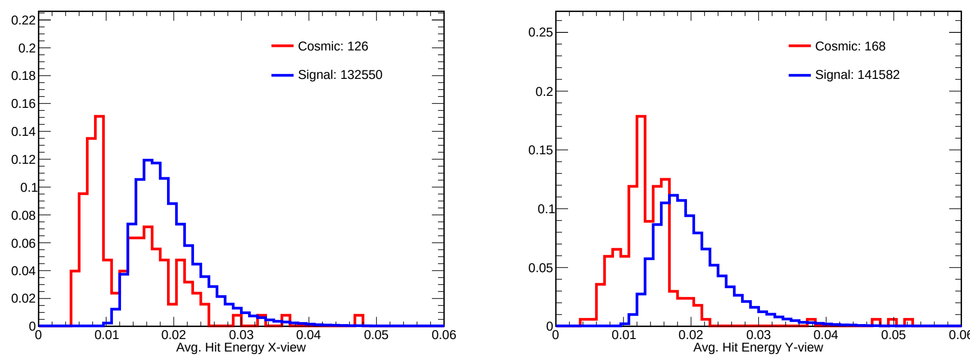

Figure 7.14: The $N-1$ for the average hit energy (in GeV) in XZ view (left) and YZ view (right). Distribution of the variable for the simulated signals and cosmic data backgrounds are shown in blue and red, respectively.

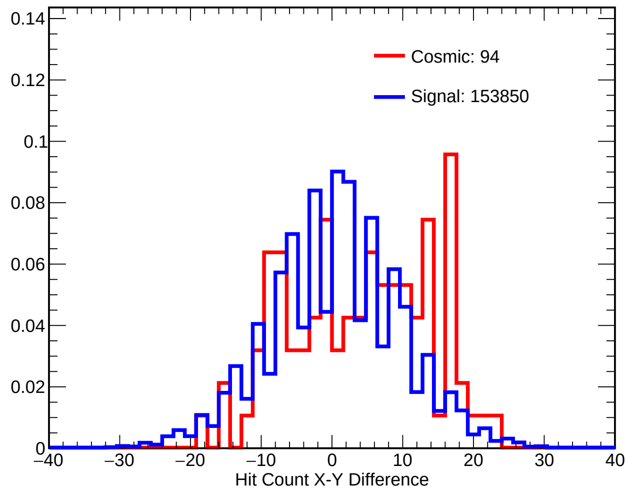

Figure 7.15: The $N-1$ for the hit count difference between the XZ and YZ views. Distribution of the variable for the simulated signals and cosmic data backgrounds are shown in blue and red, respectively.

Via the $N-1$ plots, the variables that show the most potential in separating the signal from the background are the visible energy, the average hit energy in two detector views, the hit position-timing correlation, and z position of the reconstructed vertex.

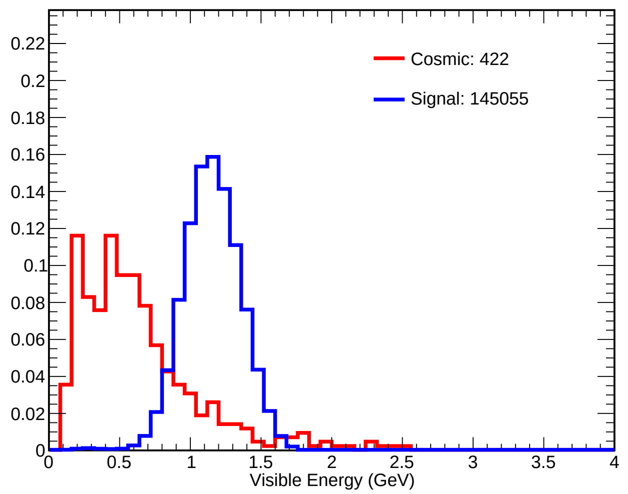

Figure 7.16: The $N-1$ for the total visible energy (in GeV). Distribution of the variable for the simulated signals and cosmic data backgrounds are shown in blue and red, respectively.

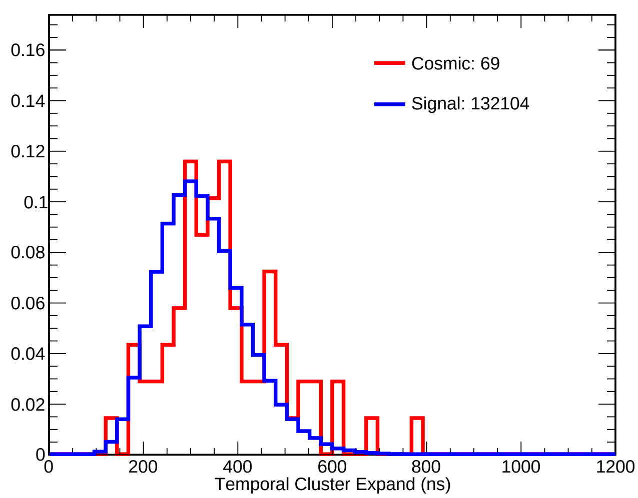

Figure 7.17: The $N-1$ for the time duration of event (in ns). Distribution of the variable for the simulated signals and cosmic data backgrounds are shown in blue and red, respectively.

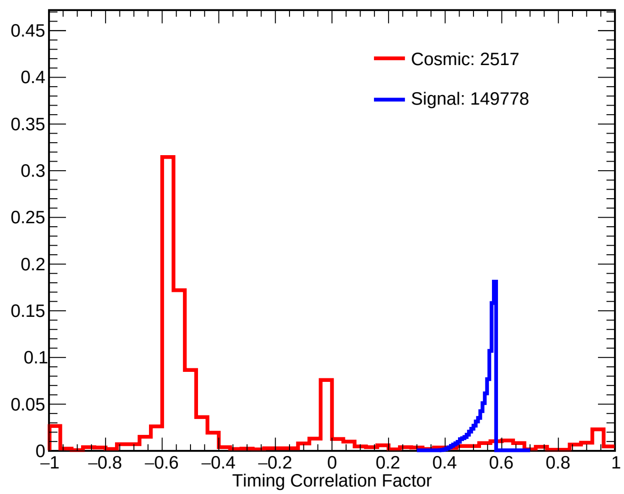

Figure 7.18: The $N-1$ for the hit position-timing correlation factor. Distribution of the variable for the simulated signals and cosmic data backgrounds are shown in blue and red, respectively.

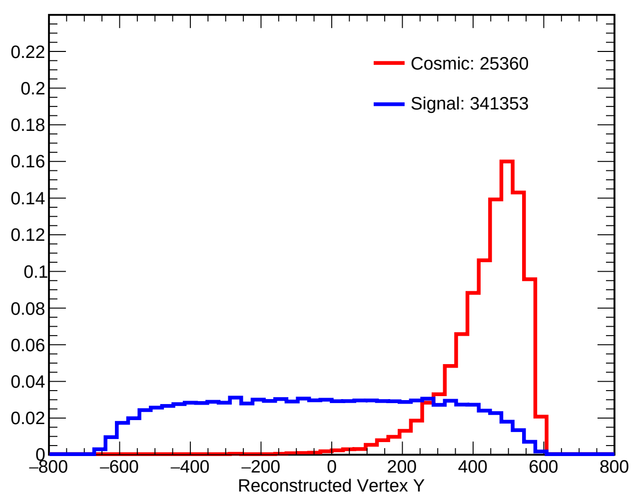

Figure 7.19: The $N-1$ for the y position (in cm) of reconstructed vertex. Distribution of the variable for the simulated signals and cosmic data backgrounds are shown in blue and red, respectively.

7.2.3 All Selection Cuts Applied

The Figures from 7.21 to 7.20 show the distributions of the selection variables after all the cuts specified in Table 7.1 are applied.

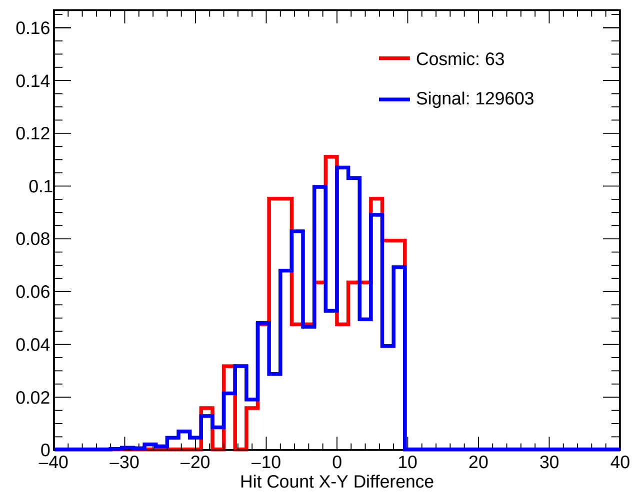

Figure 7.20: Distribution of the hit count difference between the XZ and YZ views after all cuts have been applied. For the simulated signals in blue and for the cosmic data backgrounds in red.

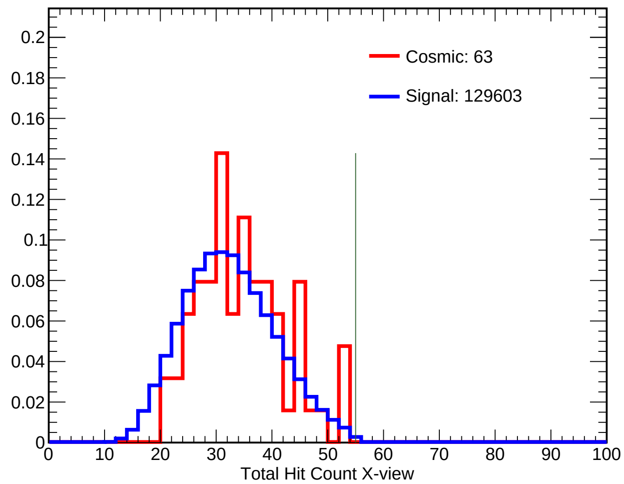

Figure 7.21: Distribution of the total hit count in the XZ view after all cuts have been applied. For the simulated signals in blue and for the cosmic data backgrounds in red.

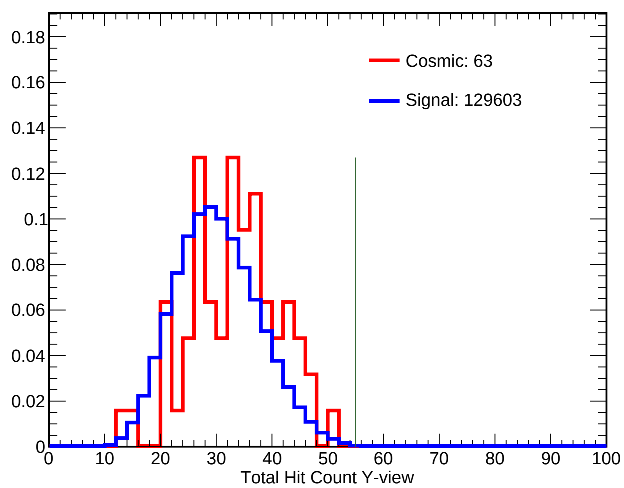

Figure 7.22: Distribution of the total hit count in the YZ view after all cuts have been applied. For the simulated signals in blue and for the cosmic data backgrounds in red.

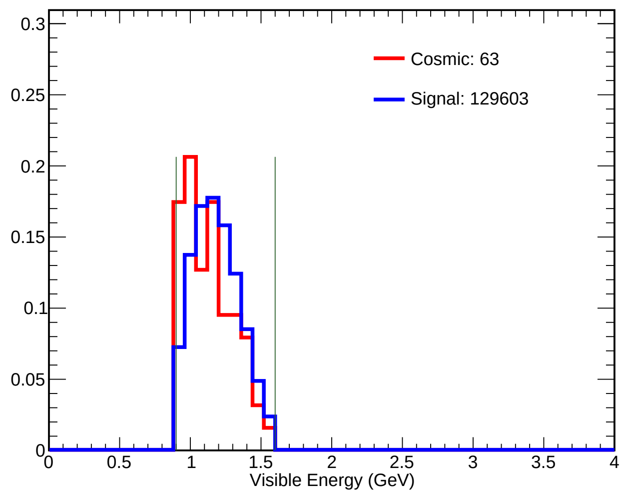

Figure 7.23: Distribution of the visible energy (in GeV) after all cuts have been applied. For the simulated signals in blue and for the cosmic data backgrounds in red.

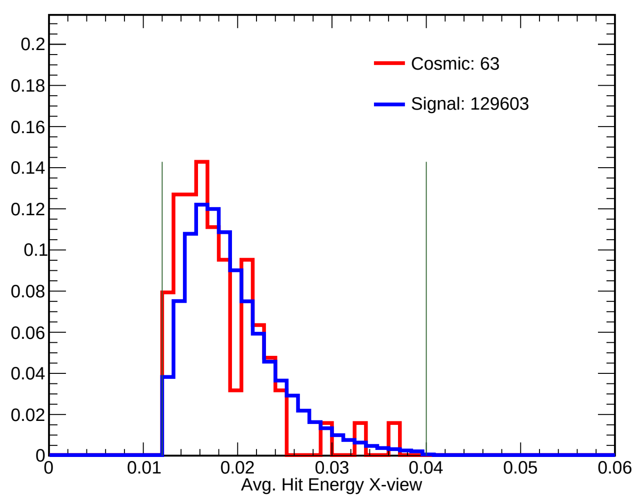

Figure 7.24: Distribution of the average hit energy (in GeV) in the XZ view after all cuts have been applied. For the simulated signals in blue and for the cosmic data backgrounds in red.

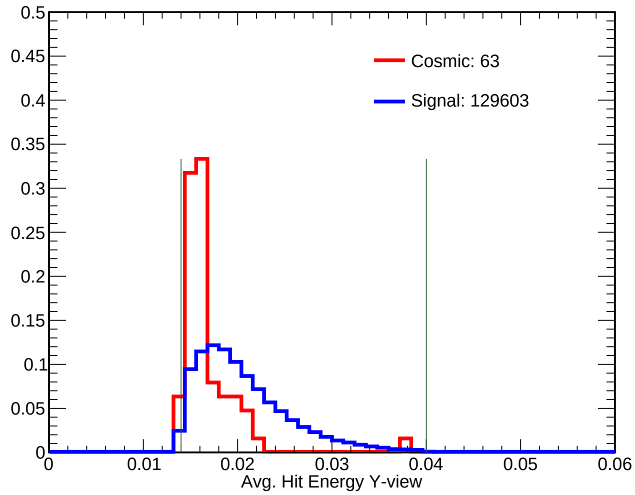

Figure 7.25: Distribution of the average hit energy (in GeV) in the YZ view after all cuts have been applied. For the simulated signals in blue and for the cosmic data backgrounds in red.

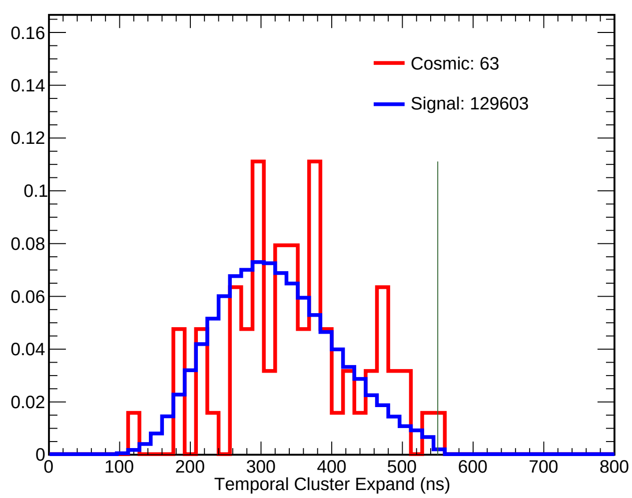

Figure 7.26: Distribution of the event duration (in ns) after all cuts have been applied. For the simulated signals in blue and for the cosmic data backgrounds in red.

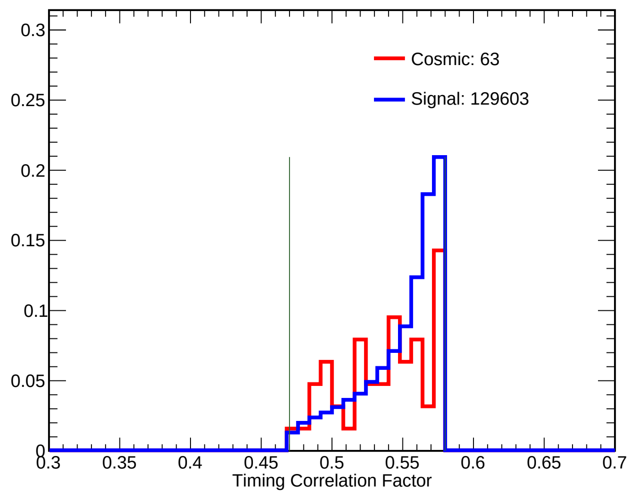

Figure 7.27: Distribution of the hit position-timing correlation factor after all cuts have been applied. For the simulated signals in blue and for the cosmic data backgrounds in red.

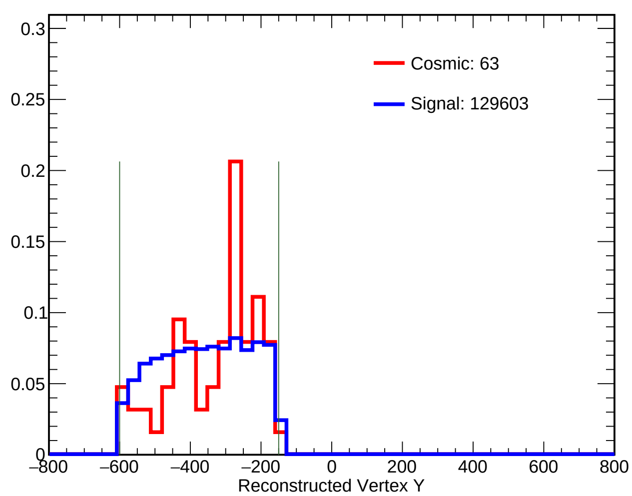

Figure 7.28: Distribution of the y position (in cm) of the reconstructed vertex after all cuts have been applied. For the simulated signals in blue and for the cosmic data backgrounds in red.

After all the cuts are applied, the number of simulated signal events retained is 129,603. Comparing this to 640,613 events before any cuts are applied, the signal efficiency of the selection cuts is 20.2%. Notice that the signal efficiency in the trigger level, from Section 5.2.7, is 57%. The overall signal efficiency of the search is, therefore, 11.5%.

From a dataset of 4 months running, a total of 63 candidate events survive all the selection cuts. This scales to roughly 190 candidates in a year of exposure. Assuming that the NOvA detector will continue to run until 2028, the `NNbarDDT` setup in 2018 will be able to collect 10 years of data. With 70% of the data blinded and used to derive the final results, the expected number of candidates will be about 190×7 or 1330 events in total.

7.3 Background Estimation

As mentioned previously, the estimation of the background for the search will be using on the partially unblinded data rather than the background model based on simulation.

We will use the side-band method with the $N-1$ distribution of the visible energy (all the cuts except the visible energy cut applied), see Figure 7.29. We are only looking at the energy region from 0.5 GeV to 2 GeV. Events with energy lying outside this region do not constitute a candidate for the search anyway. The signal region, as seen in Section 7.2.2, is between 0.9 GeV annd 1.6 GeV. Thus the side-band is the region $E \in [0.5\,\mathrm{GeV}, 0.9\,\mathrm{GeV}] \cup [1.6\,\mathrm{GeV}, 2\,\mathrm{GeV}]$.

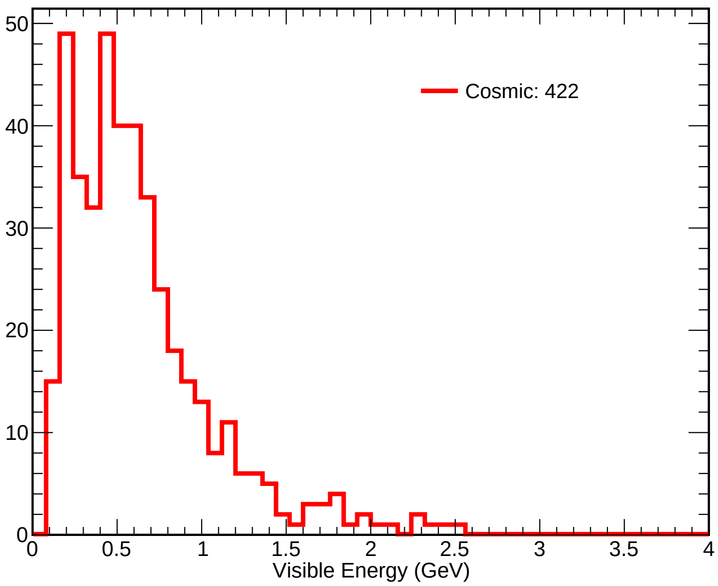

Figure 7.29: $N-1$ plot of visible energy from the FD real data. Side-band regions used for the estimation of the background will be defined based on this distribution.

The side-band is fit with an exponential function of the visible energy, using `RooFit` [138], see Figure 7.30. The total number of events in the side-band is counted as $B_{\rm sb} = 167\,$events. A simple linear relationship between the number of background events in the signal region, $B_{\rm sig}$, and $B_{\rm sb}$ is established

$$\frac{B_{\rm sig}}{B_{\rm sb}} = \frac{1-x}{x}, \tag{7.5}$$

in which, x is the normalized area under the fitting curve in the side-band region, as shown by the blue sections in Figure 7.30. From the relation (7.5), the estimation of background events in the signal region is $B_{\rm sig} = 63.21$ events.

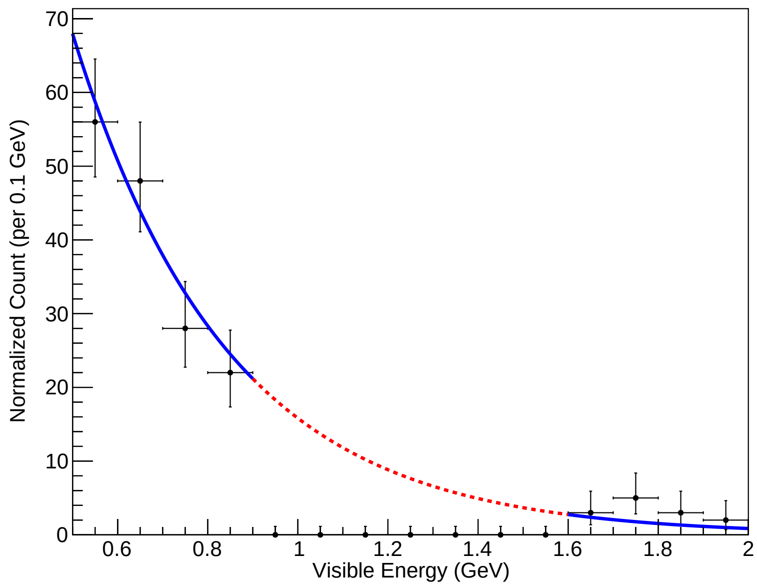

Figure 7.30: The side-band region is fitted with an exponential function. There are $B_{\text{sb}} = 167$ events in the side-band. Area under the fitting curve in side-band region is $x = 0.73$. From the fit, we can find $B_{\text{sig}} = 63.21$ events. We observed 63 events in the signal region.

After all the cuts are applied, we found 63 events in the signal region.

7.4 Systematic Uncertainties

Estimation of the systematic uncertainties is a crucial step of the analysis in the case we would like to claim a discovery. Due to the time constraint, this aspect, however, has not been analyzed in this study. In order to compute the sensitivity of the NOvA experiment to the neutron-antineutron oscillation, we project conservative guesses of the systematic errors on the signal efficiency, the background estimation and the exposure of the FD. This calculation will be explained in details in the next section.

7.5 Sensitivity Analysis

As a few important aspects of the search including a background model independent from the real data and the calculation of the systematic errors are not yet finalized, we decided not to open the box for this study. Instead we will present the sensitivity of the NOvA experiment to the neutron-antineutron oscillation.

7.5.1 Bayesian Approach for Sensitivity Estimation

Basically, this analysis is a counting experiment in which the expected number of observed events is given by

$$\mu = \Gamma\lambda\epsilon + b, \tag{7.6}$$

where Γ is the true event rate, λ is the true exposure ($\lambda = N\ T$, with N is the total number of bound neutrons in ^{12}C nuclei in the fiducial volume of the FD and T is the detector live time), ϵ is the true signal efficiency and lastly b is the true mean of background count. The probability of observing n candidate events is a Poisson distribution of mean μ:

$$P(n|\mu) = \frac{e^{-\mu}\mu^n}{n!} = \frac{e^{-(\Gamma\lambda\epsilon+b)}(\Gamma\lambda\epsilon + b)^n}{n!}. \tag{7.7}$$

Based on the Bayesian theorem, we have

$$P(\mu(\Gamma, \lambda, \epsilon, b)|n) \cdot P(n) = P(n|\mu(\Gamma, \lambda, \epsilon, b)) \cdot P(\mu(\Gamma, \lambda, \epsilon, b)). \tag{7.8}$$

For simplicity, we will assume that $\Gamma, \lambda, \epsilon$, and b are all independent. having this, we can write

$$P(\mu(\Gamma, \lambda, \epsilon, b)) = P(\Gamma) \cdot P(\lambda) \cdot P(\epsilon) \cdot P(b). \tag{7.9}$$

Treating $P(\Gamma|n)$ as a marginal distribution of $P(\mu(\Gamma, \lambda, \epsilon, b)|n)$, we can calculate the posterior of the true event rate by integral

$$\begin{aligned} P(\Gamma|n) &= \int P(\mu(\Gamma, \lambda, \epsilon, b)|n) \; \mathrm{d}\lambda \; \mathrm{d}\epsilon \; \mathrm{d}b, \\ &= A \int P(n|\mu(\Gamma, \lambda, \epsilon, b)) \cdot P(\mu(\Gamma, \lambda, \epsilon, b)) \; \mathrm{d}\lambda \; \mathrm{d}\epsilon \; \mathrm{d}b, \\ &= A \int \frac{e^{-(\Gamma\lambda\epsilon + b)}(\Gamma\lambda\epsilon + b)^n}{n!} P(\Gamma) \cdot P(\lambda) \cdot P(\epsilon) \cdot P(b) \; \mathrm{d}\lambda \; \mathrm{d}\epsilon \; \mathrm{d}b. \end{aligned} \tag{7.10}$$

A is a normalization constant ensuring $\int_0^\infty P(\Gamma|n) \; \mathrm{d}\Gamma = 1$. The probabilities $P(\Gamma), P(\lambda), P(\epsilon)$, and $P(b)$ will be marginalized out in the integration. The standard deviation of these priors will also allow the inclusion of the systematic effects into the calculation of the limit. For simplicity, we assume a Gaussian form for all these priors. In the unphysical regions of the parameters ϵ, λ and b, the priors are all set to 0.

$$P(\lambda) \propto \begin{cases} \exp\left[-\dfrac{(\lambda - \lambda_0)^2}{2\sigma_\lambda^2}\right] & \text{if } \lambda > 0, \\ 0 & \text{if } \lambda \le 0. \end{cases} \tag{7.11}$$

$$P(\epsilon) \propto \begin{cases} \exp\left[-\dfrac{(\epsilon - \epsilon_0)^2}{2\sigma_\epsilon^2}\right] & \text{if } 0 < \epsilon < 1, \\ 0 & \text{otherwise.} \end{cases} \tag{7.12}$$

$$P(b) \propto \ \exp\left[-\frac{(b-b_0)^2}{2\sigma_b^2}\right]. \tag{7.13}$$

In above equations, λ_0, ϵ_0 and b_0 are the estimated exposure, efficiency and background. The values of σ_λ, σ_ϵ and σ_b needs to be calculated by taking into account the systematic and statistical uncertainties. As mentioned in the previous section, we will use conservative guesses for the values of these errors.

The 90% confidence limit (C.L.) of the event rate $\Gamma_{90\%}$ can be found by solving the following equation

$$\int_0^{\Gamma_{90\%}} P(\Gamma|n)\ \mathrm{d}\Gamma = 0.9. \tag{7.14}$$

Once the limit of the event rate is found, the limit of the oscillation lifetime is simply the inversion of the limit of the rate.

7.5.2 Estimation of Bound Neutron Oscillation Lifetime

The NOvA's FD is 14 kton with 66.66% of the mass comes from ^{12}C [139]. So there are about 3×10^{33} bound neutrons from those ^{12}C nuclei. As mentioned in Section 7.2.3, we assume 7 years of data blinded for the analysis. Using these two figures, the total exposure of the FD for the search is calculated to be about 2.1×10^{34} neutron·years. About the uncertainty of the exposure, we can assume a small error of 1% as the mass, the composition and the live time of the detector are all measured very precisely.

Also from Section 7.2.3, the overall signal efficiency has been estimated to be 11.5%. A significant error of 10% is assumed for the signal efficiency. As pointed out in Section 7.3, the data-driven background estimation agrees with the number of candidates in the signal region. This supports the assumption we made at the beginning of this chapter that all the events present in the unblinded data are background. It, in turn, allows us to project the number of background events in the 7 years of blinded data to be equal to the expected number of candidates of 1330, see Section 7.3. A large error of 30% is imposed on this value as we are trying to be conservative in our estimation of the sensitivity.

The figures that are needed to the sensitivity calculation are summarized in Table 7.2.

	λ (n.yrs)	ϵ	b
Mean Value	2.1 $\times 10^{34}$	11.5%	1330
Assumed Error (Percentage)	1%	10%	30%
Assumed Error	2.1 $\times 10^{32}$	1.2%	400

Table 7.2: Estimation of the parameters needed for the calculation of NOvA's sensitivity to the neutron-antineutron oscillation.

.

Substituting these values into the (7.14), the sensitivity calculation is now merely a matter of multi-dimensional integration. This integral is computed using a multi-dimensional integration tool called `Cubature` [140]. The computation results in a 90% C.L. of the true event rate of

$$\Gamma_{90\%} = 2.46 \times 10^{-31}\ (\text{year}^{-1}), \tag{7.15}$$

and a 90% C.L. bound neutron oscillation life-time of

$$T_{90\%} = \frac{1}{\Gamma_{90\%}} = 4 \times 10^{30}\ (\text{year}). \tag{7.16}$$

A cross-check is performed to make sure the validity of the calculation for the NOvA's sensitivity. In this cross-check, we ran the integration against the parameters of the Super-Kamiokande experiment's search for neutron-antineutron oscillation published in 2015 [2]. The Super-Kamiokande's detector exposure, signal efficiency and background estimation are summarized in Table 7.3.

	λ (n.yrs)	ϵ	b
Mean Value	2.45×10^{34}	12.1%	24.1
Syst. and Stat. Errors	7.35×10^{32}	2.8%	5.7

Table 7.3: The detector exposure, signal efficiency and background estimation obtained from the search for neutron-antineutron oscillation in the Super-Kamiokande experiment [2].

.

The integration results in the 90% C.L. limit on the event rate of $\Gamma_{90\%} = 5.31 \times 10^{-33}$ and the 90% C.L. limit on the bound neutron oscillation life time of

$$T_{90\%} = \frac{1}{\Gamma_{90\%}} = 1.88 \times 10^{32} \text{ years.}$$

The quotation for this value from the Super-Kamiokande paper is 1.9×10^{32} years [2].

7.5.3 Estimation of Free Neutron Oscillation Lifetime

As explained in Section 2.3, the limit on the oscillation life time T for bound neutrons can be translated to a limit on that of free neutrons providing that the nuclear suppression factor R of the target nucleus is known. Currently, the nuclear suppression factor for ^{12}C is not available. Both theoretical computation or experimental measurement of this figure lie beyond the scope of this work at the moment. In order to make an estimation of free neutron oscillation life time, we make an educated guess about the value of R for ^{12}C target.

The assumption we make here is that R is linearly scale with the number of baryons inside a nucleus. This guess comes from the observation of the nuclear suppression factor estimated for various target nuclei, see Table 7.4.

Nucleus	Nuclear Suppression Factor
^{56}Fe	$1.1 \times 10^{23}\,\mathrm{s}^{-1}$ [141]
^{56}Fe	$0.7 \times 10^{23}\,\mathrm{s}^{-1}$ [31]
^{40}Ar	$0.7 \times 10^{23}\,\mathrm{s}^{-1}$ [116]
^{16}O	$1.2 \times 10^{23}\,\mathrm{s}^{-1}$ [141]
^{16}O	$0.8 \times 10^{23}\,\mathrm{s}^{-1}$ [31]
^{12}C	$0.53 \times 10^{23}\,\mathrm{s}^{-1}$ (estimated)
^{2}H	$2.3 \times 10^{22}\,\mathrm{s}^{-1}$ [61]

Table 7.4: Nuclear suppression factors for various nuclei.

For $A = 12$, the nuclear suppression factor for ^{12}C is estimated to be $R = 0.53 \times 10^{23}\,\mathrm{s}^{-1}$. Via Equation (2.9) and the result in (7.16), the 90% C.L. limit on the oscillation lifetime for free neutrons is found to be

$$\tau_{90\%} = \sqrt{\frac{T_{90\%}}{R}} = 0.6 \times 10^{8} \text{ (s)}. \tag{7.17}$$

This result (7.16) shows that, to the first order, our analysis is going in the right direction. However, compared to the limits set by past experiment shown in Table 2.1, it is clear that many aspects of the analysis need to be improved if we want to achieve a higher level of competitiveness.

Chapter 8

Result and Future Work

This thesis has demonstrated the potential of the NOvA experiment regarding the search for neutron-antineutron oscillation.

A trigger system is developed to collect the signal-like events in the FD. After a successful deployment, this system has been operating smoothly for almost two years, providing a large dataset not only critical for the neutron oscillation search but also useful for a variety of analyses involving exotic physics phenomena.

Beyond data acquisition, an offline analysis framework is developed for this work. It includes event reconstruction, background modeling, and signal selection. Applying this framework on four months of data (09/2018 - 12/2018) allows us to probe the sensitivity of the NOvA experiment to the search of the neutron-antineutron oscillation. A limit of 4×10^{30} (year) on the oscillation lifetime of bound neutrons in ^{12}C is set. With a guess of the nuclear suppression factor of ^{12}C nucleus, this translates to a limit of 0.6×10^{8} (s) on the oscillation lifetime of free neutrons.

For future work, several aspects of the analysis require improvements or complete rework.

First, the background model based on the simulation of the atmospheric neutrinos and cosmogenic neutrons will finalize. It will be validated against the cosmic data that is collected by a difference trigger stream. The validation makes sure the rates and shape distributions of cosmic particles are corrected. Being independent of the real data, this background model eliminates the need for a partially unblinded dataset, thus improves the statistics in the final result. With the ability to predict the rate and shape of the background precisely, the model enables us to claim discovery if we see a significant excess of events in the signal region after unblinding the data.

Second, the calculation of systematic uncertainties is required to provide a robust analysis result. Sources of errors affecting the signal efficiency, background estimation, and detector exposure all need to be identified. When an excess occurs in the signal region, a figure of error is a must to quantify its statistical significance.

Third, the event reconstruction will require new techniques to identify the prongs of final state particles. A simple prong count can significantly improve the efficiency of the event selection and help cut down many background events. This task might benefit from recent developments in prong identification in NOvA.

Lastly, a reliable computation of the nuclear suppression factor is needed. As this lies beyond the scope of experimental work, exchanges with experts in the corresponding field are required.

Appendices

Appendix A

Neutron-Antineutron Event Displays

Displays of neutron-antineutron oscillation events simulated based on the branching ratio shown in Table 4.1.

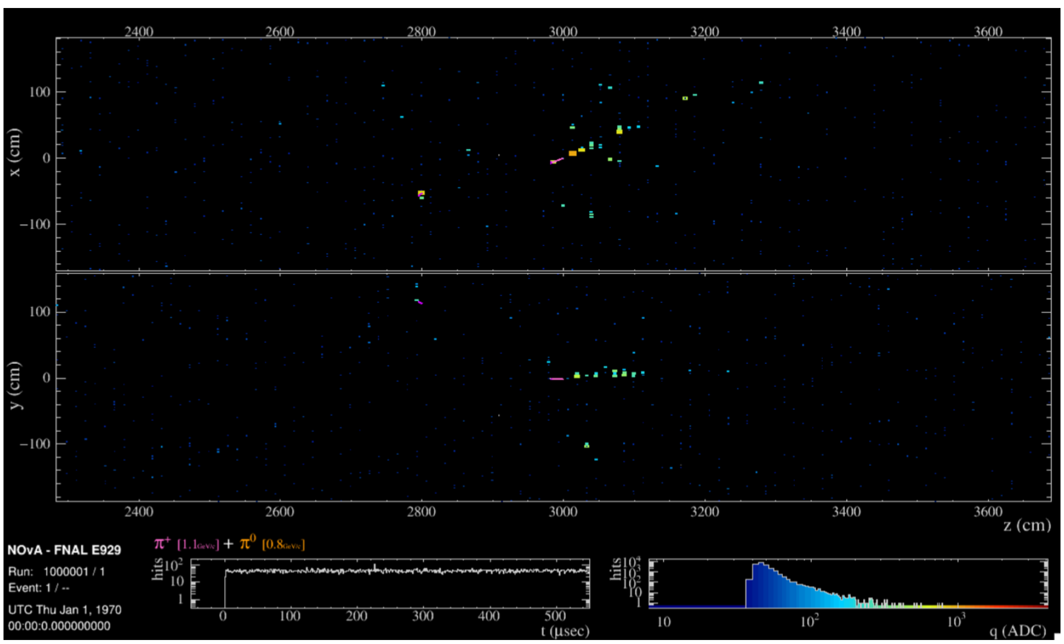

Figure A.1: Display of a $p + \bar{n} \rightarrow \pi^{+} + \pi^{0}$ simulated event.

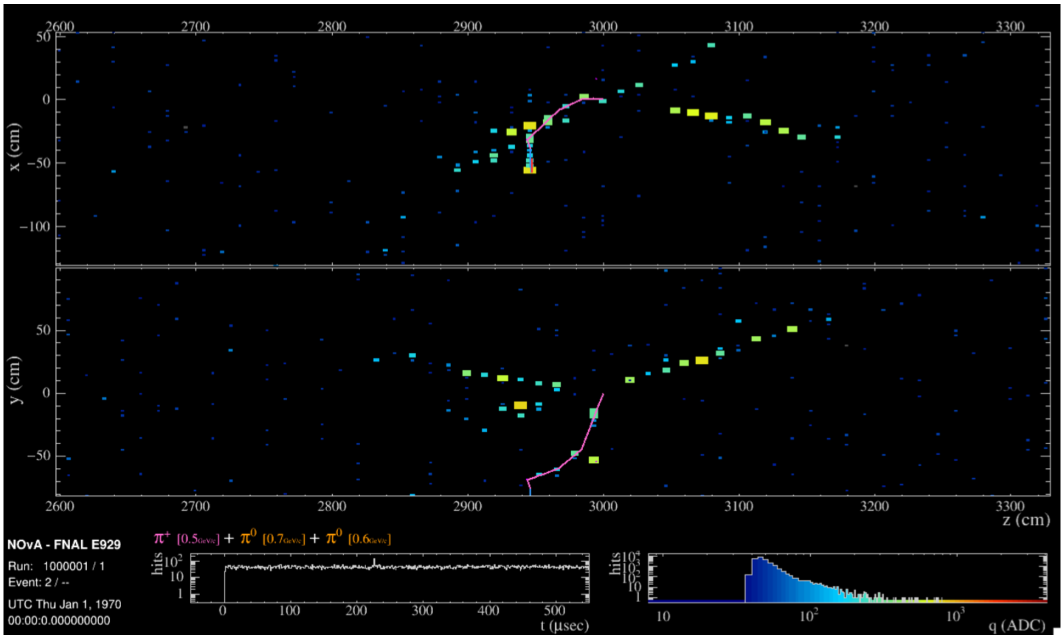

Figure A.2: Display of a $p + \bar{n} \rightarrow \pi^+ + 2\pi^0$ simulated event.

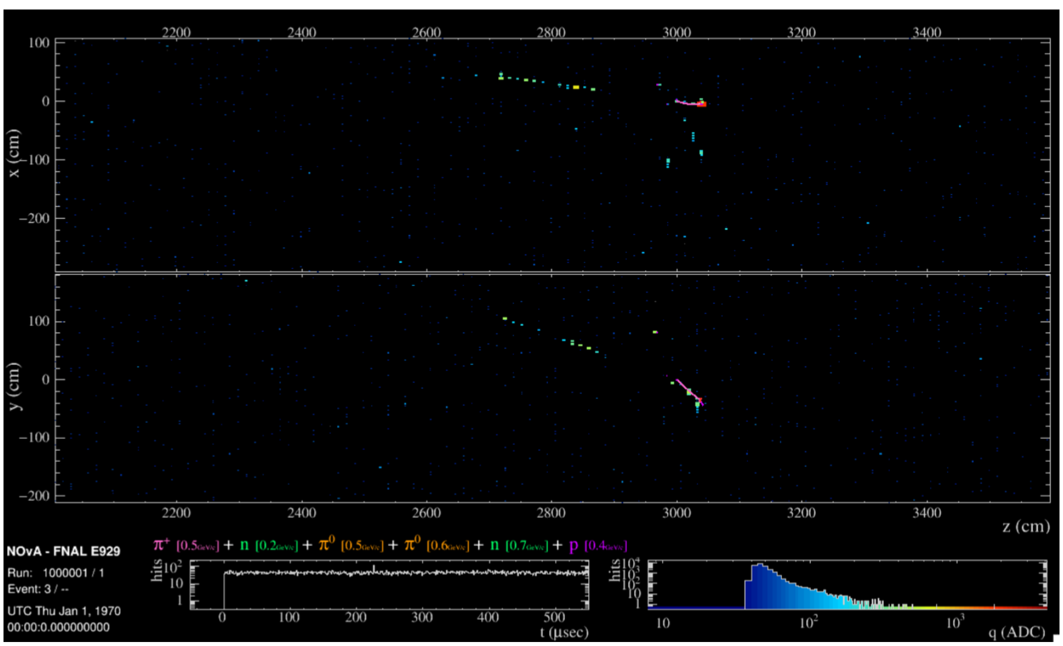

Figure A.3: Display of a $p + \bar{n} \rightarrow \pi^+ + 3\pi^0$ simulated event.

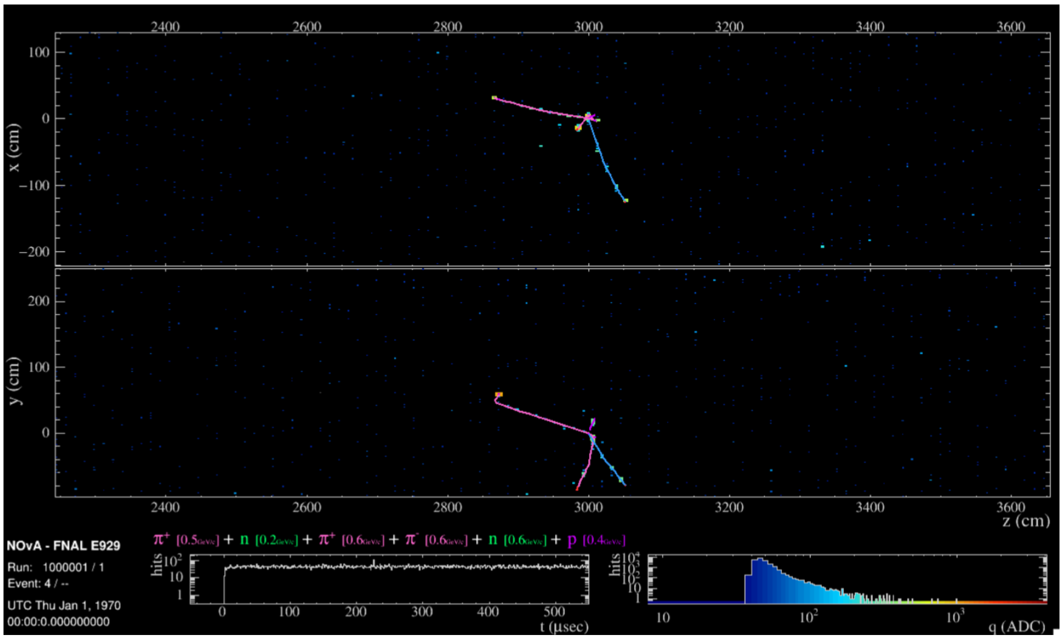

Figure A.4: Display of a $p + \bar{n} \rightarrow 2\pi^+ + \pi^- + \pi^0$ simulated event.

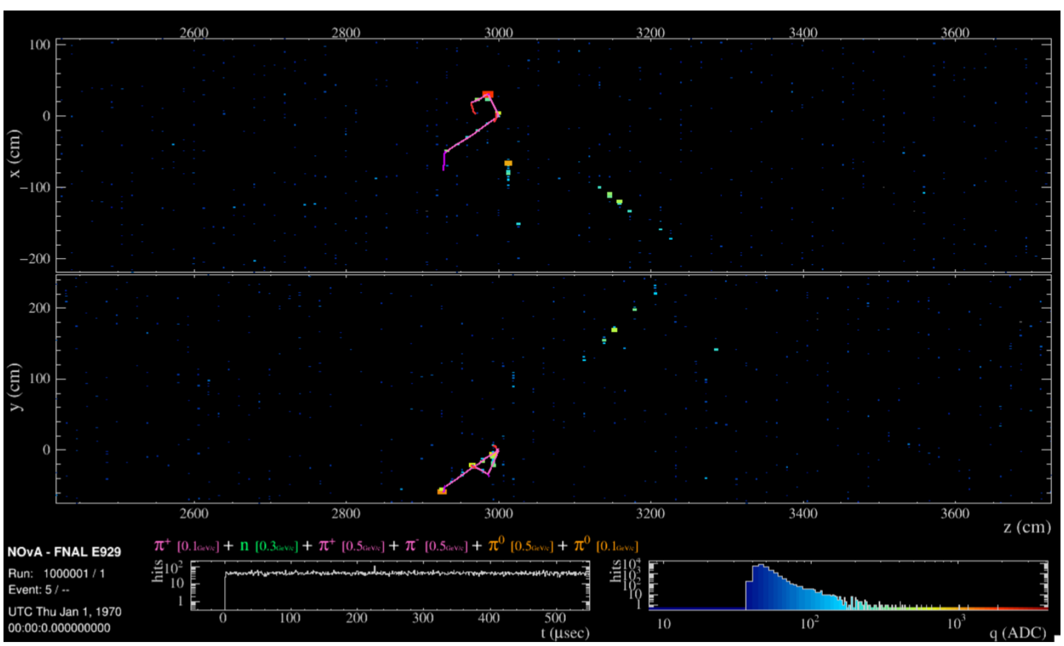

Figure A.5: Display of a $p + \bar{n} \rightarrow 2\pi^+ + \pi^- + 2\pi^0$ simulated event.

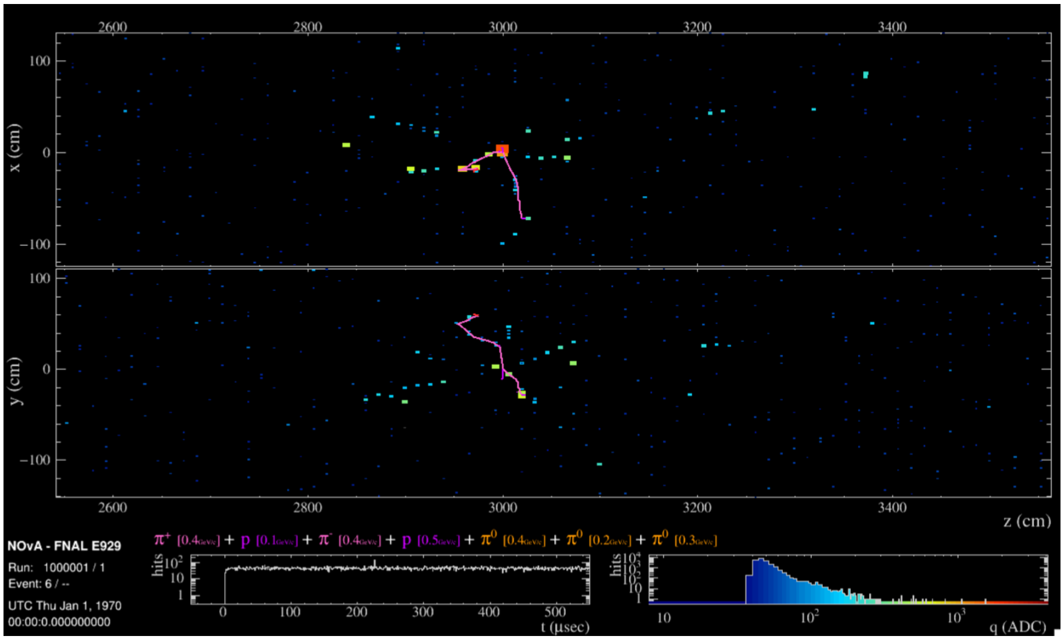

Figure A.6: Display of a $p + \bar{n} \to 2\pi^+ + \pi^- + 2\omega^0$ simulated event.

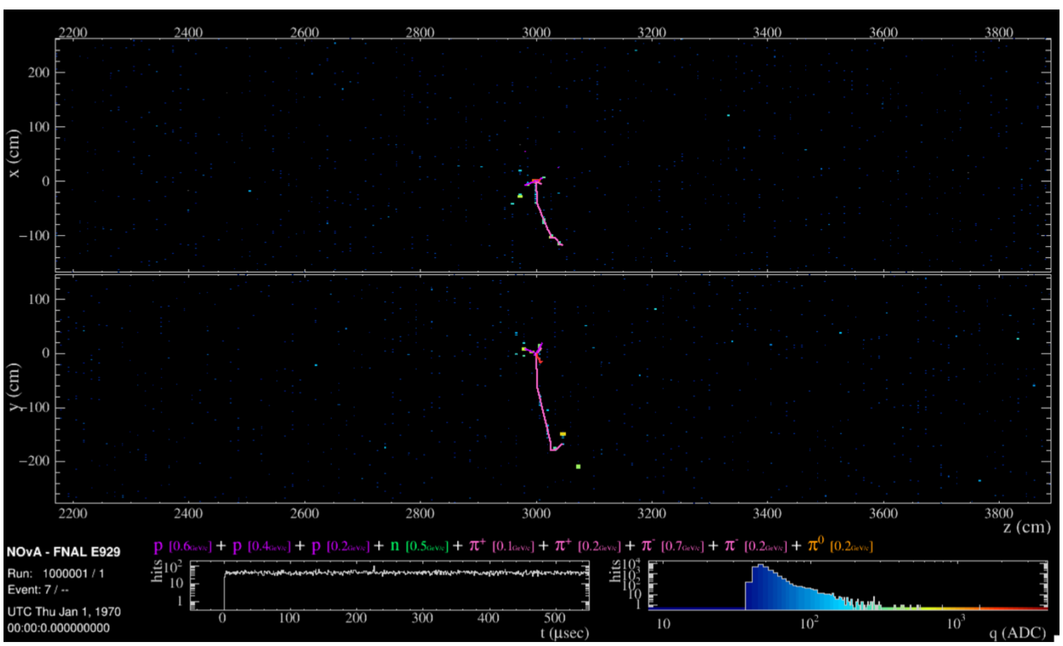

Figure A.7: Display of a $p + \bar{n} \to 3\pi^+ + 2\pi^- + \pi^0$ simulated event.

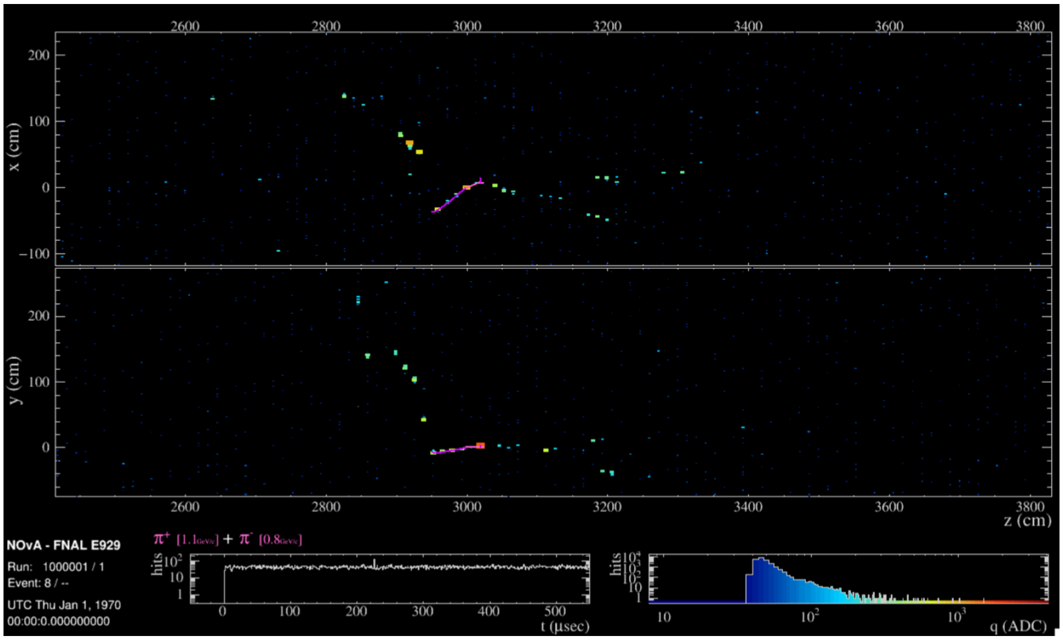

Figure A.8: Display of a $n + \bar{n} \rightarrow \pi^+ + \pi^-$ simulated event.

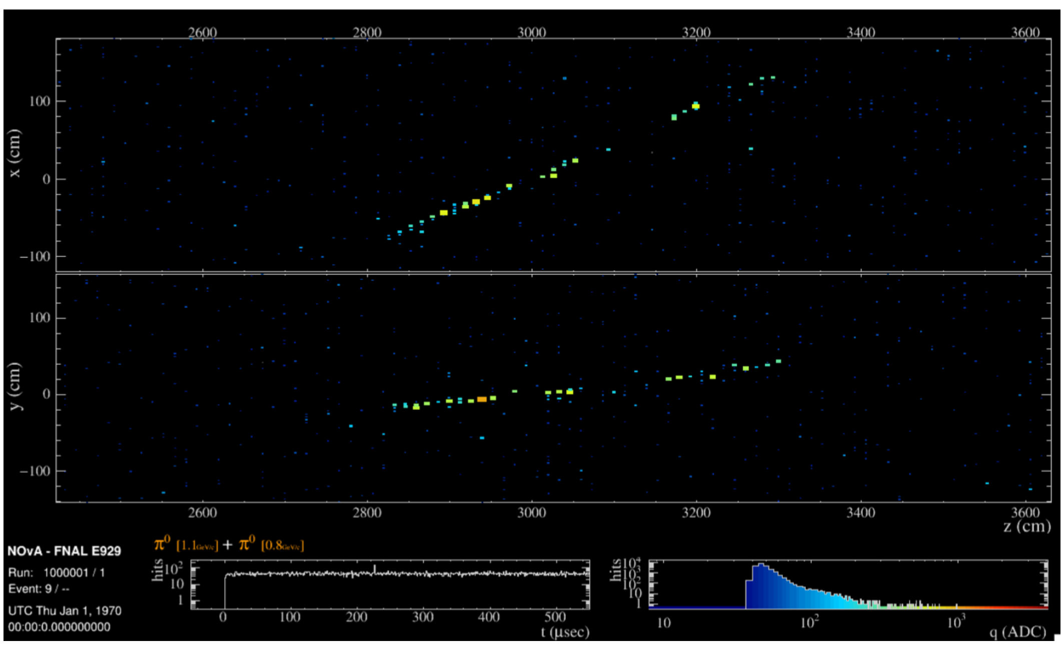

Figure A.9: Display of a $n + \bar{n} \rightarrow 2\pi^0$ simulated event.

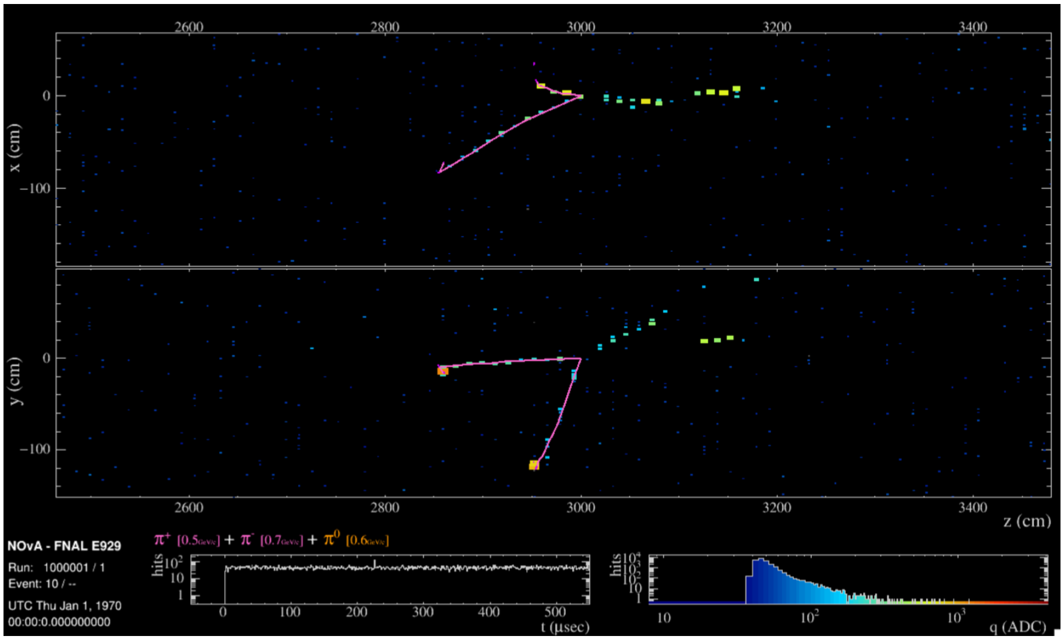

Figure A.10: Display of a $n + \bar{n} \to \pi^+ + \pi^- + \pi^0$ simulated event.

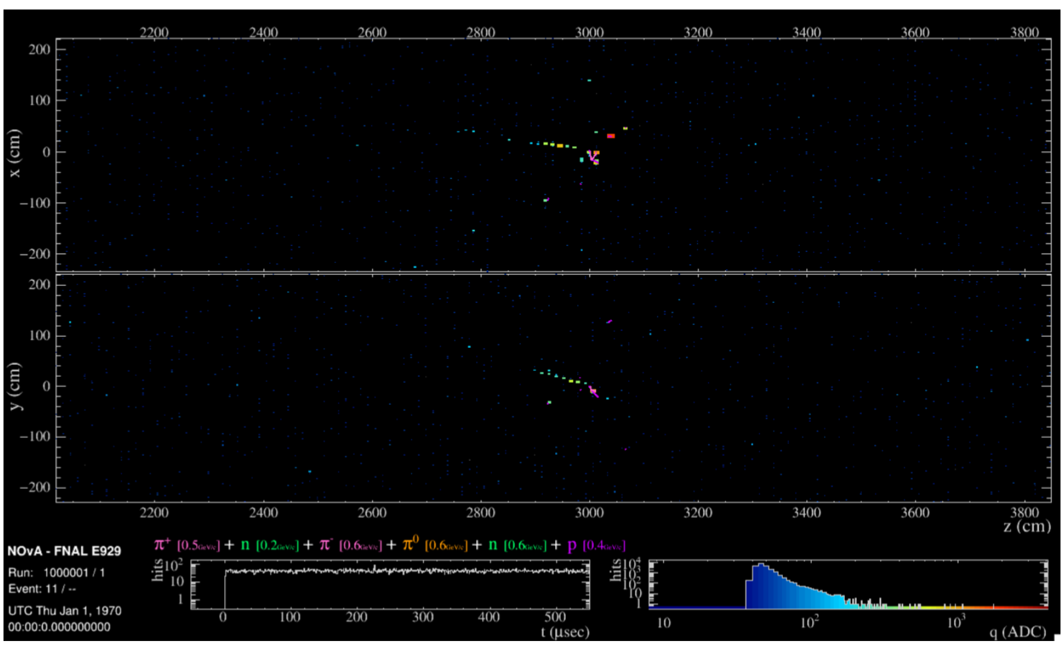

Figure A.11: Display of a $n + \bar{n} \to \pi^+ + \pi^- + 2\pi^0$ simulated event.

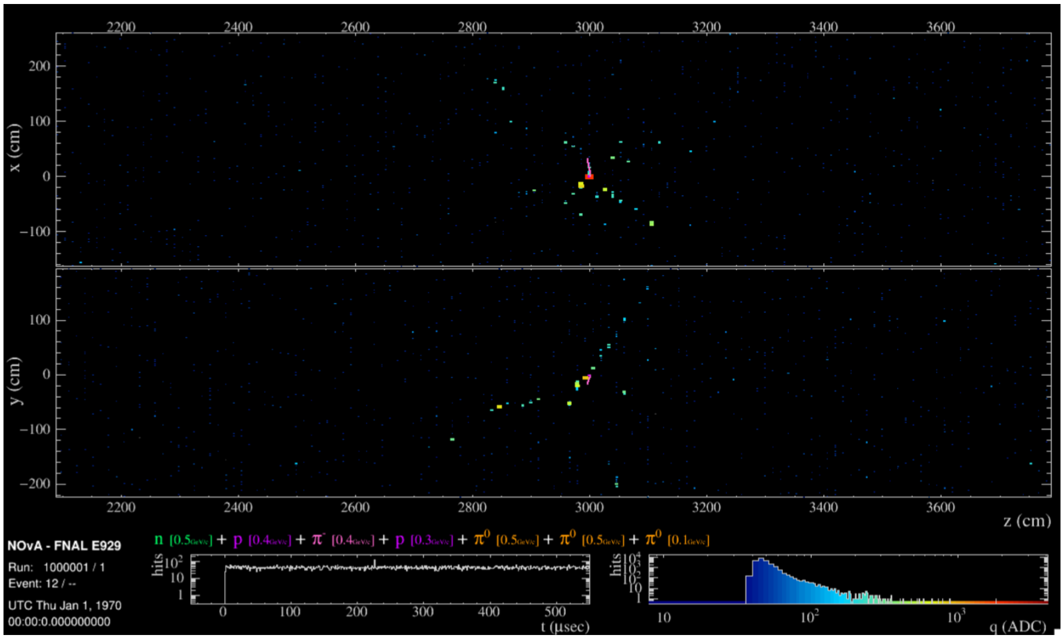

Figure A.12: Display of a $n + \bar{n} \to \pi^+ + \pi^- + 3\pi^0$ simulated event.

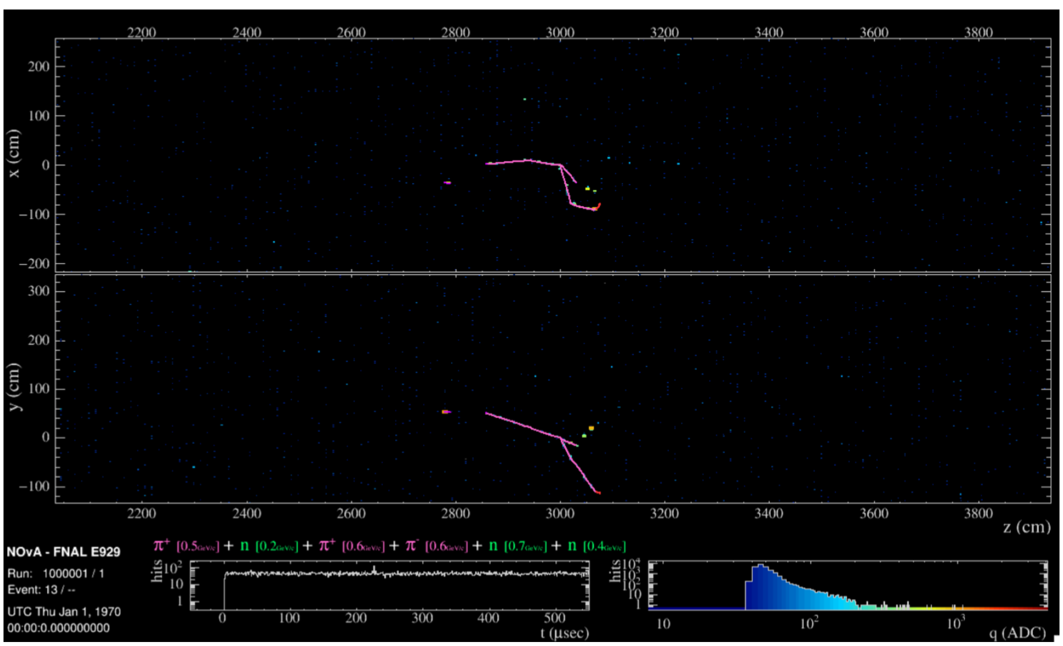

Figure A.13: Display of a $n + \bar{n} \to 2\pi^+ + 2\pi^-$ simulated event.

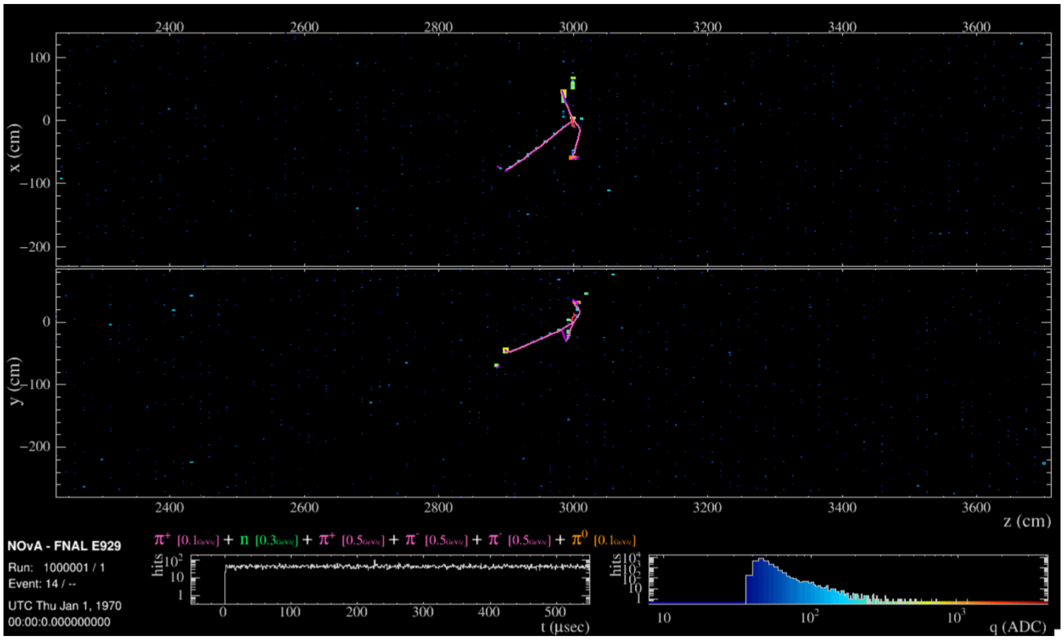

Figure A.14: Display of a $n + \bar{n} \rightarrow 2\pi^{+} + 2\pi^{-} + \pi^{0}$ simulated event.

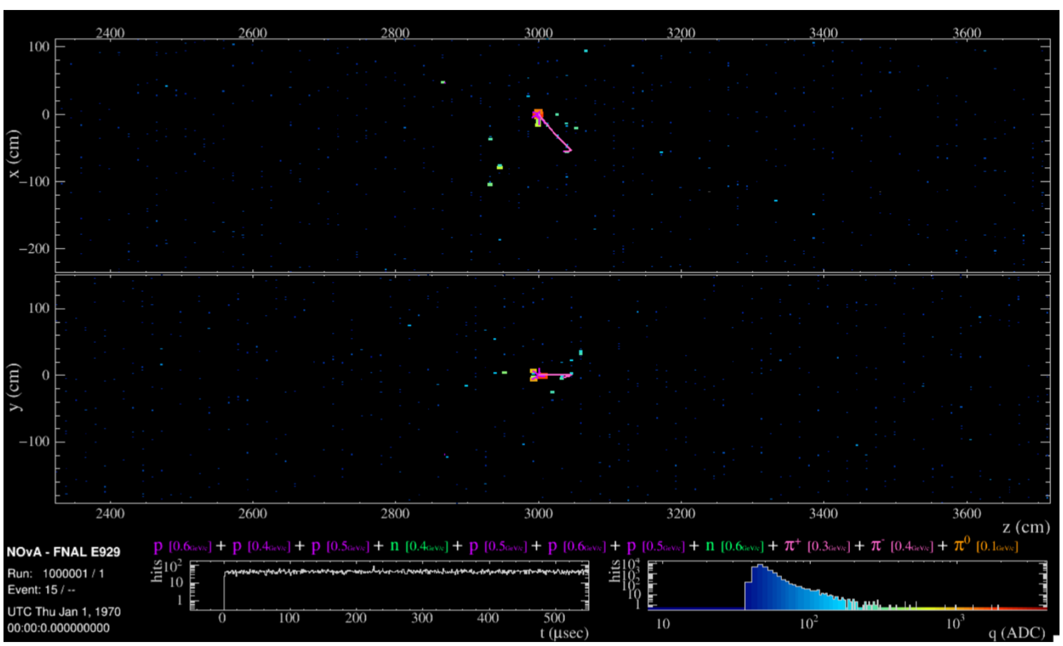

Figure A.15: Display of a $n + \bar{n} \rightarrow \pi^{+} + \pi^{-} + \omega^{0}$ simulated event.

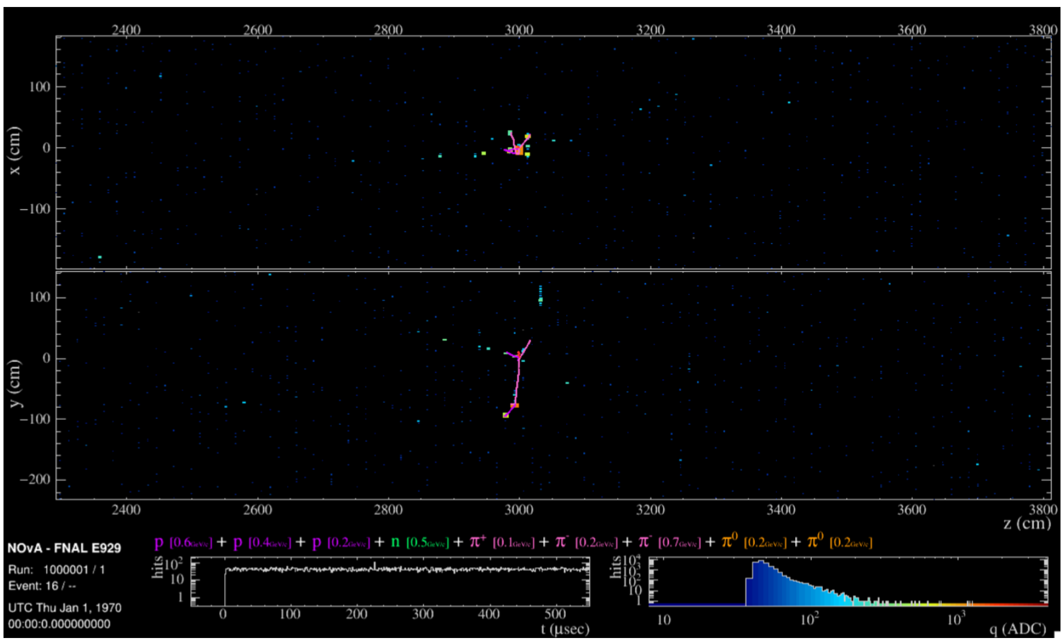

Figure A.16: Display of a $n + \bar{n} \rightarrow 2\pi^{+} + 2\pi^{-} + 2\omega^{0}$ simulated event.

Appendix B

Neutron-Antineutron Transition Probability

In Section 2.3, we see that the Schrodinger's equation for the $n - \bar{n}$ system can be written as

$$i\frac{\partial}{\partial t}\begin{pmatrix} n \\ \bar{n} \end{pmatrix} = \begin{pmatrix} E_n & \delta m \\ \delta m & E_{\bar{n}} \end{pmatrix}\begin{pmatrix} n \\ \bar{n} \end{pmatrix} \equiv A\begin{pmatrix} n \\ \bar{n} \end{pmatrix}. \tag{B.1}$$

The formal solution of this equation is

$$\begin{pmatrix} n \\ \bar{n} \end{pmatrix}_t = \mathrm{e}^{-\mathrm{i}At}\begin{pmatrix} n \\ \bar{n} \end{pmatrix}_{t=0}, \tag{B.2}$$

where $\mathrm{e}^{-\mathrm{i}At}$ is a 2×2 matrix. If the system starts as n, i.e. $(1, 0)$ the probability of being detected as $\bar{n}$, i.e. $(0, 1)$, is

$$P_{\bar{n}}(t) = \left|\begin{pmatrix} 0 & 1 \end{pmatrix}\mathrm{e}^{-\mathrm{i}At}\begin{pmatrix} 1 \\ 0 \end{pmatrix}\right|^2. \tag{B.3}$$

The time-evolution matrix $\mathrm{e}^{-\mathrm{i}At}$ can be computed via its series expansion

$$\mathrm{e}^{-\mathrm{i}At} = 1 + \frac{-\mathrm{i}At}{1!} + \frac{(-\mathrm{i}At)^2}{2!} + \frac{(-\mathrm{i}At)^3}{3!} + \cdots \tag{B.4}$$

To compute the exact expression, A can be written as [142]

$$A = \begin{pmatrix} E_n & \delta m \\ \delta m & E_n \end{pmatrix} = \frac{1}{2}\left(2\delta m \cdot \sigma_x + \Delta E \cdot \sigma_z\right) + \frac{1}{2}\left(E_n + E_{\bar{n}}\right) \cdot I, \tag{B.5}$$

where σ_x and σ_z are Pauli matrices

$$\sigma_x = \begin{pmatrix} 0 & 1 \\ 1 & 0 \end{pmatrix}, \sigma_z = \begin{pmatrix} 1 & 0 \\ 0 & -1 \end{pmatrix} \tag{B.6}$$

which satisfy $\sigma_x^2 = \sigma_x^2 = I$, and $\Delta E = E_n - E_{\bar{n}}$. Thanks to this decomposition, now we have

$$\mathrm{e}^{-\mathrm{i}At} = \mathrm{e}^{-\frac{\mathrm{i}t}{2}(E_n+E_{\bar{n}})\cdot I} \cdot \mathrm{e}^{-\frac{\mathrm{i}t}{2}(2\delta m\cdot\sigma_x+\Delta E\cdot\sigma_z)}. \tag{B.7}$$

The first factor only provides a phase shift

$$\mathrm{e}^{-\frac{\mathrm{i}t}{2}(E_n+E_{\bar{n}})\cdot I} = \mathrm{e}^{-\frac{\mathrm{i}t}{2}(E_n+E_{\bar{n}})} \cdot I, \tag{B.8}$$

which would disappear when the absolute value is taken.

To expand the second term, we need to rely on the following property of the Pauli's matrices

$$(a\cdot\sigma_x + b\cdot\sigma_z)^n = \begin{cases} \gamma^n \cdot I & \text{for even } n, \\ \gamma^n \cdot \left(\dfrac{a\cdot\sigma_x + b\cdot\sigma_z}{\gamma}\right) & \text{for odd } n, \end{cases} \tag{B.9}$$

in which $\gamma = \sqrt{a^2+b^2}$. Apply these identities to our case with $a = 2\delta m$ and $b = \Delta E$, the expansion can then be reduced to

$$\begin{aligned}
&\mathrm{e}^{-\frac{\mathrm{i}t}{2}(2\delta m\cdot\sigma_x+\Delta E\cdot\sigma_z)} = \\
&I \cdot \left[1 - \frac{(\gamma t/2)^2}{2!} + \frac{(\gamma t/2)^4}{4!} - \cdots\right] \\
&- \mathrm{i}\left(\frac{2\delta m\cdot\sigma_x + \Delta E\cdot\sigma_z}{\gamma}\right)\cdot\left[\frac{(\gamma t/2)}{1!} - \frac{(\gamma t/2)^3}{3!} + \cdots\right] \\
&= \cos\frac{\gamma t}{2}\cdot I - i\sin\frac{\gamma t}{2}\cdot\left(\frac{2\delta m\cdot\sigma_x + \Delta E\cdot\sigma_z}{\gamma}\right).
\end{aligned} \tag{B.10}$$

The probability of a neutron oscillating to an antineutron given by

$$
\begin{aligned}
P_{\bar{n}}(t) &= \left|\langle\bar{n}|\mathrm{e}^{-\mathrm{i}At}|n\rangle\right|^2 \\
&= \left|\begin{pmatrix} 0 & 1 \end{pmatrix}\begin{pmatrix} \cos\left(\frac{\gamma t}{2}\right) - i\frac{\Delta E}{\gamma}\sin\left(\frac{\gamma t}{2}\right) & -i\frac{2\delta m}{\gamma}\sin\left(\frac{\gamma t}{2}\right) \\ -i\frac{2\delta m}{\gamma}\sin\left(\frac{\gamma t}{2}\right) & \cos\left(\frac{\gamma t}{2}\right) + i\frac{\Delta E}{\gamma}\sin\left(\frac{\gamma t}{2}\right) \end{pmatrix}\begin{pmatrix} 1 \\ 0 \end{pmatrix}\right|^2 \\
&= \frac{4\delta m^2}{\gamma^2}\sin^2\left(\frac{\gamma t}{2}\right) \\
&= \frac{4\delta m^2}{4\delta m^2 + \Delta E^2}\sin^2\left(\frac{\sqrt{4\delta m^2 + \Delta E^2}}{2}t\right).
\end{aligned}
\tag{B.11}
$$

Appendix C

BGLRS Flux Model

The BGLRS model [129] describes the flux of atmospheric neutrinos (including ν_e, $\bar{\nu}_e$, ν_μ and $\bar{\nu}_\mu$) at specific experiment sites. Shown in the following spectrum plots are the fluxes computed for the Kamioka observatory (orange), the SNO lab (cyan) and the Soudan mine (pink). The fluxes in the form of $\mathrm{d}N/\mathrm{d}(\log E)$ (in units of $\mathrm{m}^{-2}\times\mathrm{steradian}^{-1}\times\mathrm{s}^{-1}$) are calculated as functions of the azimuth and zenith angles. The azimuthal dependence and the zenith dependence of the fluxes are plots separately below. The effects of solar activity on the fluxes are also taken into account in the flux calculation in [129].

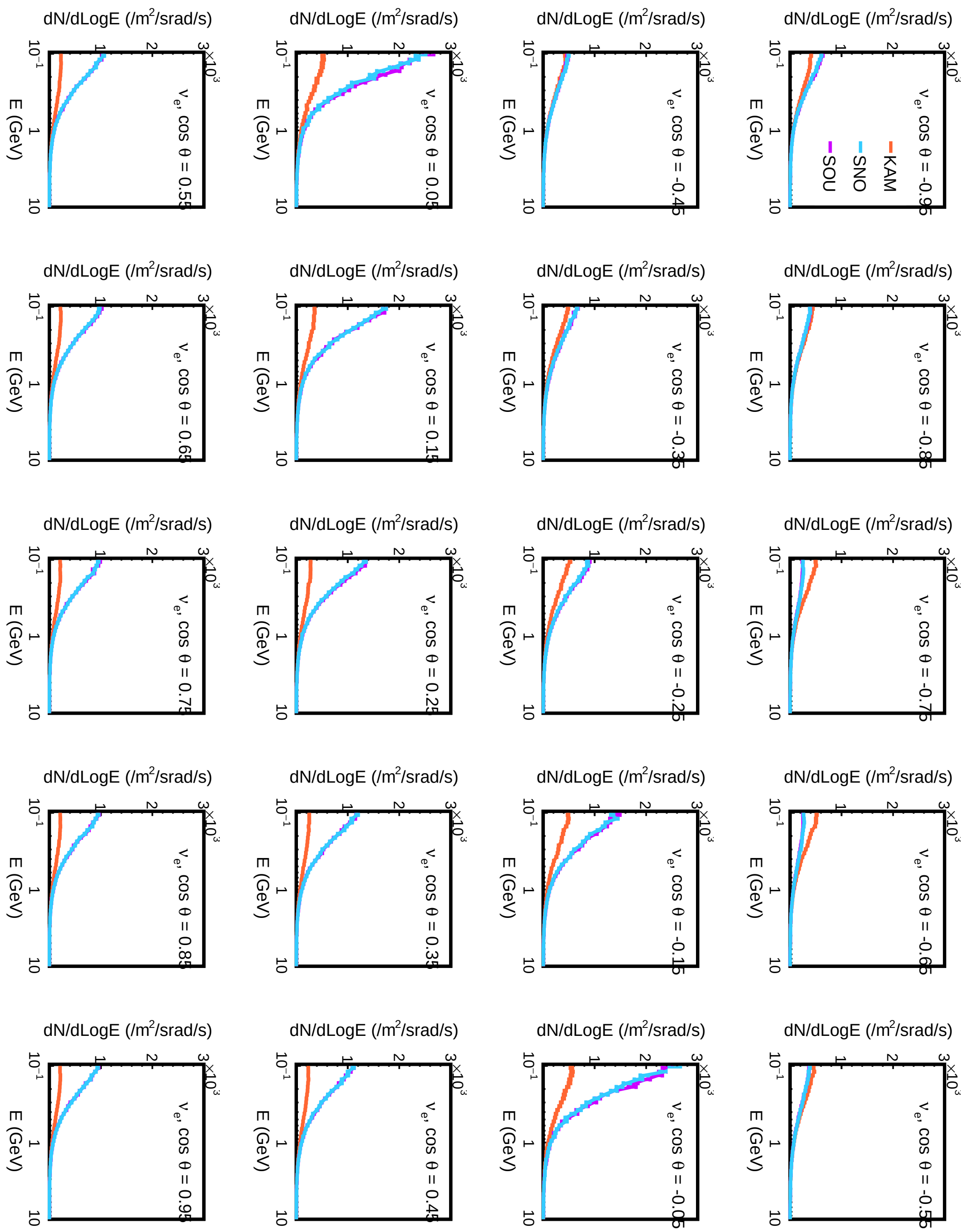

Figure C.1: Electron neutrino flux during the minimum of solar activity cycle as a function of the zenith angle.

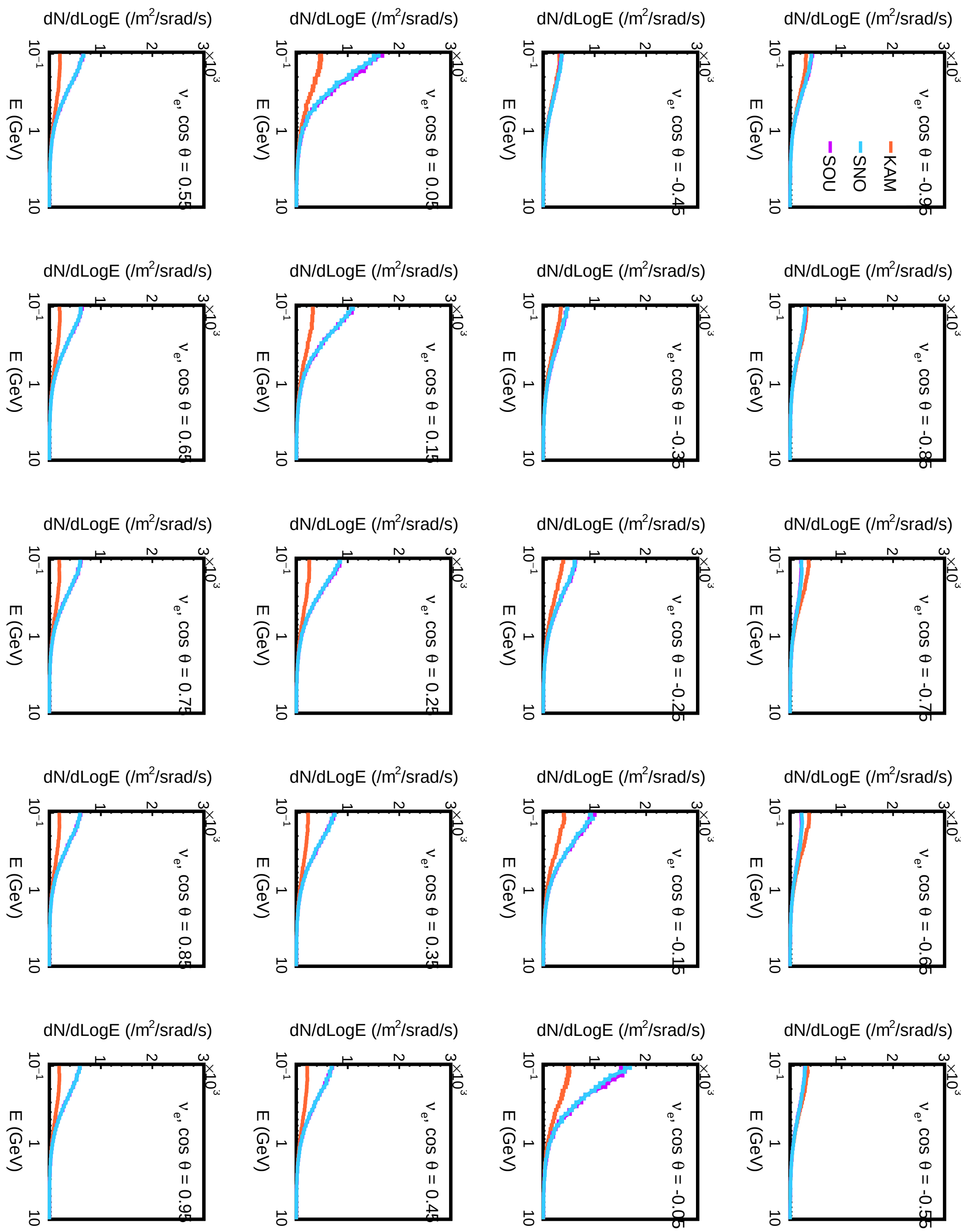

Figure C.2: Electron neutrino flux during the maximum of solar activity cycle as a function of the zenith angle.

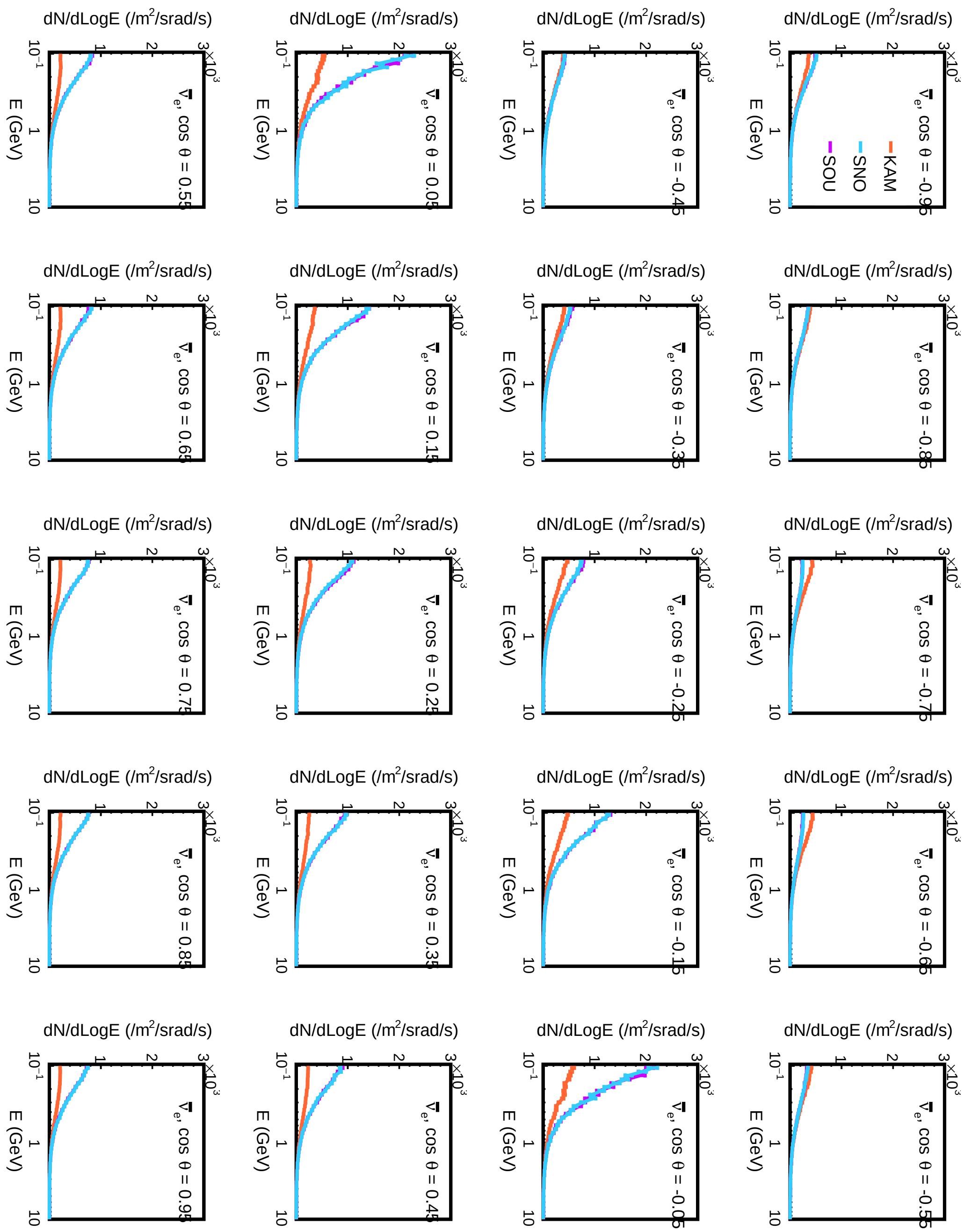

Figure C.3: Electron antineutrino flux during the minimum of solar activity cycle as a function of the zenith angle.

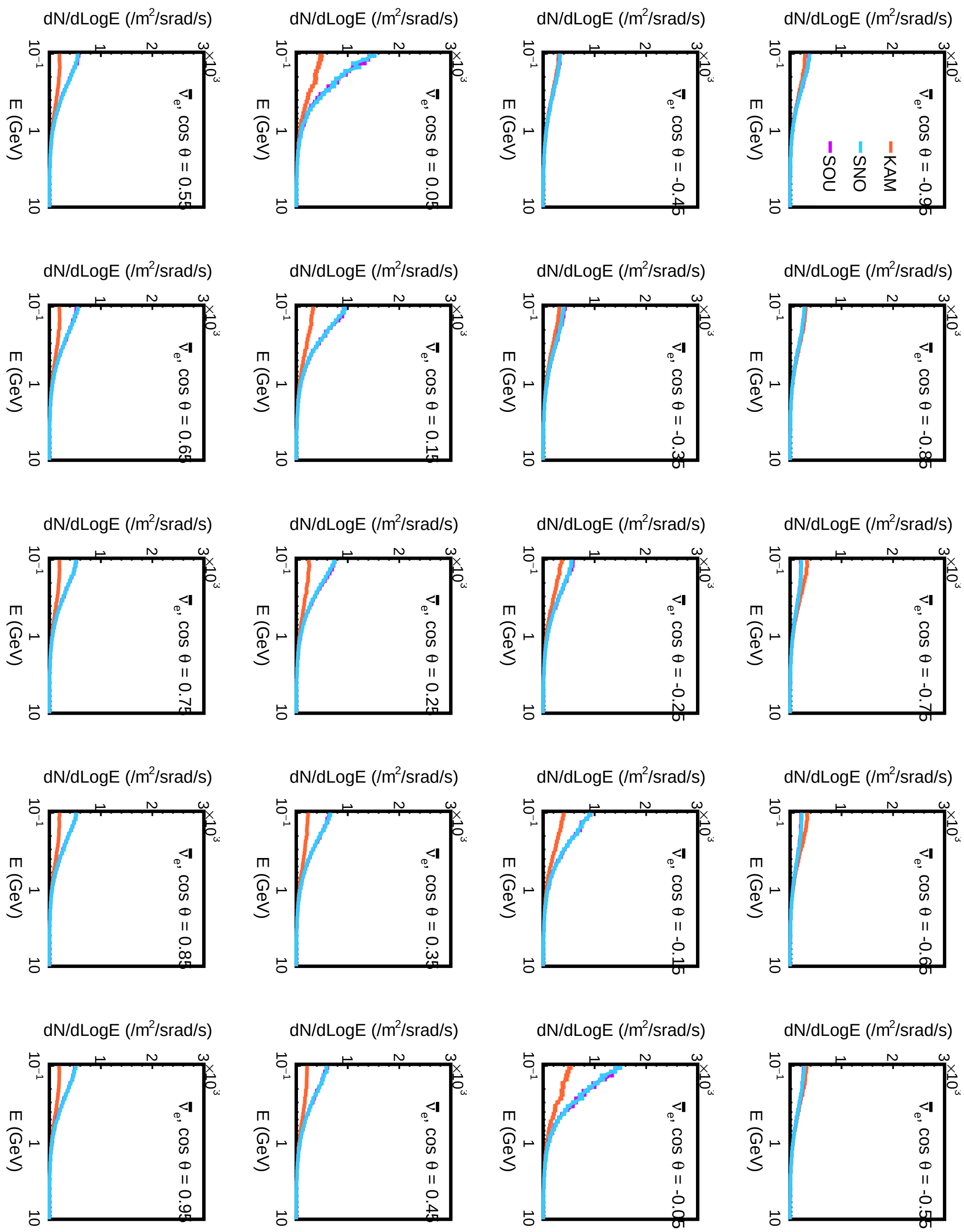

Figure C.4: Electron antineutrino flux during the maximum of solar activity cycle as a function of the zenith angle.

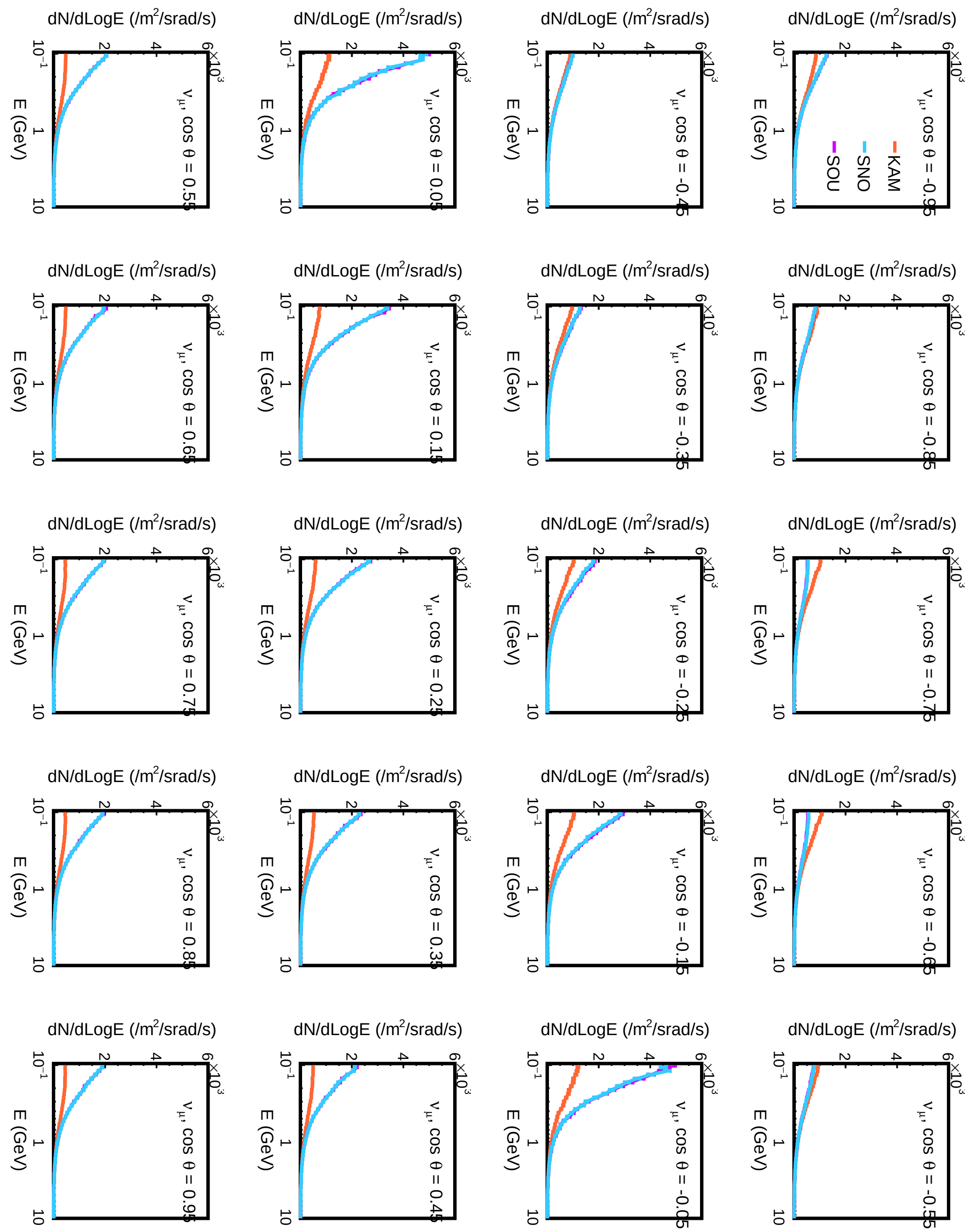

Figure C.5: Muon neutrino flux during the minimum of solar activity cycle as a function of the zenith angle.

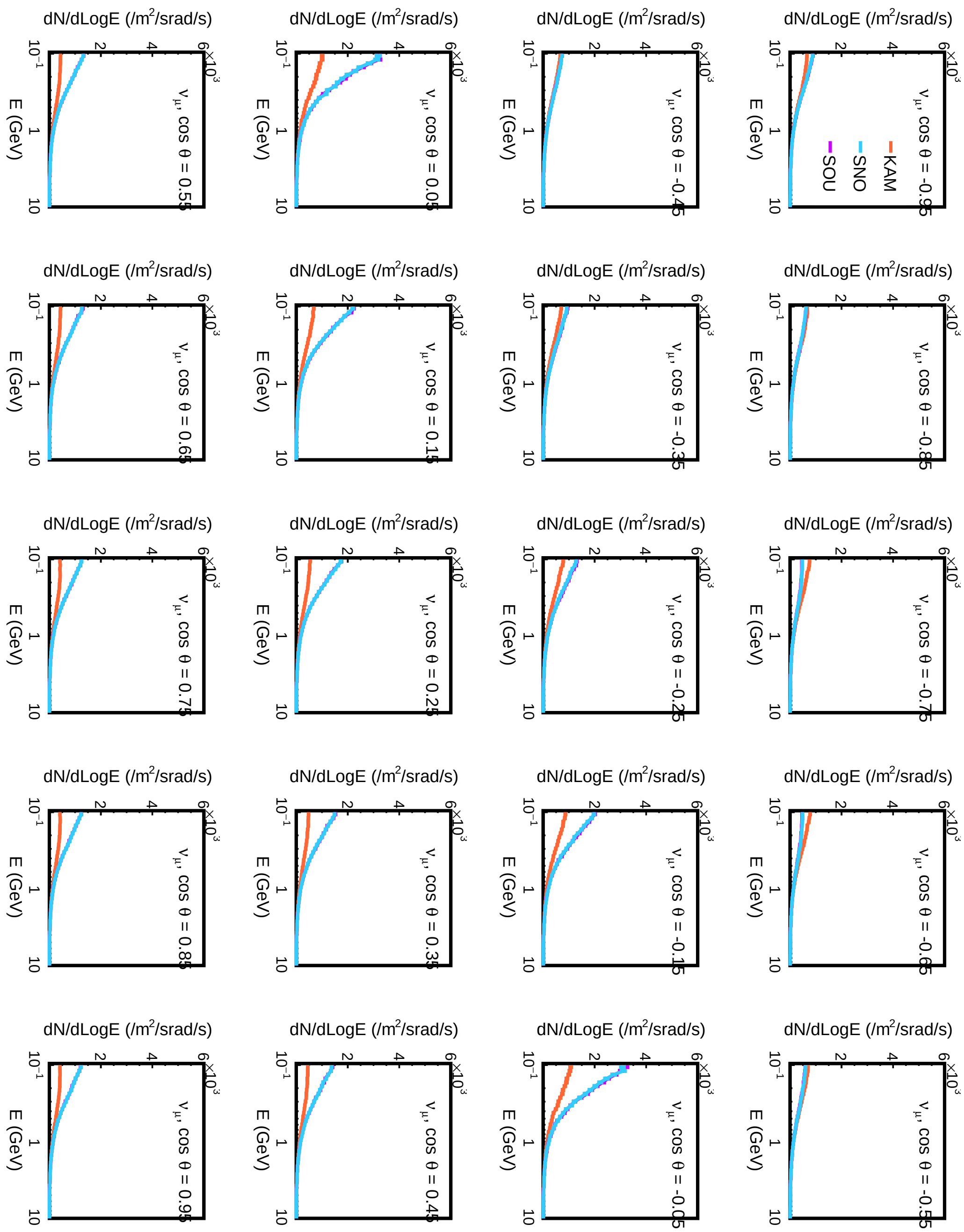

Figure C.6: Muon neutrino flux during the maximum of solar activity cycle as a function of the zenith angle.

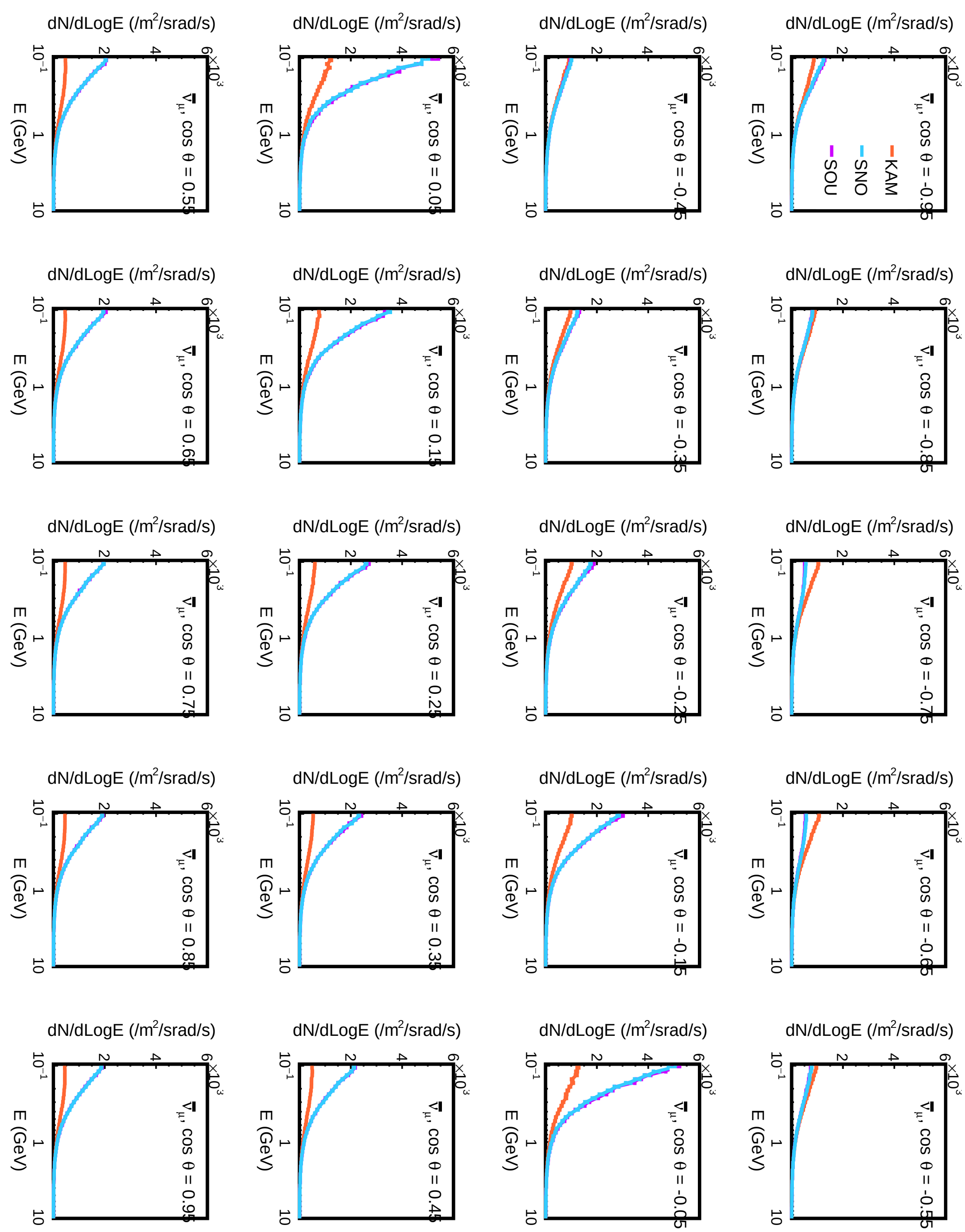

Figure C.7: Muon antineutrino flux during the minimum of solar activity cycle as a function of the zenith angle.

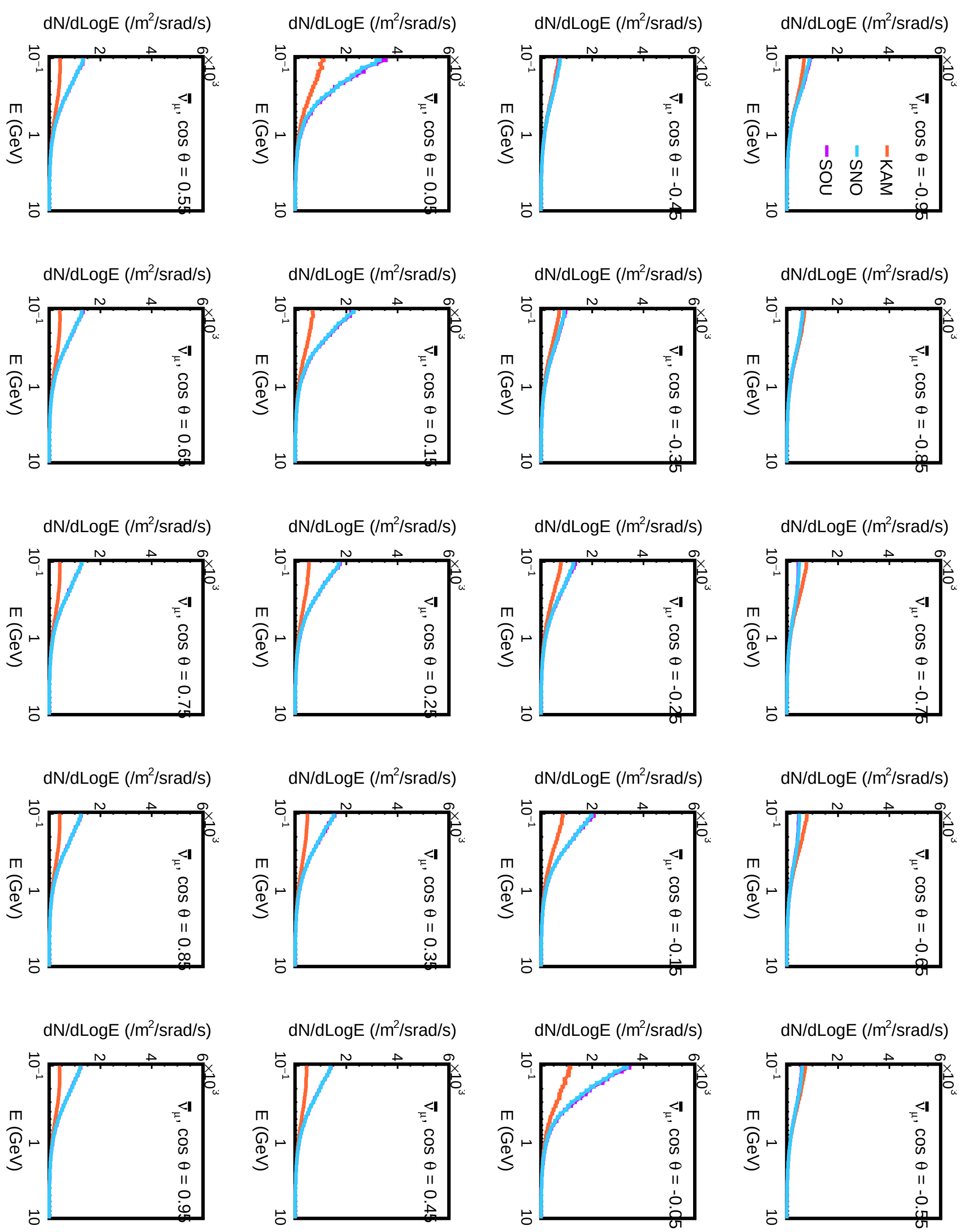

Figure C.8: Muon antineutrino flux during the maximum of solar activity cycle as a function of the zenith angle.

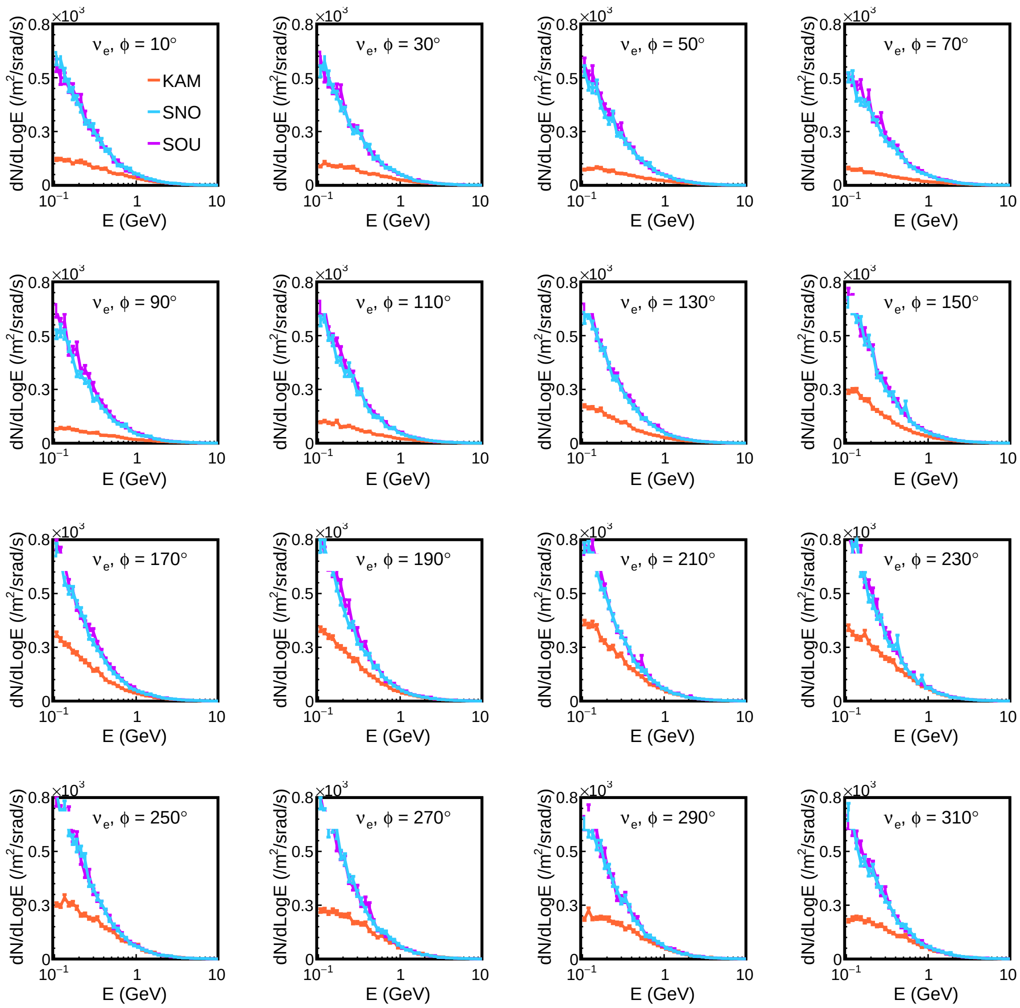

Figure C.9: Electron neutrino flux during the minimum of solar activity cycle as a function of the azimuth angle.

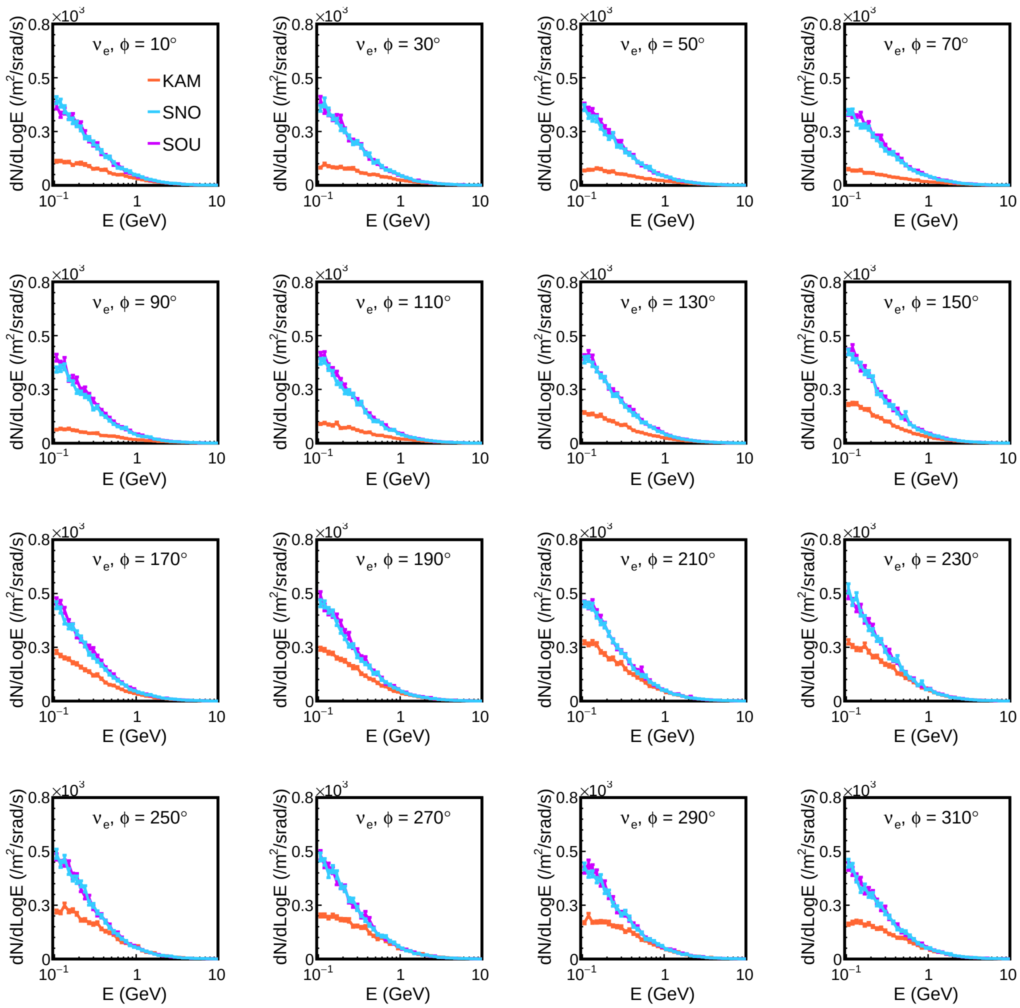

Figure C.10: Electron neutrino flux during the maximum of solar activity cycle as a function of the azimuth angle.

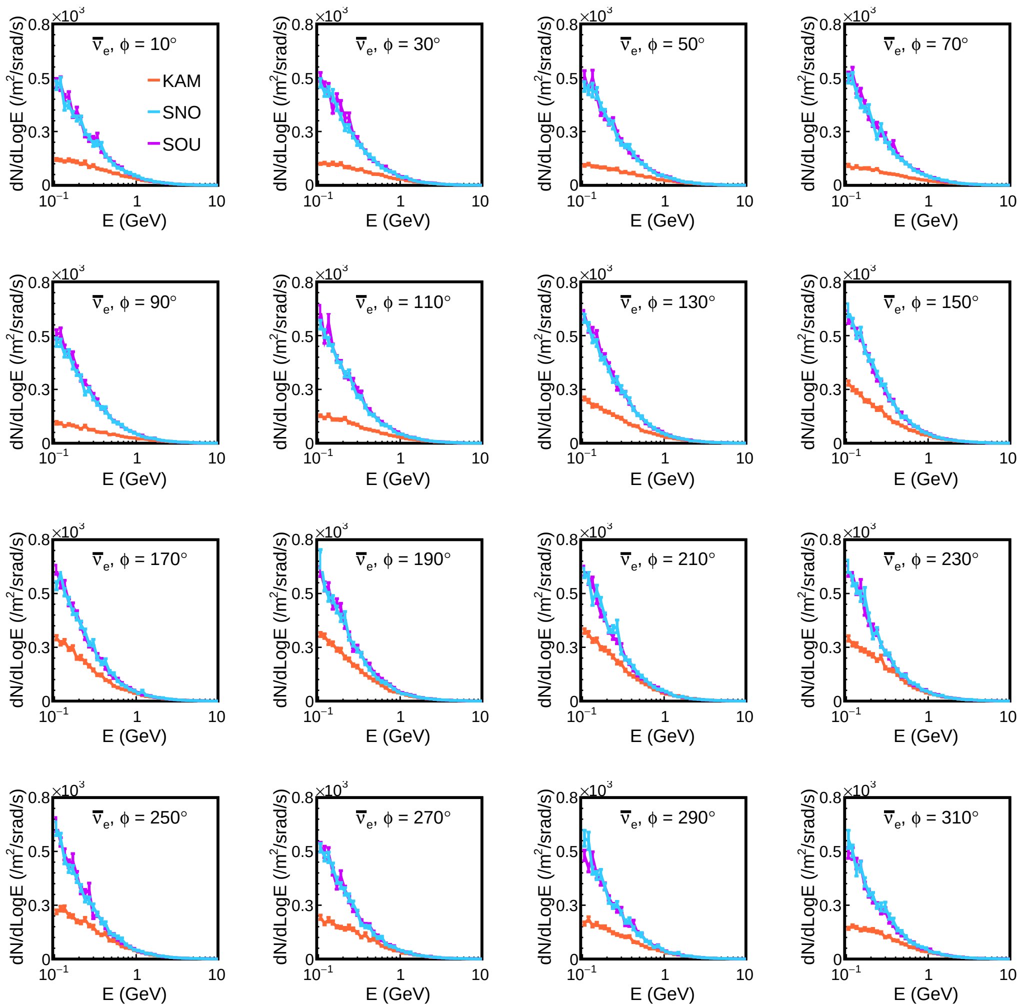

Figure C.11: Electron antineutrino flux during the minimum of solar activity cycle as a function of the azimuth angle.

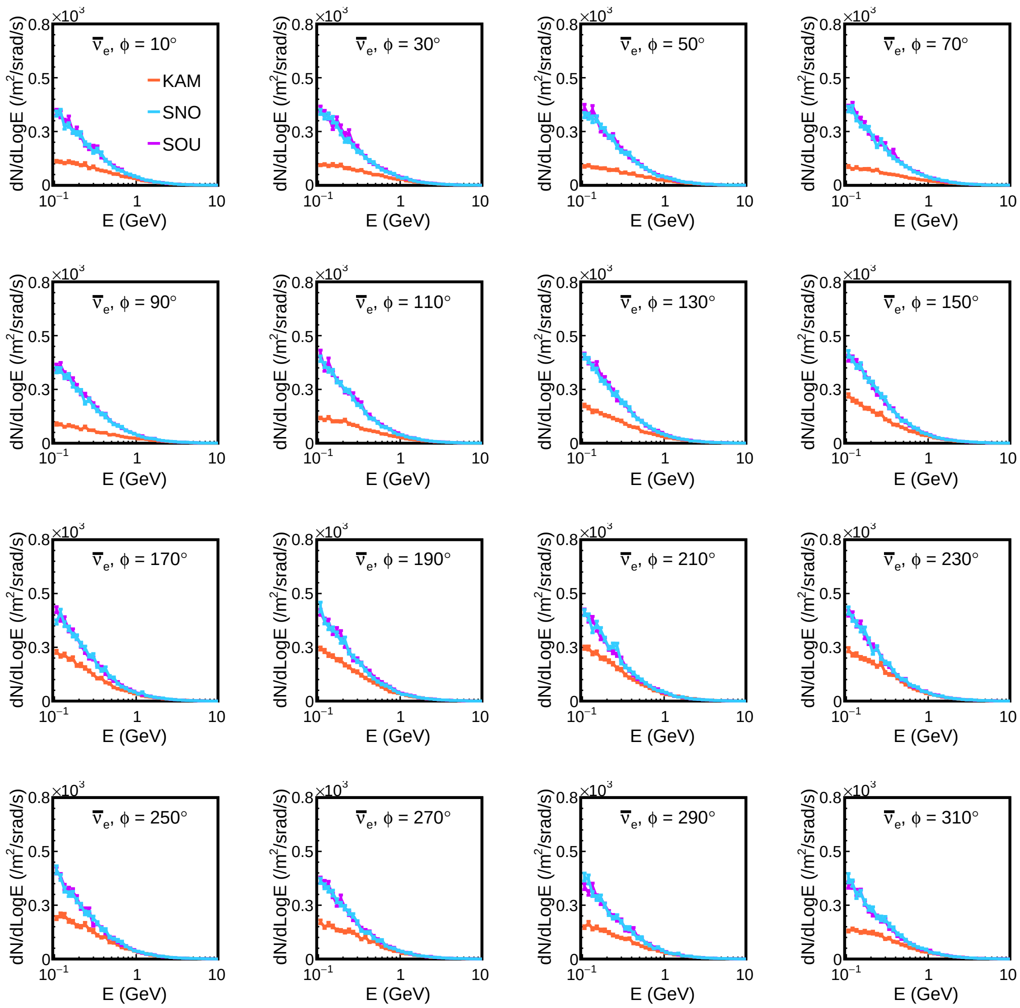

Figure C.12: Electron antineutrino flux during the maximum of solar activity cycle as a function of the azimuth angle.

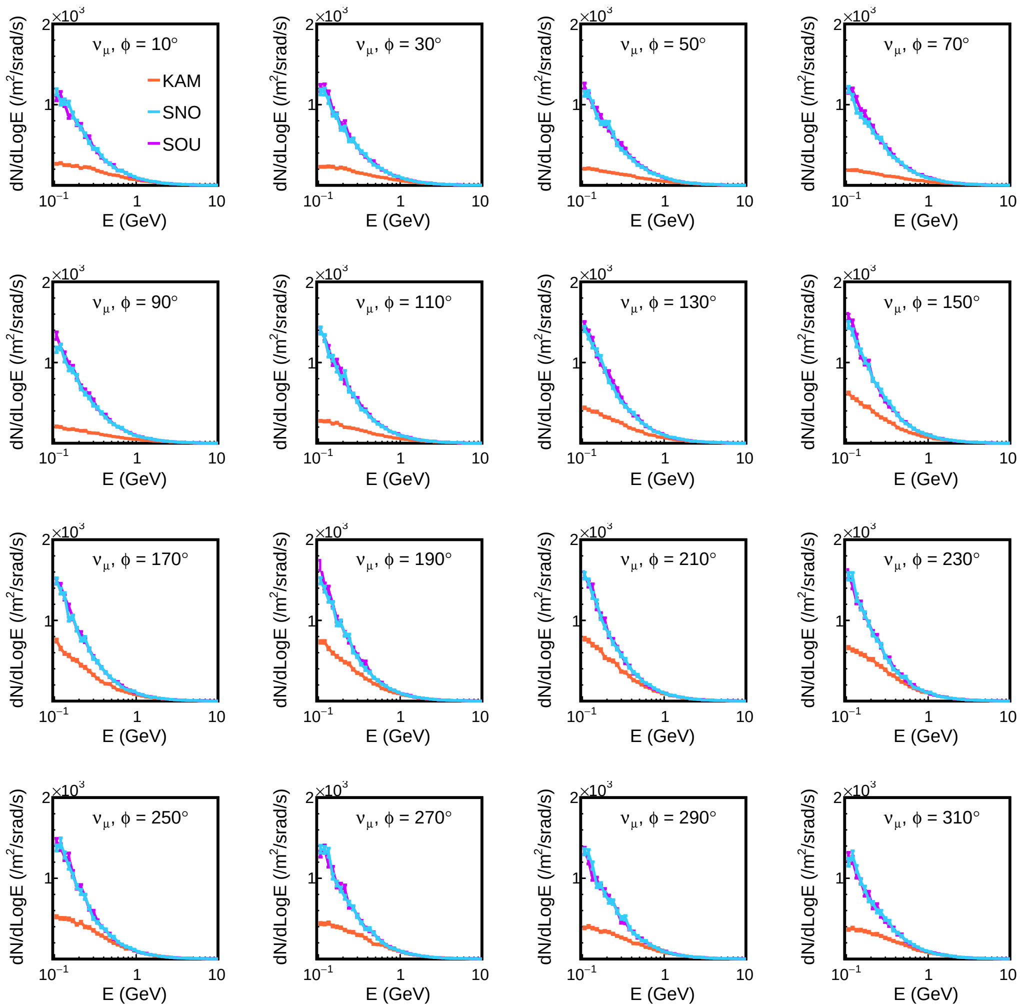

Figure C.13: Muon neutrino flux during the minimum of solar activity cycle as a function of the azimuth angle.

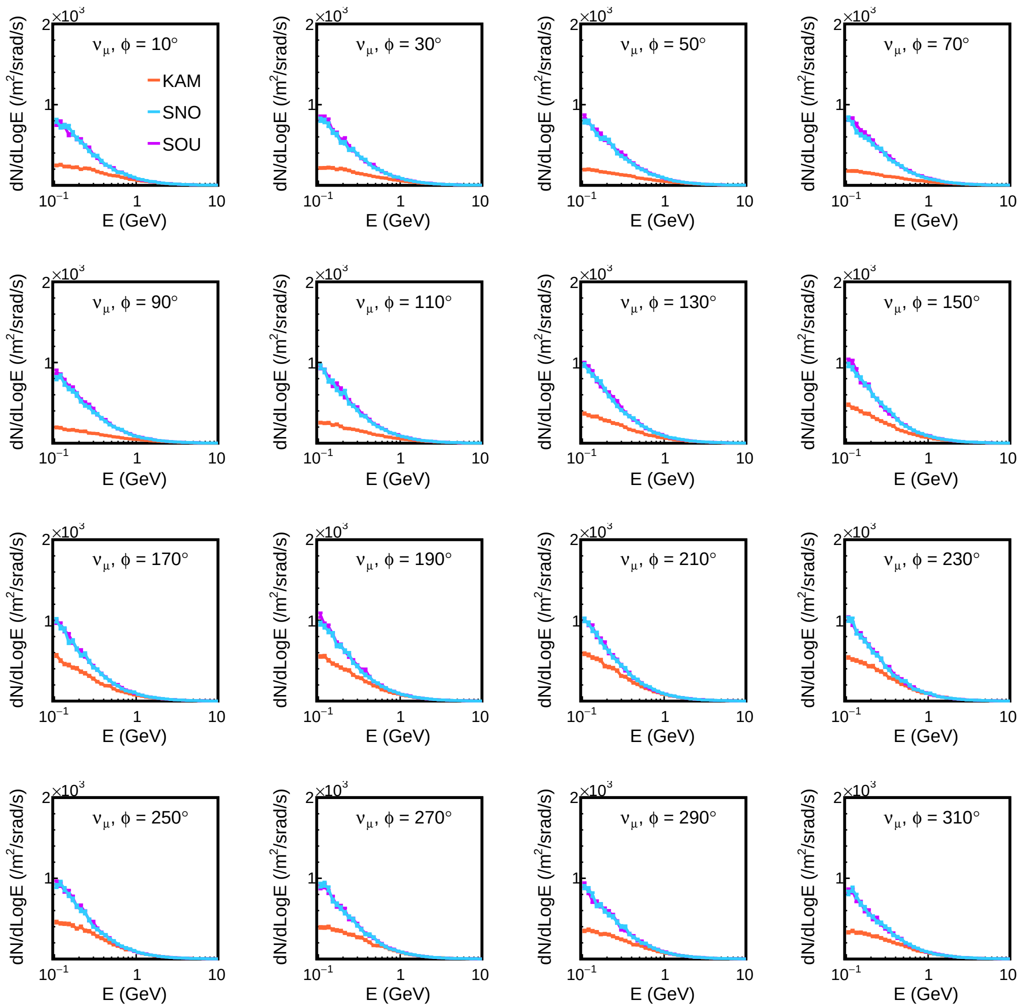

Figure C.14: Muon neutrino flux during the maximum of solar activity cycle as a function of the azimuth angle.

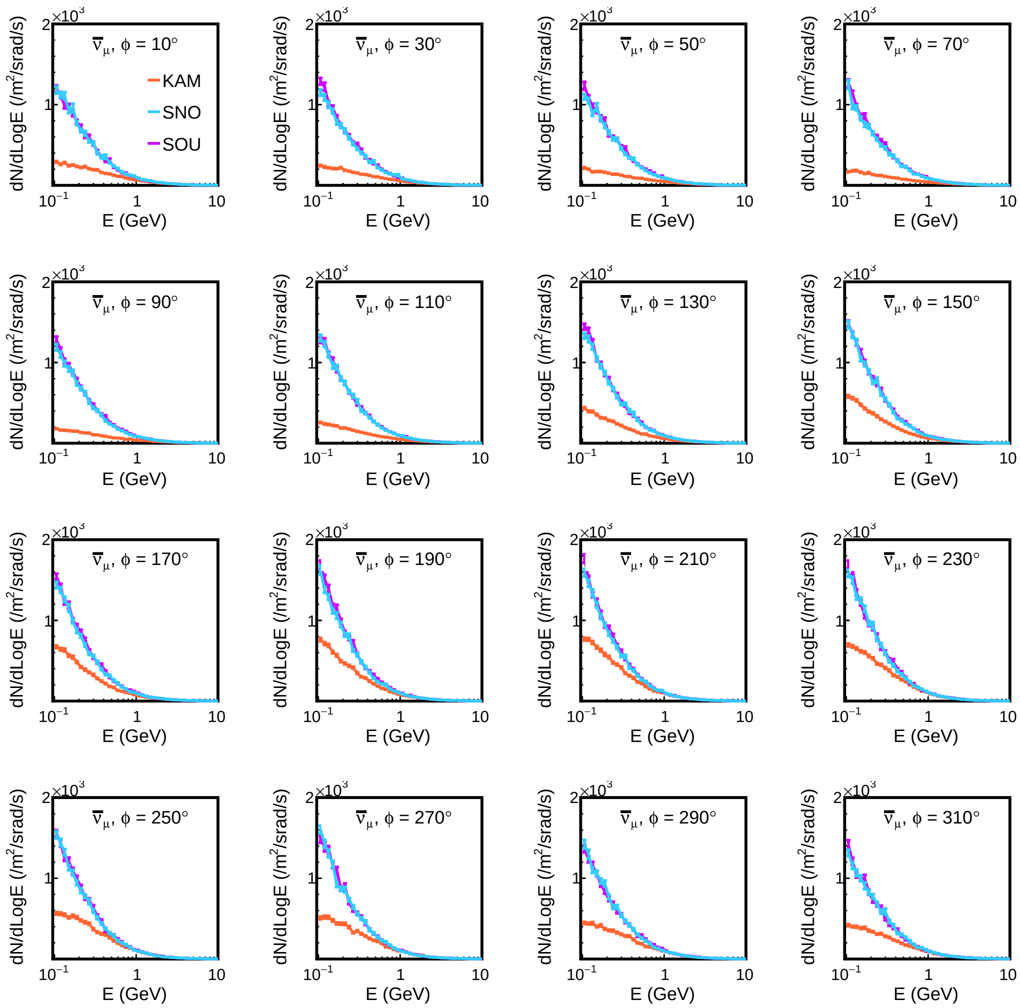

Figure C.15: Muon antineutrino flux during the minimum of solar activity cycle as a function of the azimuth angle.

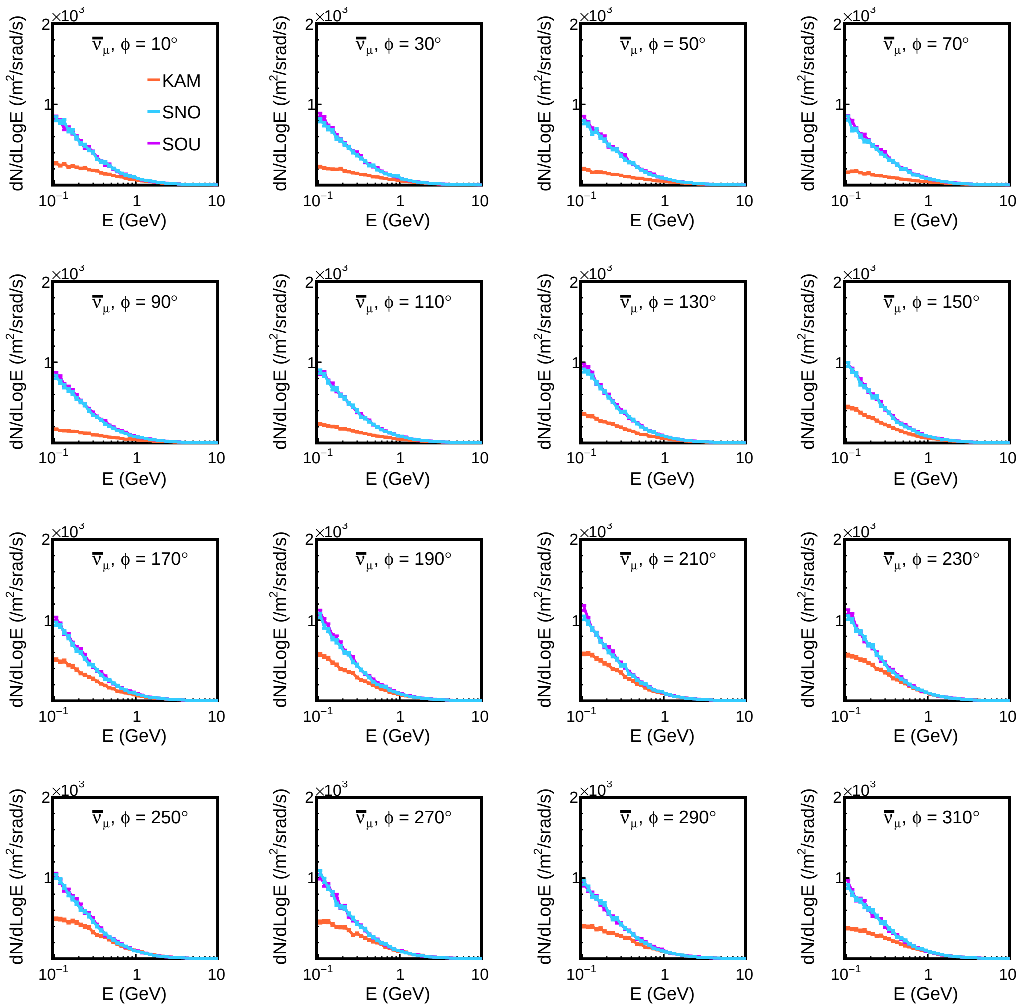

Figure C.16: Muon antineutrino flux during the maximum of solar activity cycle as a function of the azimuth angle.

Appendix D

Multivariate Method in Event Selection

We will start with a very brief introduction of the likelihood ratio method. Consider an event indexed i with a set of D features $x_k^{(i)}$. The multi-dimensional signal(background) PDF for each event is called $p_{\mathrm{s(b)}}$. If we can assume no correlation between x_k, this multi-dimensional PDF is just the product of the 1D PDF $p_{\mathrm{s(b),k}}\left(x_k^{(i)}\right)$. The likelihood of the event to be signal (background) then can be written as

$$L_{\mathrm{s(b)}}^{(i)} = \prod_{k=1}^{D} p_{\mathrm{s(b),k}}\left(x_k^{(i)}\right). \tag{D.1}$$

Once $L_{\mathrm{s}}^{(i)}$ and $L_{\mathrm{b}}^{(i)}$ are found, one can form the following classifier

$$y^{(i)} = \frac{L_{\mathrm{s}}^{(i)}}{L_{\mathrm{s}}^{(i)} + L_{\mathrm{b}}^{(i)}}. \tag{D.2}$$

A cut on $y^{(i)}$ like $[\alpha, 1]$ can be applied to select the signal events.

To be able to build the likelihood function as in (D.1) from training unbinned data we have to first standardize the features and then calculate the 1D probability density.

The standization of the features are conducted as following. For each feature x_k, we can find mean μ_k and standard deviation σ_k from all the events.

Then for each event, we set

$$X_k^{(i)} = \frac{X_k^{(i)} - \mu_k}{\sigma_k}. \tag{D.3}$$

Notice that the μ_k and σ_k are calculated with samples of both signals and backgrounds.

To build the 1D PDF $p_{\mathrm{s(b),k}}\left(x_k^{(i)}\right)$ for the k^{th} feature, we scan through all the value x_k. At each x_k, we define 5 neighboring regions. For each region, we count the number of background (signal) events, then divided this number by the total number of events and the measure[1] of the corresponding region to find the density of background (signal). The average of the 5 found density values will be used as an estimation for the PDF at x_k. A simple integral is calculated at the end of the process in order to normalize the found PDF.

In the following section, this method will be applied to the case of the neutron-antineutron oscillation search in NOvA. The dataset used in this section is the same as the dataset introduced in Section 7.2. It is split into 80% training and 20% testing samples. As this study is currently under development, we only utilize 4 among all 9 selection variables available. Unbinned version of the data is used for the multivariate event selection method presented here.

Four variables used here are (i) the event duration (in ns), (ii) the position-timing correlation factor, the average hit energy (in GeV) (iii) in XZ

[1]For the case of 1D considered here, a region is simply an interval and its measure is simply the width of this interval.

and (iv) YZ views. The distribution of those variables are shown in the Figure D.1.

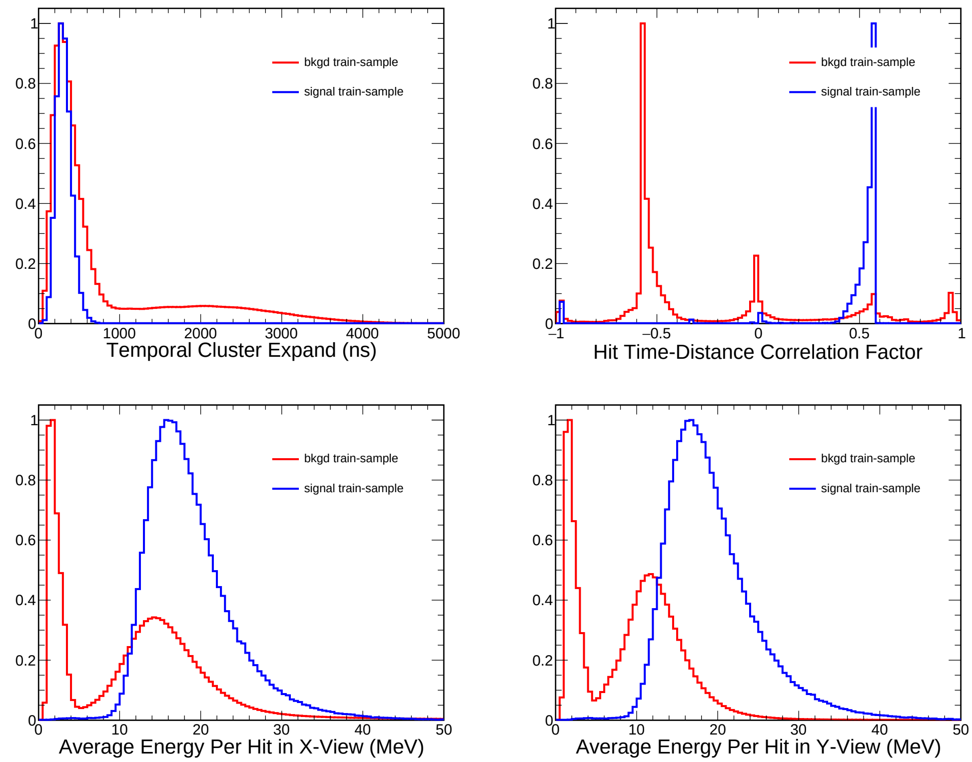

Figure D.1: Distributions of the event duration (top-left), the position-timing correlation factor (top-right), the average hit energy in XZ (bottom-left) and YZ (bottom-right) views. For the visualization purpose, the signal training sample (in blue, correspond to simulated signal events) and the background training sample (in red, corresponding to the unblinded FD's data) are normalized separately.

After standardizing the 4 selection variables and applying the density estimation algorithm described above, we obtained the 1D PDF corresponding to each variable for both signal and background training samples. Figure D.2

shows the normalized plot of these PDFs.

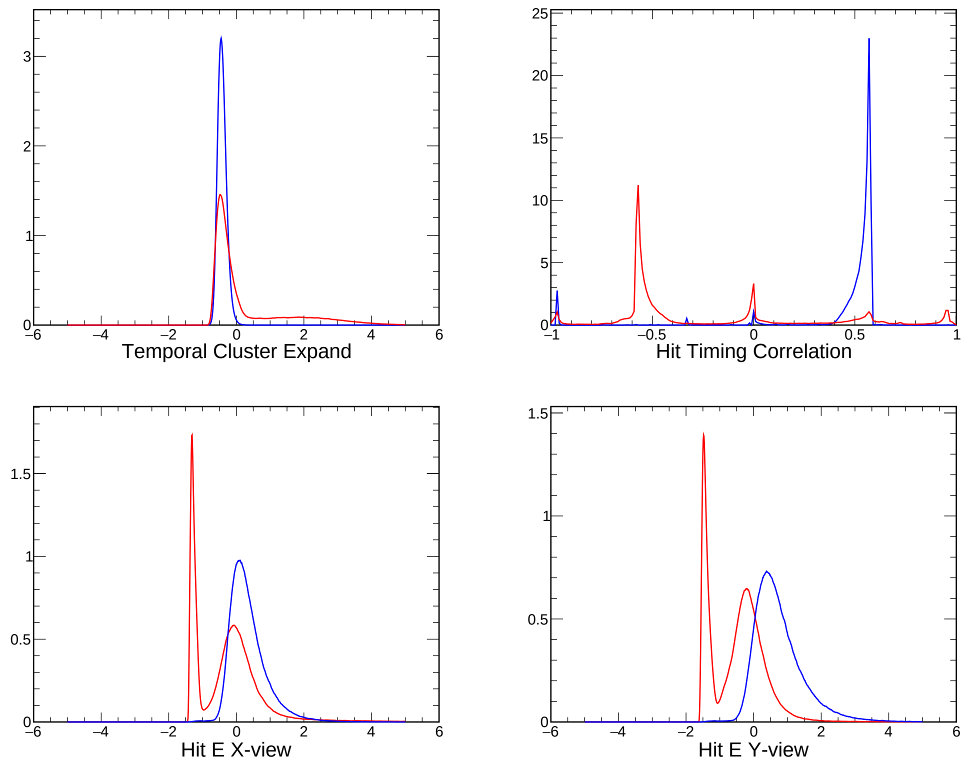

Figure D.2: PDFs of the event duration (top-left), the position-timing correlation factor (top-right), the average hit energy in XZ (bottom-left) and YZ (bottom-right) views. PDFs corresponding to the signal and background training samples are shown in blue and red, respectively. Each PDF has been normalized so that the areas under their curves are all 1.

Having the 1D PDF of all four selection variables ready, we can apply Equation (D.1) to calculate the likelihood ratio classifier. Figure D.3 shows the distribution of this classifier calculated for the training and testing samples.

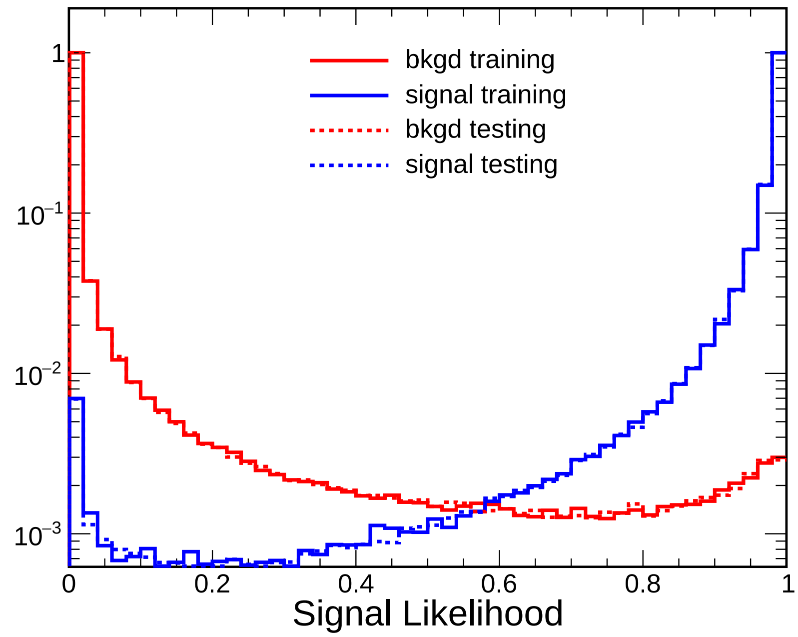

Figure D.3: The distributions of the likelihood ratio for training (solid) and testing (dashed) samples. Signal and background samples are shown in blue and red, respectively.

A cut on the value of the classifier closer to 1 is desired. An advantage of this multivariate approach is that it makes the optimization of the event selection easier. The efficiency and purity become functions of a single argument which is the cut value chosen.

This approach is currently a work under development. To complete this method, the correlations between the selection variables need to be taken into account. Also, the features corresponding to different sources of background might have different correlations. Thus, this method will benefit greatly once a background model is fully developed.

Bibliography

[1] D. Ayres et al. The NOvA Technical Design Report. 10 2007.

[2] K. Abe et al. Search for $n - \overline{n}$ oscillation in super-kamiokande. *Phys. Rev. D*, 91:072006, Apr 2015.

[3] F. Reines et al. Conservation of the number of nucleons. *Phys. Rev.*, 96:1157–1158, Nov 1954.

[4] *Fundamental Physics at the Intensity Frontier*, 2012.

[5] D. Phillips et al. Neutron-antineutron oscillations: Theoretical status and experimental prospects. *Physics Reports*, 612:1 – 45, 2016. Neutron-Antineutron Oscillations: Theoretical Status and Experimental Prospects.

[6] Y. Kamyshkov. Neutron-antineutron oscillations, 2002.

[7] E. S. Smith. Blessing Package: 90% CL “With Friends” for 3F Ana2020 - Neutrino2020 version. Technical Report NOVA-doc-46232-v3, June 2020.

[8] B. N. Nayak. Pedagogical Bi-Probability Plots. Technical Report NOvA-doc-38454-v1, June 2019.

[9] J. A. Vasel et al. Observing the next galactic supernova with the nova detectors, 2017.

[10] F. Psihas. Event Displays for Nue Selected Events. Technical Report NOVA-doc-15647-v4, June 2016.

[11] R. Kwarciany et al. Nova daq, system architecture, data combiner and timing system. In *2007 15th IEEE-NPSS Real-Time Conference*, pp. 1–5, 2007.

[12] N. Felt et al. NOvA Frontend Electronics User's Manual. Technical Report NOVA-doc-14514-v3, Dec 2015.

[13] J. Vasel. Blessing Package for New Perspectives - Timing System (DAQ). Technical Report NOVA-doc-15631-v1, Jun 2016.

[14] E. Niner. Timing Calibration Technical Note. Technical Report NOVA-doc-12570-v2, January 2015.

[15] J. Huang. Neutron-Antineutron Oscillation Search: Overlay with Cosmic Data, Data Driven Trigger. Technical Report UTKLDocDB-doc-1938-v3, University of Texas at Austin, January 2018.

[16] A. J. Norman and M. Tamsett. DDT blessed plots Neutrino 14. Technical Report NOVA-doc-11471-v1, June 2014.

[17] A. Norman. The NOvA data acquisition system. *Journal of Physics: Conference Series*, 396(1):012035, dec 2012.

[18] M. Tanaka et al. Search for proton decay into three charged leptons in 0.37 megaton-years exposure of the super-kamiokande. *Phys. Rev. D*, 101:052011, Mar 2020.

[19] K. Abe et al. Search for proton decay via $p \to e^+\pi^0$ and $p \to \mu^+\pi^0$ in 0.31 megaton$\cdot$years exposure of the super-kamiokande water cherenkov detector. *Phys. Rev. D*, 95:012004, Jan 2017.

[20] K. Abe et al. Search for proton decay via $p \to \nu K^+$ using 260 kiloton$\cdot$year data of super-kamiokande. *Phys. Rev. D*, 90:072005, Oct 2014.

[21] C. Regis et al. Search for proton decay via $p \to \mu^+ K^0$ in super-kamiokande i, ii, and iii. *Phys. Rev. D*, 86:012006, Jul 2012.

[22] H. Nishino et al. Search for proton decay via $p \to e^+\pi^0$ and $p \to \mu^+\pi^0$ in a large water cherenkov detector. *Phys. Rev. Lett.*, 102:141801, Apr 2009.

[23] Y. Hayato et al. Search for proton decay through $p \to \overline{\nu} k^+$ in a large water cherenkov detector. *Phys. Rev. Lett.*, 83:1529–1533, Aug 1999.

[24] T. K. Kuo and S. T. Love. Neutron oscillations and the existence of massive neutral leptons. *Phys. Rev. Lett.*, 45:93–96, Jul 1980.

[25] S. Weinberg. Varieties of baryon and lepton nonconservation. *Phys. Rev. D*, 22:1694–1700, Oct 1980.

[26] K. S. Babu et al. Baryon number violation, 2013.

[27] F. Oosterhof et al. Baryon-number violation by two units and the deuteron lifetime. *Phys. Rev. Lett.*, 122:172501, Apr 2019.

[28] G. Fidecaro et al. Experimental search for neutron-antineutron transitions with free neutrons. *Physics Letters B*, 156(1):122 – 128, 1985.

[29] G. Bressi et al. Final results of a search for free neutron-antineutron oscillations. *Il Nuovo Cimento A (1965-1970)*, 103(5):731–750, May 1990.

[30] M. Baldo-Ceolin et al. A new experimental limit on neutron-antineutron oscillations. *Z. Phys. C - Particles and Fields*, 63:409–416, 1994.

[31] E. Friedman and A. Gal. Realistic calculations of nuclear disappearance lifetimes induced by $n\overline{n}$ oscillations. *Phys. Rev. D*, 78:016002, Jul 2008.

[32] H. Weyl. Electron and Gravitation. 1. (In German). *Z. Phys.*, 56:330–352, 1929. [Surveys High Energ. Phys.5,261(1986); ,121(1929)].

[33] E. C. G. Stueckelberg. Interaction forces in electrodynamics and in the field theory of nuclear forces. *Helv. Phys. Acta*, 11:299–328, 1938.

[34] E. P. Wigner. Invariance in physical theory. *Proceedings of the American Philosophical Society*, 93(7):521–526, 1949.

[35] A. Pais. Lecture at the International Conference on Theoretical Physics. In *International Conference on Theoretical Physics, 1953*, volume 10, pp. 457, 1953.

[36] T. Nakano and K. Nishijima. Charge Independence for V-particles*. *Progress of Theoretical Physics*, 10(5):581–582, 11 1953.

[37] H. Bondi and T. Gold. The Steady-State Theory of the Expanding Universe. *Monthly Notices of the Royal Astronomical Society*, 108(3):252–270, 06 1948.

[38] F. Hoyle. A New Model for the Expanding Universe. *Monthly Notices of the Royal Astronomical Society*, 108(5):372–382, 10 1948.

[39] M. Goldhaber. Status of conserved quantum numbers. 1 1977.

[40] T. D. Lee and C. N. Yang. Conservation of heavy particles and generalized gauge transformations. *Phys. Rev.*, 98:1501–1501, Jun 1955.

[41] R. v. Eötvös et al. Beiträge zum gesetze der proportionalität von trägheit und gravität. *Annalen der Physik*, 373(9):11–66, 1922.

[42] E. G. Adelberger et al. Searches for new macroscopic forces. *Annual Review of Nuclear and Particle Science*, 41(1):269–320, 1991.

[43] J. G. Lee et al. New test of the gravitational $1/r^2$ law at separations down to 52 μm. *Phys. Rev. Lett.*, 124:101101, Mar 2020.

[44] W. A. Terrano et al. Short-range, spin-dependent interactions of electrons: A probe for exotic pseudo-goldstone bosons. *Phys. Rev. Lett.*, 115:201801, Nov 2015.

[45] B. R. Heckel et al. Experimental bounds on interactions mediated by ultralow-mass bosons. *Phys. Rev. Lett.*, 63:2705–2708, Dec 1989.

[46] C. W. Stubbs et al. Limits on composition-dependent interactions using a laboratory source: Is there a "fifth force" coupled to isospin? *Phys. Rev. Lett.*, 62:609–612, Feb 1989.

[47] E. G. Adelberger et al. New constraints on composition-dependent interactions weaker than gravity. *Phys. Rev. Lett.*, 59:849–852, Aug 1987.

[48] C. W. Stubbs et al. Search for an intermediate-range interaction. *Phys. Rev. Lett.*, 58:1070–1073, Mar 1987.

[49] C. L. Bennett et al. First-year wilkinson microwave anisotropy probe (WMAP) observations: Preliminary maps and basic results. *The Astrophysical Journal Supplement Series*, 148(1):1–27, sep 2003.

[50] A. D. Sakharov. Violation ofCPin variance,casymmetry, and baryon asymmetry of the universe. *Soviet Physics Uspekhi*, 34(5):392–393, may 1991.

[51] G. 't Hooft. Symmetry Breaking through Bell-Jackiw Anomalies. *Phys. Rev. Lett.*, 37:8–11, Jul 1976.

[52] G. 't Hooft. Computation of the quantum effects due to a four-dimensional pseudoparticle. *Phys. Rev. D*, 14:3432–3450, Dec 1976.

[53] V. Kuzmin et al. On anomalous electroweak baryon-number non-conservation in the early universe. *Physics Letters B*, 155(1):36 – 42, 1985.

[54] M. Shaposhnikov. Baryon asymmetry of the universe in standard electroweak theory. *Nuclear Physics B*, 287:757 – 775, 1987.

[55] L. Canetti et al. Matter and antimatter in the universe. *New Journal of Physics*, 14(9):095012, sep 2012.

[56] R. N. Mohapatra. Neutron–anti-neutron oscillation: theory and phenomenology. *Journal of Physics G: Nuclear and Particle Physics*, 36(10):104006, Sep. 2009.

[57] C. Theroine. A neutron-antineutron oscillation experiment at the european spallation source. *Nuclear and Particle Physics Proceedings*, 273-275:156 – 161, 2016. 37th International Conference on High Energy Physics (ICHEP).

[58] J. Chung et al. Search for neutron-antineutron oscillations using multiprong events in soudan 2. *Phys. Rev. D*, 66:032004, Aug 2002.

[59] C. Berger et al. Search for neutron-antineutron oscillations in the fréjus detector. *Physics Letters B*, 240(1):237 – 242, 1990.

[60] M. Takita et al. Search for neutron-antineutron oscillation in ^{16}O nuclei. *Phys. Rev. D*, 34:902–904, Aug 1986.

[61] B. Aharmim et al. Search for neutron-antineutron oscillations at the sudbury neutrino observatory. *Phys. Rev. D*, 96:092005, Nov 2017.

[62] B. T. Cleveland et al. Measurement of the solar electron neutrino flux with the homestake chlorine detector. *The Astrophysical Journal*, 496(1):505–526, mar 1998.

[63] Y. Fukuda et al. Solar neutrino data covering solar cycle 22. *Phys. Rev. Lett.*, 77:1683–1686, Aug 1996.

[64] S. Fukuda et al. Determination of solar neutrino oscillation parameters using 1496 days of super-kamiokande-i data. *Physics Letters B*, 539(3):179 – 187, 2002.

[65] Q. R. Ahmad et al. Measurement of the rate of $\nu_e + d \to p + p + e^-$ interactions produced by ^8b solar neutrinos at the sudbury neutrino observatory. *Phys. Rev. Lett.*, 87:071301, Jul 2001.

[66] Q. R. Ahmad et al. Direct evidence for neutrino flavor transformation from neutral-current interactions in the sudbury neutrino observatory. *Phys. Rev. Lett.*, 89:011301, Jun 2002.

[67] J. N. Abdurashitov et al. Measurement of the solar neutrino capture rate with gallium metal. iii. results for the 2002–2007 data-taking period. *Phys. Rev. C*, 80:015807, Jul 2009.

[68] P. Anselmann et al. Solar neutrinos observed by gallex at gran sasso. *Physics Letters B*, 285(4):376 – 389, 1992.

[69] W. Hampel et al. Gallex solar neutrino observations: results for gallex iv. *Physics Letters B*, 447(1):127 – 133, 1999.

[70] M. Altmann et al. Complete results for five years of gno solar neutrino observations. *Physics Letters B*, 616(3):174 – 190, 2005.

[71] Y. Abe et al. Indication of reactor $\overline{\nu}_e$ disappearance in the double chooz experiment. *Phys. Rev. Lett.*, 108:131801, Mar 2012.

[72] K. Eguchi et al. First results from kamland: Evidence for reactor antineutrino disappearance. *Phys. Rev. Lett.*, 90:021802, Jan 2003.

[73] T. Araki et al. Measurement of neutrino oscillation with kamland: Evidence of spectral distortion. *Phys. Rev. Lett.*, 94:081801, Mar 2005.

[74] F. P. An et al. Observation of electron-antineutrino disappearance at daya bay. *Phys. Rev. Lett.*, 108:171803, Apr 2012.

[75] F. P. An et al. Improved measurement of electron antineutrino disappearance at daya bay. *Chinese Physics C*, 37(1):011001, jan 2013.

[76] F. P. An et al. Spectral measurement of electron antineutrino oscillation amplitude and frequency at daya bay. *Phys. Rev. Lett.*, 112:061801, Feb 2014.

[77] J. K. Ahn et al. Observation of reactor electron antineutrinos disappearance in the reno experiment. *Phys. Rev. Lett.*, 108:191802, May 2012.

[78] D. Casper et al. Measurement of atmospheric neutrino composition with the imb-3 detector. *Phys. Rev. Lett.*, 66:2561–2564, May 1991.

[79] K. Hirata et al. Experimental study of the atmospheric neutrino flux. *Physics Letters B*, 205(2):416 – 420, 1988.

[80] K. Daum et al. Determination of the atmospheric neutrino spectra with the fréjus detector. *Zeitschrift für Physik C Particles and Fields*, 66(3):417–428, Sep 1995.

[81] Y. Fukuda et al. Evidence for oscillation of atmospheric neutrinos. *Phys. Rev. Lett.*, 81:1562–1567, Aug 1998.

[82] Y. Ashie et al. Evidence for an oscillatory signature in atmospheric neutrino oscillations. *Phys. Rev. Lett.*, 93:101801, Sep 2004.

[83] M. H. Ahn et al. Measurement of neutrino oscillation by the k2k experiment. *Phys. Rev. D*, 74:072003, Oct 2006.

[84] D. G. Michael et al. Observation of muon neutrino disappearance with the minos detectors in the numi neutrino beam. *Phys. Rev. Lett.*, 97:191801, Nov 2006.

[85] P. Adamson et al. Measurement of neutrino oscillations with the minos detectors in the numi beam. *Phys. Rev. Lett.*, 101:131802, Sep 2008.

[86] P. Adamson et al. Measurement of the neutrino mass splitting and flavor mixing by minos. *Phys. Rev. Lett.*, 106:181801, May 2011.

[87] K. Abe et al. First muon-neutrino disappearance study with an off-axis beam. *Phys. Rev. D*, 85:031103, Feb 2012.

[88] K. Abe et al. Measurement of neutrino oscillation parameters from muon neutrino disappearance with an off-axis beam. *Phys. Rev. Lett.*, 111:211803, Nov 2013.

[89] N. Agafonova et al. Final results of the opera experiment on ν_τ appearance in the cngs neutrino beam. *Phys. Rev. Lett.*, 120:211801, May 2018.

[90] K. Abe et al. Indication of electron neutrino appearance from an accelerator-produced off-axis muon neutrino beam. *Phys. Rev. Lett.*, 107:041801, Jul 2011.

[91] P. Adamson et al. Improved search for muon-neutrino to electron-neutrino oscillations in minos. *Phys. Rev. Lett.*, 107:181802, Oct 2011.

[92] K. Abe et al. Evidence of electron neutrino appearance in a muon neutrino beam. *Phys. Rev. D*, 88:032002, Aug 2013.

[93] K. Abe et al. Evidence for the appearance of atmospheric tau neutrinos in super-kamiokande. *Phys. Rev. Lett.*, 110:181802, May 2013.

[94] A. Pastore. Recent results of the OPERA neutrino experiment. *PoS*, EPS-HEP 2013:525, 2014.

[95] A. Y. Smirnov. Neutrino mass, mixing and discrete symmetries. *Journal of Physics: Conference Series*, 447:012004, jul 2013.

[96] M. A. Acero et al. First measurement of neutrino oscillation parameters using neutrinos and antineutrinos by nova. *Phys. Rev. Lett.*, 123:151803, Oct 2019.

[97] M. Acero et al. Adjusting Neutrino Interaction Models and Evaluating Uncertainties using NOvA Near Detector Data. 6 2020.

[98] M. Acero et al. Measurement of Neutrino-Induced Neutral-Current Coherent π^0 Production in the NOvA Near Detector. *Phys. Rev. D*, 102(1):012004, 2020.

[99] P. Adamson et al. Search for active-sterile neutrino mixing using neutral-current interactions in NOvA. *Phys. Rev. D*, 96(7):072006, 2017.

[100] M. Acero et al. Search for Multi-Messenger Signals in NOvA Coincident with LIGO/Virgo Detections. *Phys. Rev. D*, 101:112006, 2020.

[101] M. Acero et al. Supernova neutrino detection in NOvA. 5 2020.

[102] A. Norman. The NOvA Data Acquisition System. *J. Phys. Conf. Ser.*, 396:012035, 2012.

[103] D. F. Friend. CD3b Review - 16 Cell Extrusion Profiles. Technical Report NOVA-doc-3974-v3, July 2009.

[104] B. Pahlka. Photon transport simulations. Technical Report NOVA-doc-4277-v1, October 2009.

[105] J. B. Birks et al. The emission spectra of organic liquid scintillators. *British Journal of Applied Physics*, 14(3):141–143, mar 1963.

[106] L. Kuraray Co. Kuraray Fiber Catalog. Technical Report NOVA-doc-2665-v1, September 2007.

[107] A. J. Norman et al. NOvA DAQ Data Formats - Definitions. Technical Report NOVA-doc-4390-v16, December 2009.

[108] A. Norman et al. The NOvA timing system: A system for synchronizing a long baseline neutrino experiment. *Journal of Physics: Conference Series*, 396(1):012034, dec 2012.

[109] J. Allison et al. Recent developments in geant4. *Nuclear Instruments and Methods in Physics Research Section A: Accelerators, Spectrometers, Detectors and Associated Equipment*, 835:186 – 225, 2016.

[110] J. Allison et al. Geant4 developments and applications. *IEEE Transactions on Nuclear Science*, 53(1):270–278, Feb 2006.

[111] S. Agostinelli et al. Geant-4 - a simulation toolkit. *Nuclear Instruments and Methods in Physics Research Section A: Accelerators, Spectrometers, Detectors and Associated Equipment*, 506(3):250 – 303, 2003.

[112] T. Böhlen et al. The fluka code: Developments and challenges for high energy and medical applications. *Nuclear Data Sheets*, 120:211 – 214, 2014.

[113] A. Ferrari et al. Fluka: A multi-particle transport code. 12 2005.

[114] M. Campanella et al. First Calorimeter Simulation with the FLUGG Prototype. Technical Report ATL-SOFT-99-004, CERN, Dec 1999.

[115] C. Andreopoulos et al. The GENIE Neutrino Monte Carlo Generator. *Nucl. Instrum. Meth.*, A614:87–104, 2010.

[116] J. E. Hewes. Searches for bound neutron-antineutron oscillation in liquid argon time projection chambers. 1 2017.

[117] M. Tanabashi et al. Review of Particle Physics. *Phys. Rev. D*, 98(3):030001, 2018.

[118] R. D. Woods and D. S. Saxon. Diffuse surface optical model for nucleon-nuclei scattering. *Phys. Rev.*, 95:577–578, Jul 1954.

[119] A. Bodek and J. L. Ritchie. Fermi-motion effects in deep-inelastic lepton scattering from nuclear targets. *Phys. Rev. D*, 23:1070–1091, Mar 1981.

[120] R. Brun and V. Filippini. The ROOT Documentation - TGenPhaseSpace. https://root.cern.ch/doc/master/classTGenPhaseSpace.html. Technical report, CERN.

[121] R. Merenyi et al. Determination of pion intranuclear rescattering rates in $\nu_\mu - \mathrm{Ne}$ versus $\nu_\mu - \mathrm{D}$ interactions for the atmospheric ν flux. *Phys. Rev. D*, 45:743–751, Feb 1992.

[122] M. Tanabashi et al. Review of particle physics. *Phys. Rev. D*, 98:030001, Aug 2018.

[123] S. Rafi et al. Nucleon density distribution in ^{9}C. *Phys. Rev. C*, 89:067601, Jun 2014.

[124] C. Hagmann et al. Cosmic-ray shower generator (cry) for monte carlo transport codes. In *2007 IEEE Nuclear Science Symposium Conference Record*, volume 2, pp. 1143–1146, Oct 2007.

[125] A. Aurisano. Tech Note: 2017 Light Model. Technical Report NOVA-doc-23228-v2, September 2017.

[126] A. Aurisano et al. The NOvA simulation chain. *Journal of Physics: Conference Series*, 664(7):072002, dec 2015.

[127] J. Huang. NNbar Oscillation: How to Set Limits, MC Simulation Using GENIE. Technical Report UTKLDocDB-doc-1924-v, University of Texas at Austin, January 2018.

[128] S. M. Kasahara. NOvA Data Acquisition System. *Physics Procedia*, 37:1876 – 1883, 2012. Proceedings of the 2nd International Conference on Technology and Instrumentation in Particle Physics (TIPP 2011).

[129] G. D. Barr et al. Three-dimensional calculation of atmospheric neutrinos. *Phys. Rev. D*, 70:023006, Jul 2004.

[130] M. Honda et al. Atmospheric neutrino flux calculation using the nrlmsise-00 atmospheric model. *Phys. Rev. D*, 92:023004, Jul 2015.

[131] D. Heck et al. *CORSIKA: a Monte Carlo code to simulate extensive air showers.* 1998.

[132] S. Roesler et al. The monte carlo event generator dpmjet-iii. In A. Kling et al., editors, *Advanced Monte Carlo for Radiation Physics, Particle Transport Simulation and Applications*, pp. 1033–1038, Berlin, Heidelberg, 2001. Springer Berlin Heidelberg.

[133] F. H. Report PITHA-85/02. Technical Report PITHA-85/02, RWTH Aachen, 1985.

[134] W. R. Nelson et al. Report SLAC 265. Technical Report SLAC 265, StanfordLinear Accelerator Center, 1985.

[135] M. D. Baird. Slicing module comparison techical note. Technical Report NOVA-doc-9195-v1, May 2013.

[136] M. Ester et al. A density-based algorithm for discovering clusters in large spatial databases with noise. pp. 226–231. AAAI Press, 1996.

[137] R. Brun and V. Filippini. The ROOT Documentation - TGraph. https://root.cern.ch/doc/master/classTGraph.html. Technical report, CERN.

[138] W. Verkerke and D. P. Kirkby. The RooFit toolkit for data modeling. *eConf*, C0303241:MOLT007, 2003.

[139] M. Strait. Tech Note - 2016 geometry and composition changes. Technical Report NOVA-doc-23132-v4, September 2017.

[140] S. G. Johnson. Adaptive Multidimensional Integration. https://github.com/stevengj/cubature. Technical report, Massachusetts Institute of Technology.

[141] C. Dover et al. NEUTRON ANTI-NEUTRON OSCILLATIONS IN NUCLEI. *Phys. Rev. D*, 27:1090–1100, 1983.

[142] M. Bergevin. *Search for Neutron Anti-neutron Oscillation at the Sudbury Neutrino Observatory*. PhD thesis, Guelph U., 2010.

Vita

Dung Phan [redacted]. He graduated from Vietnam National University, Hanoi and received a Bachelor of Science in Physics in 2012. He was accepted and started the Ph.D. program in the University of Texas at Austin in August, 2014.

Permanent address: 5701 S Mopac Expressway, Austin, Texas - 78749

This dissertation was typeset with LaTeX† by the author.

†LaTeX is a document preparation system developed by Leslie Lamport as a special version of Donald Knuth's TeX Program.